

**human myocardial perfusion *in vivo*  
using dynamic  
magnetic resonance imaging.**

Asvina Jivan

University of Leicester

Submitted for the degree of Doctor of Philosophy

Faculty of Medicine, Department of Radiology

University of Leicester

December 1998

UMI Number: U106312

All rights reserved

INFORMATION TO ALL USERS

The quality of this reproduction is dependent upon the quality of the copy submitted.

In the unlikely event that the author did not send a complete manuscript and there are missing pages, these will be noted. Also, if material had to be removed, a note will indicate the deletion.



UMI U106312

Published by ProQuest LLC 2013. Copyright in the Dissertation held by the Author.  
Microform Edition © ProQuest LLC.

All rights reserved. This work is protected against  
unauthorized copying under Title 17, United States Code.



ProQuest LLC  
789 East Eisenhower Parkway  
P.O. Box 1346  
Ann Arbor, MI 48106-1346

# **The quantitative assessment of human myocardial perfusion *in vivo* using dynamic magnetic resonance imaging.**

Asvina Jivan

## **Abstract**

A quantitative measure of myocardial perfusion is of use clinically to provide information about the severity and location of a perfusion abnormality. This can help in guiding the clinician in the choice of therapeutic intervention, and in monitoring changes in the perfusion abnormality following intervention.

The current methods of measuring perfusion have been examined and this thesis has assessed whether MRI could become a useful tool. MRI is non-invasive, and fast imaging sequences have opened the possibility of dynamic imaging. This, coupled with high spatial resolution allows assessment of the transmural layers of the myocardium.

In MR imaging, a measure of absolute myocardial perfusion (ml/min/g) is not possible at present because the MR signal is not directly related to the tissue concentration of the contrast agent. The concentration of the bolus needs to be accurately tracked through the tissue, in order for tracer kinetic models, which enable perfusion to be calculated, to be of use.

This thesis has tried to cover the difficulties of using MRI for quantitatively assessing myocardial perfusion and has tried to correct the errors which are introduced by the simplistic use of MRI. In this way, the imaging methodology has been optimised.

The optimised imaging techniques have been applied to patients with acute myocardial infarction. These patients were dynamically imaged using a new contrast agent Gd-BOPTA. The concentration of the agent was estimated, and a tracer kinetic model applied. The values estimated for perfusion were higher than expected, and brought into question the behaviour of the contrast agent.

The final experimental section has investigated whether Gd-BOPTA may behave differently to currently available contrast agents (e.g. Gd-DTPA), and so be responsible for the spurious perfusion results. Data are shown which support this argument, and further work is required in applying this optimised imaging technique of perfusion measurement using Gd-DTPA.

## **Acknowledgements**

I would like to thank Professor Cherryman for establishing this project, and for his help and guidance. I would especially like to thank Dr Mark Horsfield for the long discussions, and to members of the University Department of Radiology for their help and support. Many thanks to Julia and Derek and to the staff of the MRI unit.

Thankyou to my family and friends for being there, and a special thanks to Richard for coping with me.

# Contents

	Page
Abstract	2
Acknowledgements	3
List of Figures	11
List of Tables	13
<b>Chapter 1: Introduction</b>	
<b>1.1 Perfusion</b>	15
<b>1.2 Current methods of quantitatively assessing human myocardial perfusion</b>	15
1.2.1 Direct measurements of blood flow	16
1.2.1.I Electromagnetic flow meter	16
1.2.1.II Ultrasonic flow meters	17
1.2.2 Indicator and indicator dilution techniques	18
1.2.2.I Thermodilution	18
1.2.2.II Inert gas clearance techniques	18
1.2.2.III Positron Emission Tomography (PET)	20
1.2.2.IV <sup>201</sup> Thallium SPECT	21
1.2.2.V Contrast echocardiography	23
1.2.2.VI Ultrafast x-ray computed tomography	23
<b>1.3 The history of MRI</b>	23
<b>1.4 Cardiac MRI</b>	27
1.4.1 The cardiac cycle	28
1.4.2 Cardiac gating	29
1.4.3 The magnetohydrodynamic effect	30
<b>1.5 Aims of the thesis</b>	30

<b>1.6</b>	<b>References</b>	<b>31</b>
------------	-------------------	-----------

## **Chapter 2: Theory**

<b>2.1</b>	<b>The basic principles of magnetic resonance</b>	<b>43</b>
2.1.1	Magnetic properties of the nucleus	44
2.1.2	Hydrogen magnetic resonance	44
2.1.3	Radio frequencies in the MR signal	46
2.1.3.I	Quantum mechanical view	46
2.1.3.II	Classical view	46
<b>2.2</b>	<b>Image contrast</b>	<b>49</b>
2.2.1	$T_1$ , $T_2$ , and Proton density	49
2.2.2	Proton density	49
2.2.3	$T_1$ relaxation	50
2.2.4	$T_2$ relaxation	52
2.2.5	Molecular mechanisms of relaxation	53
2.2.6	Protein binding and relaxation	54
2.2.7	Factors affecting $T_2$ relaxation	54
<b>2.3</b>	<b>Other sources of image contrast</b>	<b>55</b>
2.3.1	Magnetic susceptibility	55
2.5.1.I	Paramagnetism	56
2.5.1.II	Superparamagnetism	57
2.5.1.III	Ferromagnetism	57
2.3.2	Contrast agents	57
2.5.2.I	Principles of relaxation enhancement	58
2.5.2.II	Tissue relaxivity	59
2.3.3	Flow	60
2.3.4	Blood and haemorrhage	60
2.3.5	Chemical shift	61
2.3.6	Magnetisation transfer contrast	61

<b>2.4</b>	<b>Basic magnetic resonance pulse sequences</b>	<b>62</b>
2.4.1	Spin echo imaging	62
2.4.2	Gradient echo imaging	63
2.4.3	Inversion recovery imaging	64
<b>2.5</b>	<b>Magnetic resonance image formation</b>	<b>65</b>
2.5.1	Slice selection	66
2.5.2	Frequency encoding	66
2.5.3	Fourier transform	67
2.5.4	Phase encoding	67
2.5.5	Scan times	68
<b>2.6</b>	<b>References</b>	<b>69</b>

## **Chapter 3: Dynamic $T_1$ measurement using snapshot FLASH.**

<b>3.1</b>	<b>Introduction</b>	<b>70</b>
3.1.1	General factors affecting accuracy and precision of $T_1$ relaxation measurements	70
3.1.2	Methods of $T_1$ measurement using MRI	72
3.1.2.1	Multishot techniques	72
3.1.2.1.I	Progressive saturation & saturation recovery	72
3.1.2.1.II	Inversion recovery	73
3.1.2.1.III	Two point measures	74
3.1.2.1.IV	Hybrid schemes	75
3.1.2.1.V	Variable flip angles	75
3.1.2.2	Single shot techniques	76
3.1.2.2.I	Stimulated echo	76
3.1.2.2.II	Multiple excitation pulses	78
3.1.2.3	Dynamic imaging	80

<b>3.2</b>	<b>Aims</b>	80
3.2.1	Signal loss due to reduction in overall sequence repetition time	80
3.2.2	Effect of read pulse flip angle on overall signal intensity	80
3.2.3	Correction for specified inaccuracies	80
3.2.4	Ability to predict $TI_{null}$ for dynamic snapshot FLASH	81
<b>3.3</b>	<b>Theory</b>	81
3.3.1	The snapshot FLASH sequence.	81
3.3.2	The theoretical effects of the overall sequence repetition time	82
3.3.3	The theoretical effects of the read pulse flip angle	84
<b>3.4</b>	<b>Method</b>	86
3.4.1	Assessment of effects on $T_1$ measurement of phantoms	86
3.4.1.1	Effect of flip angle and 2 vs. 3 parameter fit on $T_1$ measurement using saturation recovery gradient echo imaging.	86
3.4.1.2	Signal loss due to $T_2$ relaxation.	87
3.4.2	$T_1$ measurement of phantoms	88
3.4.3	The effect of a reduction in the overall sequence repetition rate and ability to predict null point.	88
3.4.4	The effect of altering the read pulse flip angle.	89
<b>3.5</b>	<b>Results</b>	89
3.5.1	Assessment of effects on $T_1$ measurement of phantoms.	89
3.5.1.1	Effect of flip angle and 2 vs. 3 parameter fit on $T_1$ measurement using saturation recovery gradient echo imaging.	89
3.5.1.2	Signal loss due to $T_2$ relaxation.	90
3.5.2	The effect of a reduction in the overall sequence repetition rate and ability to predict null point.	92
3.5.3	The effect of altering the read pulse flip angle.	94
<b>3.6</b>	<b>Discussion</b>	95
<b>3.7</b>	<b>Conclusion</b>	96



## Chapter 4: The dynamic measurement of myocardial $T_1$ relaxation *in vivo* using snapshot FLASH

<b>4.1</b>	<b>Introduction</b>	102
4.1.1	Reasons for measuring relaxation <i>in vivo</i>	102
4.1.2	Measurement of myocardial $T_1$ relaxation <i>in vivo</i>	103
4.1.3	Considerations for <i>in vivo</i> myocardial $T_1$ measurement	104
<b>4.2</b>	<b>Aims</b>	105
<b>4.3</b>	<b>Method</b>	106
4.3.1	The effect of the heart rate ( $TR_0$ ) on $T_1$ values in normal and abnormal myocardium.	107
4.3.1.1	Baseline (pre contrast) $T_1$ measurement	107
4.3.1.2	$T_1$ measurement during contrast injection	109
4.3.2	The effect of inversion time on the accuracy and precision of snapshot FLASH in measuring $T_1$ <i>in vivo</i> .	109
4.3.2.1	Phantom studies	109
4.3.2.2	Volunteer studies	110
4.3.2.2 I	Multiple TI (MTI) images	110
4.3.2.2 II	Dynamic images	110
4.3.3	The effect of ECG gating MRI scans on the myocardial $T_1$ values obtained	112
<b>4.4</b>	<b>Results</b>	112
4.4.1	The effect of the heart rate ( $TR_0$ ) on $T_1$ values in both normal and abnormal myocardial regions of interest.	112
4.4.1.1	Baseline (pre contrast)	114
4.4.1.2	During contrast injection	115
4.4.2	The effect of inversion time on the accuracy and precision of snapshot FLASH in measuring $T_1$ <i>in vivo</i> .	115

4.4.2.1 Phantom studies	115
4.4.2.2 Volunteer studies	117
4.4.3 The effect of ECG gating MRI scans on the myocardial $T_1$ values	120
4.4.4 Myocardial $T_1$ values from normal volunteers	121
<b>4.5 Discussion</b>	<b>123</b>
<b>4.6 Conclusion</b>	<b>124</b>
<b>4.7 References</b>	<b>126</b>

**Chapter 5: Clinical application of the unidirectional influx constant ( $K_i$ ) as a method of quantitatively assessing myocardial perfusion *in vivo*.**

<b>5.1 Introduction</b>	<b>130</b>
<b>5.2 Aims</b>	<b>133</b>
<b>5.3 Method</b>	<b>133</b>
5.3.1 MR imaging	133
5.3.2 Single photon emission computed tomography (SPECT)	135
<b>5.4 Results</b>	<b>137</b>
<b>5.5 Discussion</b>	<b>143</b>
<b>5.6 Conclusion</b>	<b>145</b>
<b>5.7 References</b>	<b>146</b>

## **Chapter 6: MR enhancement of human myocardium *in vivo* post acute myocardial infarction using Gd-BOPTA.**

<b>6.1</b>	<b>Introduction</b>	<b>152</b>
<b>6.2</b>	<b>Aims</b>	<b>154</b>
<b>6.3</b>	<b>Method</b>	<b>154</b>
<b>6.4</b>	<b>Results</b>	<b>155</b>
<b>6.5</b>	<b>Discussion</b>	<b>158</b>
<b>6.6</b>	<b>Conclusion</b>	<b>159</b>
<b>6.7</b>	<b>References</b>	<b>160</b>

## **Chapter 7: Thesis conclusions**

<b>7.1</b>	<b>References</b>	<b>165</b>
------------	-------------------	------------

<b>Appendix 1</b>	<b>Theoretical solutions for signal correction, when using a snapshot FLASH imaging sequence</b>	<b>164</b>
-------------------	--	------------

<b>Appendix 2</b>	<b>Volunteer questionnaire</b>	<b>167</b>
-------------------	--------------------------------	------------

<b>Appendix 3</b>	<b>Publications</b>	<b>169</b>
-------------------	---------------------	------------

## List of Figures

- Figure 1.1 Shows the application of Faraday's law of induction to an electromagnetic flow probe.
- Figure 1.2 A schematic representation of the heart
- Figure 1.3 A schematic representation of an ECG trace.
- Figure 2.1 Shows the angular momentum of a hydrogen atom.
- Figure 2.2 The alignment of the protons with the magnetic field  $B_0$ .
- Figure 2.3 Axis conventions.
- Figure 2.4 Shows the effect of the RF pulse on the  $M$  vector.
- Figure 2.5 Precession of protons.
- Figure 2.6 Effect of proton density on the amplitude of the free induction decay (FID) signal.
- Figure 2.7 Effect of TR on image contrast
- Figure 2.8 Effect of echo time (TE) on the image contrast
- Figure 2.9 Illustrates the spin-echo pulse sequence
- Figure 2.10 Diagrammatically illustrates the gradient echo pulse sequence.
- Figure 2.11 Diagrammatically illustrates the inversion recovery pulse sequence.
- Figure 2.12 Shows how the resonant frequency is varied by the superimposition of a gradient field on the existing main magnetic field ( $B_0$ ).
- Figure 3.1. A spin echo pulse sequence for partial or progressive saturation.
- Figure 3.2. An inversion recovery spin echo pulse sequence
- Figure 3.3. A variable tip angle gradient echo sequence.
- Figure 3.4. The stimulated echo pulse sequence.
- Figure 3.5 A multiple readout gradient echo sequence.
- Figure 3.6. Schematic representation of the z-magnetization during the snapshot FLASH sequence in the steady-state.
- Figure 3.7 Signal intensity as a function of  $T_1$  for various overall repetition times.
- Figure 3.8. Simulated errors in  $R_1$  measurement caused by using the simple equation (Eq. [A1.9]) as the overall TR is reduced.

- Figure 3.9. The simulated effect of increasing flip angle on the image signal intensity ratio, for a range of  $T_1$  values.
- Figure 3.10. The simulated effect of flip angle increase on the signal intensity of an " $M_0$ " image for a range of  $T_1$  values.
- Figure 3.11. The simulated effect of flip angle increase on signal amplitude for a range of  $T_1$  values.
- Figure 3.12. Graph showing the effect of a two vs. three parameter nonlinear curve fitting to estimate  $T_1$  relaxation times using a saturation recovery gradient echo method.
- Figure 3.13. The effect of [Gd] on the transverse relaxation time ( $R_2$ ).
- Figure 3.14. Graph showing the signal loss as a percentage of the  $M_0$  value, due to  $T_2$  effects.
- Figure 3.15. Normalised signal intensity response for three values of  $TR_0$ , flip angle= $8^\circ$ .
- Figure 3.16. Mean estimation of  $R_1$  for three values of  $TR_0$  using the simplified analysis of Eq. [A1.9], and the full analysis of Eq. [A1.6].
- Figure 3.17. Mean estimation of  $R_1$  for flip angles,  $1^\circ$ ,  $8^\circ$  and  $15^\circ$
- 
- Figure 4.1. Three short axis images are obtained from the left ventricle.
- Figure 4.2. Schematic representation of an ECG gated snapshot FLASH imaging sequence.
- Figure 4.3. Graph showing the calculated  $R_1$  over time using the simplified analysis of Eq.[A1.9] and the full analysis of Eq.[A1.6] during the introduction of a contrast agent gadobenate dimeglumine (Gd-BOPTA) from a patient who had a fast heart rate (100 bpm).
- Figure. 4.4 Graph showing the calculated  $R_1$  over time using the simplified analysis of Eq.[A1.9] and the full analysis of Eq.[A1.6] during the introduction of a contrast agent gadobenate dimeglumine (Gd-BOPTA) from a patient who had a slow heart rate.
- Figure. 4.5 Shows the calculated mean  $R_1$  values in a phantom using ECG gated dynamic snapshot FLASH imaging with two inversion times.
- Figure. 4.6 Graph showing the calculated mean  $R_1$  values obtained in volunteers using ECG gated dynamic snapshot FLASH imaging with two inversion times

- Figure. 4.7 The graph compares the calculated  $R_1$  values obtained in a volunteer using ECG gated dynamic snapshot FLASH imaging with two inversion times, and ECG gated snapshot FLASH imaging with multiple inversion times
- Figure. 4.8 The graph shows the calculated  $R_1$  value obtained during dynamic snapshot FLASH imaging with  $TI=820ms$ , with and without ECG gating.
- Figure. 4.9 The graph shows the  $R_1$  values obtained in ten volunteers using ECG gated snapshot FLASH imaging with multiple inversion times and full longitudinal relaxation between inversion pulses (MTI imaging).
- Figure 5.1 Three reconstructed transverse tomograms through the left ventricle.
- Figure 5.2 Shows the raw signal intensity data (A) and the calculated  $R_1$  values (B) which are then used to calculate the  $K_i$  (C). This is shown for two patients, Patient 1, with good quality raw data, and Patient 2, with poor quality raw data.
- Figure 5.3 The mean  $K_i$  obtained from thirty regions of interest are shown for the thirty patients in the study.
- Figure 5.4. Shows the anatomical areas represented by the ROI's at each of the imaging levels.
- Figure 5.5 This figure shows the correlation coefficient obtained for  $K_i$  and  $^{201}thallium$  SPECT.
- Figure 6.1 Shows the mean difference in percentage enhancement between 15 & 30 minute images for normal and reduced  $^{201}thallium$  uptake in each patient.

## List of Tables

Table 3.1.	Standard deviation of the $R_1$ for each flip angle using the simple and full analysis.
Table 4.1.	Calculated relaxation rates ( $R_1$ ) when using the simplified analysis of Eq.[A1.9], compared to the fuller analysis of Eq.[A1.6]. Results are shown for human myocardium during the arterial injection of Gd-BOPTA.
Table 4.2.	Percentage difference in baseline relaxation rates for the simplistic analysis Eq.[A1.9], and fuller analysis Eq.[A1.6] compared to the multiple inversion time relaxation rate calculation. This is shown for patients with fast and slow heart rates.
Table 4.3.	Percentage difference between relaxation rates at first pass peak for the simplistic analysis Eq.[A1.9], and fuller analysis Eq.[A1.6]. This is shown for patients with fast and slow heart rates.
Table 4.4.	Shows the mean and the variability in the calculated longitudinal relaxation rates for three types of imaging.
Table 4.5.	Shows the mean calculated $R_1$ values in one volunteer using three types of imaging for each of the three myocardial levels,
Table 4.6.	Shows the mean and the variability in the calculated relaxation rates, with and without ECG gating when dynamic imaging when a long TI is used
Table 4.7.	Shows the $R_1$ values obtained in ten volunteers using the multiple TI imaging (MTI).
Table 5.1	The mean and SD values for $K_i$ in all thirty patients.
Table 5.2	The mean and SD values for $\lambda$ in ROIs divided into normal and reduced $^{201}\text{thallium}$ uptake.
Table 5.3	Shows the relationship between $K_i$ , $\lambda$ and the $^{201}\text{thallium}$ assessment of ROIs.
Table 5.4	The grouping of ROIs according to the anatomical areas of the myocardium they represent.
Table 6.1.	The mean percentage signal enhancement for myocardial ROIs at 15 and at 30 minutes post contrast.
Table 6.2	Shows the sets of data upon which the Student's $t$ -test was performed.

# **Chapter 1: Introduction**

## **1.1 Perfusion**

The word perfusion comes from the Latin *perfundo*, to pour over or diffuse through. Diffusion is described as a process whereby atoms and molecules intermingle due to their random thermal (Brownian) motion. Perfusion describes the nutritive supply of blood to the tissue and the removal of waste products and is measured in mls of blood/min/100g tissue.

The term perfusion has many connotations in different medical situations. Physiologists interpret perfusion as referring to blood circulation and blood/tissue exchange, whereas radiologists or pathologists will refer to it as the density of microvasculature in a tissue as visualised by catheter angiography.

Tissue perfusion is dependant upon the minute structure of the tissue, blood microcirculation, and blood/tissue exchange. Quantitative measures of perfusion can be applied clinically to:

- a) provide information on the location, size and severity of perfusion abnormalities.
- b) help clinicians determine the patient's prognosis and preoperative risk, so guiding the clinician to appropriate therapeutic interventions.
- c) accurately monitor the change in the severity of a vascular disease after therapeutic interventions such as thrombolysis, percutaneous transluminal angioplasty, or bypass surgery.

## **1.2 Current methods of quantitatively assessing human myocardial perfusion**

The development of measurement technologies has enabled physiologists to obtain an understanding of the coronary blood flow in animals. However, techniques developed for use in animals cannot be easily transferred to humans. For example, in animals, the use of radiolabelled microspheres has enabled multiple measurements of absolute myocardial perfusion in ml/min/100g of tissue.



This technique is based on the principle that small particles, microspheres, introduced into the circulation, will mix uniformly and distribute in proportion to blood flow. The microspheres are then completely entrapped into precapillary vasculature during first pass delivery. By using a reference arterial blood flow during microsphere injection, myocardial perfusion is determined as the ratio of blood flow to tissue mass. Because of the need for tissue samples in order to determine the concentration of the microspheres, and because the microspheres (which can be radioactive) are trapped in the microvasculature, this technique is inapplicable to human studies.

Due to this limitation, there is less information on the regulation and control of human myocardial perfusion. It is assumed therefore that the coronary circulation in large mammals i.e. dogs and pigs, are reasonably similar to man. This may possibly be the case for normal but may not be so in the presence of disease. However, until absolute perfusion can be accurately measured in humans, no-one knows.

## **1.2.1 Direct measurements of blood flow**

### **1.2.1.I Electromagnetic flow meter**

This method is often used in animal studies, although can be used clinically in humans for the measurement of flow (mls/min) in coronary artery bypass grafts at the time of open heart surgery. This technique is based on the principle of Faraday's Law of inductance, which states that a conductor moving in a magnetic field generates an electric current.

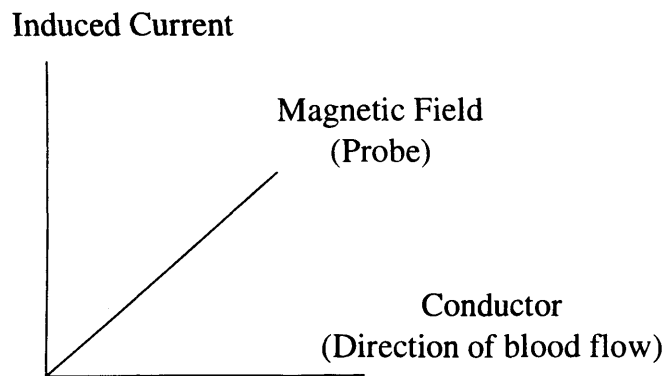


Figure 1.1 shows the direction of the blood flow, magnetic field and induced current, in the application of Faraday's law of induction to an electromagnetic flow probe.

This principle was first applied by Kolin (1936), and since then two types of probe have been developed:

- a) Perivascular probe, which measures the blood flow within bypass grafts during the time of surgery.
- b) Extra corporeal flow meters, which measures blood flow in cannulas.

This method has the advantage that it is able to measure rapid changes in blood flow. However it is limited in that accurate measurements require good probe vessel contact (Wyatt 1961). A blood vessel requires dissection to enable the probe to encircle it, which is unacceptable in humans for the measurement of blood flow in native coronary arteries. Electromagnetic flow probes when used intraoperatively to measure blood flow in bypass grafts, suffer from the problem of calibration. They work best when implanted, as applied in animal studies, where fibrous adhesions form around the probe, stabilising contact between the vessel and the probe. Finally there is the problem of assessing absolute myocardial perfusion, which is not possible as the perfusion bed of the vessel is undetermined.

#### **1.2.1.II Ultrasonic flow meters**

This method is based on the Doppler effect, first described by Johann Doppler (1842), which states that when sound waves are reflected from a moving structure, the frequency of the reflected wave is shifted in proportion to the velocity of the moving structure relative to the transmitter. Within the vascular tree, the Doppler shift is obtained from ultrasound waves being reflected off red blood cells.

In order to accurately measure the velocity of flow (m/s), the angle between the piezoelectric crystal (used to generate the ultrasound wave), and the blood vessel must also be known. For this to become volumetric flow (mls/s), the diameter of the blood vessel must be known. Ultrasound waves may be emitted and received by a single piezoelectric crystal, called Pulsed wave Doppler, or by separate piezoelectric crystals, called Continuous wave Doppler. Modern flow probes have two piezoelectric crystals, one on either side of the vessel, and an acoustic reflector placed mid way, on the opposite wall of the vessel. An ultrasound beam is transmitted across the vessel and reflected back to the other crystal.

Extravascular Doppler flowmeters have been applied clinically to measure the flow within (DeBono *et al* 1992), and patency of (Gould *et al* 1972), coronary artery bypass grafts. Transoesophageal Doppler echocardiography has been used to measure coronary sinus blood flow (Siostrzonek *et al* 1993), and blood flow in the proximal left coronary artery (Yamangishi *et al* 1991). This method has the advantage in that it is non invasive, and has high temporal resolution. However, it has technical limitations in that small variations in transmission angle produce large changes in Doppler shift. Also, it may not be possible to obtain an adequate signal in all patients using transthoracic and transoesophageal techniques.

An intravascular Doppler flowmeter comprises a catheter which has a pulsed piezoelectric crystal mounted at its tip, first developed by Hartley *et al* (1971). More recently a Doppler guide wire has been developed (Doucette *et al* 1992), enabling the measurement of blood velocity distal to a stenosis to be measured. Measurements of relative changes in coronary artery blood flow (Rossen *et al* 1992), are in good agreement with thermodilution measurements. The principle limitation of this technique is that the diameter of the vessel must be known in order to calculate blood flow. This may be obtained using angiography, or from ultrasound echoes, but small errors in diameter produce large errors in the calculated area. The technique is also dependant upon the blood velocity profile within a vessel, which may produce errors in the calculated mean flow velocity. Also, if a vessel changes diameter during the cardiac cycle, i.e. coronary sinus, absolute blood flow calculations are not possible. Finally, movement of the Doppler flow probe relative to the vessel wall may affect measurements.

## **1.2.2 Indicator and indicator dilution techniques**

### **1.2.2.1 Thermodilution**

This method was introduced by Ganz *et al* (1971), and is based on a simple principle. A miscible liquid, (saline) at a known lower temperature than blood, is infused into the coronary sinus. The change in temperature of the blood-fluid mixture down stream is proportional to blood flow.

The right side of the heart requires catheterisation in order to cannulate the coronary sinus, and the technique enables a broad range of blood flows to be measured. In order to obtain valid measurements, the injectate has to be infused at a constant rate, through an

insulated catheter to minimise heat exchange, and there should be complete mixing of the perfusate and Coronary sinus blood. Finally infusion should be for a short duration (20-30 seconds) to prevent recirculation, and sensitive thermistors are required to measure the change in temperature. The catheter should remain in a stable position within the Coronary sinus for multiple measurements of flow to be comparable.

This technique allows the measurement of blood flow from the anterior portion of the left ventricle, if the catheter is placed in the most proximal segment of the Coronary Sinus. This is a simple and relatively inexpensive method of measuring blood flow in humans. The disadvantage of this technique is that catheterisation of the Coronary sinus is required. In addition, rapid changes in blood flow cannot be monitored as a delay of 2-3 seconds exists between measurement and recording. Finally, measurement of blood flow is limited to areas drained by the Coronary Sinus, and in the presence of myocardial infarction the coronary venous drainage pattern is likely to be distorted.

#### **1.2.2.II Inert gas clearance techniques**

There are two types of tracer used for this method, a) radioactive tracers e.g. xenon<sup>133</sup>, and b) non radioactive tracers e.g. nitrous oxide, helium, hydrogen and argon.

This technique is based on the work of Kety and Schmidt (1945), who modified the indicator dilution principle. According to this, when an inert gas is introduced into the systemic circulation, there will be a faster rise in the arterial concentration of the gas than in the venous concentration, this is called saturation. When saturation has been reached, and the tracer input ceases, the tracer will diffuse back into the venous system, and this is called desaturation. In this case, the arterial concentration will fall more rapidly than venous concentration. In either saturation or desaturation, the coronary flow per unit weight is proportional to the integrated difference in tracer concentration between the arterial and venous concentrations.

This technique requires that arterial and venous blood is simultaneously sampled during saturation/desaturation to monitor the concentration of the tracer. The tracer must be physiologically inert, must not recirculate, and the blood-tissue partition coefficient (dimensionless) must be known. Finally, the blood flow must remain stable during the measurement period, usually 5-20 minutes.

Non-radioactive inert gases are detected by an initial separation using chromatography, and quantified by mass spectroscopy or an ionisation detector. Radioactive gases are detected by a multicrystal camera.

Accurate measurements require both stable conditions and a knowledge of the time course of interventions, allowing measurements of gas clearance times. These become less reliable when the myocardium is heterogeneous, such as during ischaemia or with fibrosis. Also this technique does not allow rapid changes in blood flow to be measured, and is unable to distinguish flow to selected transmural layers of the myocardium.

### **1.2.2.III Positron Emission Tomography (PET)**

This modality is dependant upon the detection of positrons, high energy positive electrons with a short half life, which are emitted from certain isotopes with an excess number of protons. If the excess proton decays, a positron, a neutron, and a neutrino are emitted. Positrons loose kinetic energy within a tissue due to collisions with other atoms, and rapidly come to rest. The positron then combines with an electron in an 'annihilation reaction' in which their mass is converted into energy and two photons of 511 keV are produced which travel at 180° to each other.

An array of paired detectors can be placed around the patient to detect the double photon emission, following an intravenous injection of a positron emitter. Data can then be acquired after an appropriate time interval, and the projection images can be reconstructed to created tomographic representations of the tracer concentration in the myocardium. Only coincident events are counted, which eliminates background emissions. Positron activity is measured in direct proportion to its tissue content, and is not a function of the distance from the counter so there is a higher counting efficiency (detected vs. emitted events).

The measurement of perfusion is based on the Kety Formula. The arterial input function of the indicator is established by withdrawing timed blood samples, and the tissue concentration is a function of the organ's extraction fraction, which shows the affinity of the indicator for the myocardium, and the myocardial blood flow. Several intravenously administered radiopharmaceuticals are being used to quantify myocardial perfusion and include,  $^{13}\text{NH}_3$ -ammonia,  $^{15}\text{O}$ -water  $\text{H}_2^{15}\text{O}$ ,  $^{82}\text{Rb}$ -rubidium and  $^{62}\text{Cu}$  copper.

The intravenous administration of  $^{13}\text{NH}_3$ -ammonia results in its rapid clearance from the blood into the myocardium, which retains it in proportion to flow (Schelbert *et al* 1979, 1981). Quantitative measurement of myocardial blood flow using  $^{13}\text{NH}_3$ -ammonia is

possible using a tracer kinetic model proposed by Musik *et al* (1993). This tracer is produced by a cyclotron, and has the disadvantage that many PET centres are established without cyclotrons.

Another cyclotron produced tracer is  $^{15}\text{O}$ -water ( $\text{H}_2^{15}\text{O}$ ) which has been used for myocardial perfusion measurements. This involves the intravenous administration of  $\text{H}_2^{15}\text{O}$ , and following a delay of 10-20 seconds to allow transit to the heart, data is collected. To correct for the blood pool background activity, after  $\text{H}_2^{15}\text{O}$  has decayed,  $\text{C}^{15}\text{O}$  is inhaled. This binds avidly to haemoglobin and enables the labelling of the vascular space, which is then subtracted from the  $\text{H}_2^{15}\text{O}$  image of the heart. Results in humans indicate that regions with the lowest relative perfusion corresponded anatomically with regions distal to coronary stenosis as defined by coronary angiography (Walsh *et al* 1988). However the limitations of the  $\text{H}_2^{15}\text{O}$  technique include low signal to noise ratios, after subtraction of the blood-pool. Also, this is a cyclotron tracer which has to be produced on site due to its short half-life (1.5 minutes).

$^{82}\text{Rb}$ -rubidium is a generator produced tracer, therefore having the advantage of eliminating the need for an on-site cyclotron. It also has a short half-life (1.5 minutes), so enabling serial evaluation of flow. However, this tracer is limited in that myocardial extraction is dependant upon blood flow (Mullani *et al* 1982).

$^{62}\text{Cu}$  copper pyruvaldehyde-bis( $\text{N}^4$ -methylthiosemicarbazonato) (PTSM), is a generator produced tracer. A biodistribution study by Green *et al* (1990) showed rapid blood clearance and prolonged tissue retention of the tracer. Sheldon *et al* (1990) found that there was an initial linear increase in copper radioactivity with blood flow, and then the increase was more gradual at flows greater than 2.5mls/min/g. Thus, to accurately estimate flow using this tracer, mathematical approaches are required to decouple flow and extraction.

In summary, PET imaging shows promise for the measurement of absolute myocardial perfusion. However, it is an expensive technique that uses ionising radiation, and as yet has limited spatial and temporal resolution.

#### **1.2.2.IV $^{201}\text{Tl}$ Thallium SPECT**

Cardiac single photon emission computed tomography (SPECT), enables the 3D assessment of myocardial perfusion. In conjunction with an intravenously injected diffusable indicator,  $^{201}\text{Tl}$ thallium, a rotating gamma camera detects emitted photons of a

defined energy. The data can then be used to produce reconstructed tomographic images through the heart.

<sup>201</sup>Thallium is a metallic element with biologic properties similar to potassium. The distribution of <sup>201</sup>thallium, following intravenous administration is primarily intracellular, (Gehring *et al* 1967, Lebowitz *et al* 1973, Mullins *et al* 1960). Transport of <sup>201</sup>thallium across the cell membrane is thought to occur via the sodium-potassium ATPase pump (Zimmer *et al* 1979). Initial distribution in the myocardium is related to regional blood flow (Nielsen *et al* 1980), with a high first pass extraction (Weich *et al* 1977). In general the uptake of <sup>201</sup>thallium in the heart is linearly related to myocardial blood flow, and so defects in the images are produced predominantly by regional deficits in myocardial blood flow distribution. There is a slight underestimation at high flows and overestimation at low flows (Nielsen *et al* 1980). <sup>201</sup>Thallium is washed out from the myocardium with a half life of 4-8 hours (Gerwitz *et al* 1978, Kaul *et al* 1986).

This technique is used in conjunction with stress testing either by exercise or chemically using drugs such as dipyridamole. <sup>201</sup>Thallium is injected intravenously at peak exercise and images are taken immediately (stress) and after a delay of 3-4 hours (redistribution), although there are variations on this basic protocol. A myocardial perfusion SPECT image in a normal heart is shown as a homogenous uptake of the tracer. By comparing stress images with delayed or redistribution images areas that show a defect in both images are considered to be infarcted or scar tissue. Ischaemic areas are shown as defects in perfusion 'cold spots' on stress images only (Phost *et al* 1977).

<sup>201</sup>Thallium SPECT imaging is a widely available relatively cheap method of imaging the myocardium. However it is limited in that absolute quantification of myocardial perfusion is not possible, as it is not possible to measure the concentration of <sup>201</sup>thallium within the myocardium. This method is unable to correct for attenuation of photons, so the number of counts is dependant upon the depth, and is limited by its sampling frequency. Relative quantification relates a scaling factor to the pixel counts across the tomographic image, enabling a comparison of uptake in various regions of the myocardium. Another method of quantifying myocardial perfusion is to compare the study with a database of normal perfusion distributions (Garcia *et al* 1985).

#### **1.2.2.V Contrast echocardiography**

This technique uses echo (ultrasound) contrast enhancing agents in the form of microbubbles or sonicated albumin particles to assess myocardial perfusion. These contrast enhancing agents can be administered either by peripheral venous injection or by intracoronary injection (Feinstein *et al* 1990). The microbubbles can be smaller than red blood cells, and are able to pass through the microvasculature, but will ultimately collapse.

Echocardiographic images which are taken in cross section, can be analysed using videodensitometry. The principle uses a grey scale to assess indicator concentration at two sequential locations in the vessel, to determine the transit time of a bolus of contrast agent between the two points.

This is a relatively simple, non ionising technique that can rapidly be repeated to assess the effectiveness of revascularisation procedures (Ito *et al* 1992). However it is not possible to quantitatively assess myocardial perfusion using this technique as it is not possible to assess tissue concentration of the contrast agent. There is a variable relationship between signal intensity and contrast medium concentration, and calibration is difficult (Rovai *et al* 1993).

#### **1.2.2.VI Ultrafast x-ray computed tomography**

This is able to measure myocardial blood flow during first pass of a bolus of iodinated contrast agent injected intravenously into either a central vein or the aortic root. Cross-sectional images are obtained rapidly are acquired during the passage of the bolus, and myocardial contrast agent concentration is expressed as a Hounsfield number (Rumberger *et al* 1987).

This method has been validated using radioactive microspheres in dogs (Weiss *et al* 1989, 1994), and can be used for repeat measurements of myocardial perfusion within minutes. However it is limited in that the technique is invasive and involves ionising radiation.

### **1.3 The History of MRI**

The ability of magnetic fields to affect atoms was first observed by the Dutch physicist Pieter Zeeman. He demonstrated that if a sodium atom was placed in a strong magnetic field, then its optical spectrum would be affected. This was termed the “Zeeman



effect” (Zeeman 1897), and an Irish physicist, Joseph Larmor (1897) introduced the “Larmor equation” describing the dependence of nuclei precession frequency upon strength of the external magnetic field. In 1924 the existence of the intrinsic magnetic moment or field of the atom was demonstrated by Gerlach and Stern (1924). Rabi *et al* (1938, 1938, 1939) were the first to make direct measurements of nuclear magnetic resonance (NMR). The term NMR was coined by Rabi; nuclear because only the nuclei of the atoms react, magnetic because this phenomenon occurs in a magnetic field and, resonance because of the dependence of field strength and frequency. For their work on atomic and nuclear magnetic phenomena, both Stern and Rabi received the Nobel prize for physics, Stern in 1943, and Rabi in 1944.

Work continued in NMR, much of it pioneering, but unsuccessful in demonstrating the phenomena in bulk matter (Gorter 1936, Gorter *et al* 1942). In 1946 the first successful demonstration of NMR in a solid object was published. Two independent groups working on opposite coasts of the United States America, published articles in issues of Physical Review (Bloch 1946, Bloch *et al* 1946, Purcell 1946). Felix Bloch, Wilford Hansen, and Martin Packard were based at Stanford University, whilst the other team were based at Harvard University and comprised of Edward Purcell, Henry Torrey and Robert Pound. The importance of the demonstration of NMR in solids was recognised in 1952 when the Nobel Prize for physics was jointly awarded to Bloch and Purcell.

The ‘Bloch equations’ which is the basis of analysing NMR experiments was also developed by Felix Bloch and published in 1946. The concepts of a ‘thermal or longitudinal’ relaxation time ( $T_1$ ), and a ‘transversal’ relaxation time ( $T_2$ ) were introduced by him together with the rationale for the use of substances known today as contrast agents.

In 1948, a Dutch physicist, Nicholaas Bloembergen, working with Purcell and Pound, published a theory of nuclear magnetic relaxation (Bloembergen *et al* 1948). This theory has been widely applied and has become known as the BPP theory. In 1981, Bloembergen received the Nobel prize for physics.

In order to sustain the NMR signal over a longer period of time, the spin echo was developed in 1950, by Erwin Hahn. The technique was later improved by Herman Carr and Edward Purcell (1954). Further work was done by Saul Meiboom and David Gill (1958), to produce the Carr-Purcell-Meiboom-Gill spin echo pulse sequence, one of the standard imaging pulse sequences.

The analysis of magnetic resonance by Fourier transform techniques was introduced, by Richard Ernst and Weston Anderson (1966). It was applied to the study of molecular dynamics by Robert Vold (1968), and Raymond Freeman (Freeman *et al* 1969). Their experimental techniques later led to the second standard imaging sequence, the inversion recovery pulse sequence.

Early work in NMR centred upon chemical shift. This is a specific change in the resonant frequency of a nucleus dependant upon the compound the nucleus is in. Essentially this phenomenon is a 'finger print' of the chemical compound, and led to the development of NMR spectroscopy, enabling chemists to demonstrate the structure of compounds.

NMR techniques began to be applied to study biologic systems. NMR was used by Thomas Shaw *et al* (1950, 1951, 1952, 1953), to monitor the water content of food. Erik Odeblad and his team studied the NMR properties of human tissues and secretions (1955, 1956, 1957, 1958, 1959, 1966, 1968). A method for the measurement of blood flow rates 'arterial spin tagging' was also created at this time by Jerome Singer (1959, 1960). This was eventually used together with Oliver Morse, to quantitate blood flow (1970).

Researchers also applied NMR to study the structure of water in living micro-organisms. A Mexican scientist Jorge Cerbón, first alluded to the theory of 'free' and 'bound' water in living cells (1964). His other observations of the behaviour of lipid NMR signal and ionic concentration in NMR of micro-organisms (Cerbón 1965), led to a separate line of NMR research, ionic complexing in muscle tissue (Cope 1965, 1967, Martinez *et al* 1969, Czeisler 1970).

NMR spectra of water in many living systems were investigated by many researchers in order to obtain evidence for the existence of 'ordered water' (Bratton *et al* 1965, Bruskov 1966, Koga *et al* 1966, Sussman *et al* 1966, Chapman *et al* 1967, Fritz *et al* 1967, Abetsedarskaya *et al* 1968, Cope 1969, Hazelwood *et al* 1969, Hansen 1971, Cooke *et al* 1971, Hazelwood *et al* 1971).

The discrimination of malignant tumours from normal tissue using NMR was first reported by Raymond Damadian (1971). He found that the hydrogen relaxation time constants  $T_1$  and  $T_2$  were significantly longer in rat tumours compared to normal tissue. This work was rapidly reproduced by other researchers (Chang *et al* 1972, Iijima *et al* 1973, Weisman *et al* 1972, Hollis *et al* 1972).

The first NMR image of a heterogeneous object was published in *Nature* by Paul Lauterbur (1973). He obtained a one dimensional image of two glass capillary tubes, one containing water was placed inside a larger tube containing D<sub>2</sub>O. Lauterbur achieved this by applying a second weaker magnetic field, called a gradient field, to a strong static magnetic field. As the radiofrequency is proportional to the strength of the magnetic field, the location of the nuclei could be calculated. This new imaging technique was termed 'zeumatography' by Lauterbur, from the Greek word *zeugma* meaning 'that which joins together.' This was used because the two magnetic fields (static and gradient), must both come together in the object to form the image. However this term was never widely used, and the technique was generally called NMR imaging. In the mid 1980's with the advent of clinical imaging the word 'nuclear' was dropped due to unpopular connotations for the general public.

A mouse was used as the subject for the first images of a live animal, published by Damadian *et al* (1976). The first image of a human torso was then published by Damadian *et al* (1977), showing a cross section through the eight thoracic vertebra, and was closely followed by other human studies (Hinshaw *et al* 1977, Andrew *et al* 1977).

NMR signals were very weak and prone to noise artefacts. This was improved by adding several thousand measurements, but then data acquisition took several hours. For NMR to become a clinically useful tool, developments in instrumentation and faster imaging sequences were required.

Data acquisition was speeded up by Peter Mansfield *et al* working at Nottingham University. Damadian's technique had sampled a tissue region one point at a time whereas, Mansfield's technique would sample one line at a time. Mansfield's initial image of his finger (1976), was later followed by images of the abdomen (1978). Imaging was further improved by the development of the 'spin warp' method, developed at Aberdeen University (Edelstein *et al* 1980).

Smith *et al* published work showing the use of NMR to differentiate benign from malignant tissue (1981). Young *et al* at Hammersmith, demonstrated the superior ability of NMR compared to computed tomography to show areas of demyelination in patients with multiple sclerosis (1981), and the posterior fossa (1981).

As clinical imaging has developed, so has the use of contrast agents. These are substances that affect the relaxation rates ( $R_1=1/T_1$ ,  $R_2=1/T_2$ ) of tissues and in combination with imaging sequences can increase tissue contrast. Bloch first described the use of a

paramagnetic salt (ferric nitrate) to enhance the relaxation rate of water (Bloch *et al* 1948). As mentioned earlier in the text, Bloembergen *et al* (1948) published a theory of nuclear magnetic relaxation which has been developed (Solomon 1955, Bloembergen 1957).

The first demonstration of a paramagnetic metal ion enhancing the relaxation rate of water by binding to a macromolecule was by Einsinger *et al* (1961). This phenomenon, known as proton relaxation enhancement, has been used to study the hydration and structure of metalloenzymes (Mildvan 1974, Burton *et al* 1979).

The feasibility of paramagnetic agents to discriminate tissues on the basis of differential water proton relaxation times was applied by Lauterbur *et al* (1978). Dogs with an occluded coronary artery were injected with a manganese salt, known to preferentially localise normal from infarcted myocardium. The longitudinal proton relaxation rates ( $R_1$ ) correlated with manganese concentration, enabling normal myocardium to be distinguished on the basis of relaxation behaviour. This has also been shown by other studies (Brady *et al* 1982, Goldman *et al* 1982).

Young *et al* performed the first human studies involving paramagnetic agents where enhancement of the gastrointestinal tract was achieved by the oral administration of ferric chloride (1981). The demonstration of the diagnostic potential of paramagnetic contrast agents was first shown by Carr *et al* (1984), by the enhancement of cerebral tumours in regions where there was capillary breakdown. He demonstrated this in patients using the intravenous administration of gadolinium (III) diethylenetriaminepentaacetic acid (Gd-DTPA).

Advances in hardware design including superconducting magnets, enabling high magnetic field strengths have led to better images. When this is combined with faster imaging sequences, it has enabled the imaging of moving structures such as the heart. Magnetic resonance imaging (MRI) as the technique has become to be known, has gained wide and practical acceptance today.

## **1.4 Cardiac MRI**

Imaging of the heart requires physiological gating to reduce the loss of signal from moving structures. Three forms of gating can be used: respiratory gating, a pulse oximeter or electrocardiographic gating (ECG). The latter is the most effective form in practise.

### 1.4.1 The cardiac cycle

The cardiac cycle is initiated in the sino-atrial (SA) node and is shown in Figure 1.2. This is located in the right atrium, which then becomes depolarised. The change in electrical potential produced the P wave on the ECG trace, shown in Figure 1.3, and signals atrial contraction.

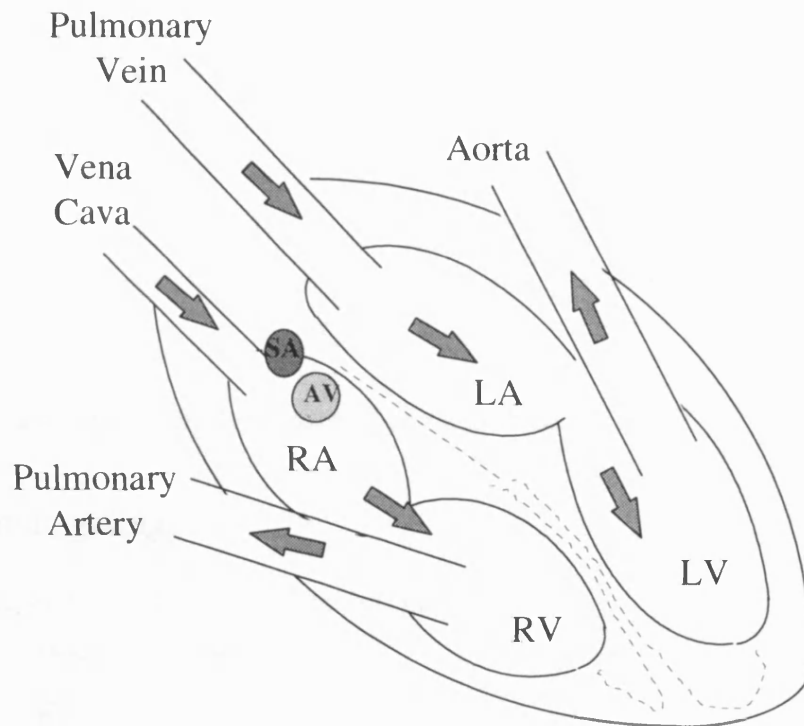


Figure 1.2 is a schematic representation of the heart. The chambers LA, LV, RA, and RV are the left atrium, left ventricle, right atrium and right ventricle respectively. The arrows indicate the movement of the blood through the chambers. Blood enters the right atrium of the heart through the Vena Cava, having travelled around the body. Atrial contraction moves blood into the ventricle. When the right ventricle contracts blood is pumped into the Pulmonary artery, where it is taken to the lungs. On its return to the heart, blood enters the left atrium, and is eventually pumped by the left ventricle into the Aorta, to travel around the body. SA indicates the location of the Sino-atrial Node, which is the ‘pacemaker’ of the heart. AV indicates the location of the atrioventricular node, where atrial contraction is detected. The electrical signal then travels along the dotted lines to both ventricles.

The excitation pulse is detected in the atrio-ventricular node (AV), and continues to travel along the interventricular septum towards the apex and into the free walls of both ventricles. Ventricular depolarisation generates the QRS waves just before ventricular contraction (ventricular systole). Repolarisation of the ventricles produces the T wave.

Assessment of the heart at end diastole i.e. during isovolumic contraction, image data should be acquired just at the peak of the R wave. Images of the heart at end systole i.e. during isovolumic relaxation, image data should be acquired at the downslope of the T wave.

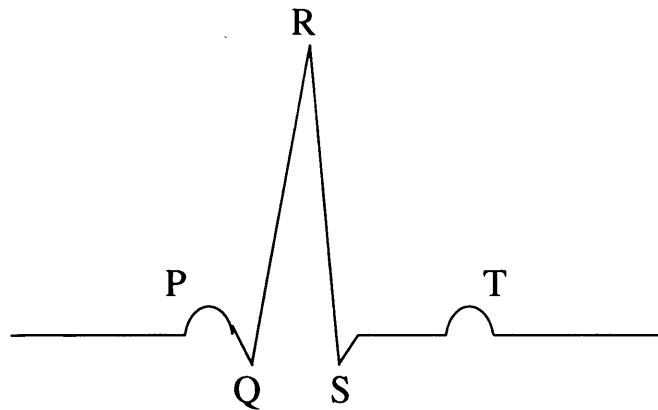


Figure 1.3 is a schematic representation of an ECG trace.

### 1.4.2 Cardiac gating

There are two main types of cardiac gating;

- a) Prospective gating
- b) Retrospective gating.

Prospective gating initiates the imaging sequence at a fixed point in the cardiac cycle, so image acquisition is synchronised to a point in the cardiac cycle. This is usually applied to imaging sequences where the signal acquisition is triggered by the R wave. This method can be used to obtain either a single slice image or multislice images.

Retrospective gating is the continuous application of the pulse sequence to acquire images during an independent recording of the ECG trace. This method is used for fast imaging sequences, and these are not synchronised to the ECG trace. When the scan is completed, the ECG trace is used to reconstruct the acquired images at the various phases of the cardiac cycle.

### **1.4.3 The Magnetohydrodynamic effect**

A clearly defined R wave to trigger imaging is required to obtain high quality cardiac images. The magnetohydrodynamic (MHD) effect is an artefact on an ECG trace which hinders the gating of image acquisition to the cardiac cycle.

This is caused by a voltage being introduced by flowing blood (conductor) in the magnetic field of the scanner. This is based on the principle of electromagnetic induction described by Faraday.

The significance of this effect for cardiac imaging is that the ECG can be altered to produced an indistinct R wave relative to relative to the T wave. The effect is dependant upon magnetic field strength, blood velocity and cardiac orientation.

Maximising the detection of the physiological ECG activity whilst minimising the sensitivity to the MHD potential is the main goal of ECG gating. The adequate placement of ECG leads can reduce the amount of artefact detected on the ECG. The optimum position of the leads varies according to the cardiac axis, which may vary between individuals.

## **1.5 Aims of the thesis**

In MR imaging, a measure of absolute myocardial perfusion (in ml/min/g) is not possible at present because the MR signal is not directly related to the tissue concentration of the contrast agent. Until the concentration of the bolus can be tracked in its journey through the tissue, tracer kinetic models enabling perfusion to be calculated cannot be applied.

This thesis aims to:

- a) Evaluate the current state-of-the-art methods of perfusion measurement.
- b) Assess whether MRI could be a useful tool for measuring myocardial perfusion
- c) Understand the difficulties of using MRI, and to try to correct the errors which are introduced by the simplistic use of MRI.
- d) Investigate the properties of a new MRI contrast agent Gd-BOPTA.

## 1.6 References

- Abetsedarskaya LA, Miftakhutdinova FG, Fedotov VD. State of water in live tissues (results of investigations by the NMR-spin echo method). *Biophysics* 13:750-757 1968
- Andrew ER, Bottomley PA, Hinshaw WS *et al.* NMR images by the multiple sensitive point method: application to larger biological systems. *Phys Med Biol* 22:971 1977
- Bloch F, Hanson WW, Packard ME. Nuclear induction. *Phys Rev* 69:127-129 1946
- Bloch F. Nuclear induction. *Phys Rev* 70: 460-474 1946
- Bloch F, Hansen WW, Packard ME. The nuclear induction experiment. *Phys Rev* 70: 474-485 1946
- Bloembergen N, Purcell EM, Pound RV. Relaxation effects in nuclear magnetic resonance absorbtion. *Phys Rev* 73:679-712 1948
- Bloembergen N. Proton relaxation times in paramagnetic solutions. *J Chem Phys.* 27:572-373 1957.
- Brady TJ, Goldman MR, Pykett IL *et al.* Proton nuclear magnetic resonance imaging of regionally ischaemically canine hearts: effects of paramagnetic proton signal enhancement. *Radiology* 144:343-347 1982
- Bratton CB, Hopkins AL, Weinberg JW. Nuclear magnetic resonance studies of living muscle. *Science* 147:738-739 1965
- Bruskov VI. Use of the method of nuclear magnetic resonance in biological research. *Biophysics* 11:223-236 1966
- Burton DR, Forsen S, Karlstrom G, Dwek RA. Proton relaxation enhancement (PRE) in biochemistry: a crtical survey. *Prog NMR Spectrosc* 13:1 1979



Carr DH, Brown J, Bydder GM *et al.* Intravenous chelated gadolinium as a contrast agent in NMR imaging of cerebral tumors. *Lancet* 1:484-486 1984

Carr HY, Purcell EM. Effects of diffusion on free precession in nuclear magnetic resonance experiments. *Phys Rev* 94:630-638 1954

Cebón J. Nuclear magnetic resonance of water in microorganisms. *Biochim Biophys Acta* 88:444-447 1964

Cebón J. Variations of the lipid phase of living microorganisms during the transport process. *Biochim Biophys Acta* 102:449-458 1965

Chang DC, Rorschach HE, Nichols BL, Hazelwood CF. Pulsed NMR studied on water in biological tissues. *Bull Am Phys Soc Ser 2* 17:328 1972

Chapman G, McLauchlan KA. Oriented water in the siatic nerve of the rabbit. *Nature* 215:391-392 1967

Cooke R, Wien R. The state of water in muscle tissue as determined by proton nuclear magnetic resonance. *Biophys J* 11:1002-1017 1971

Cope FW. NMR evidence for complexing  $\text{Na}^+$  in muscle, kidney, and brain and by Actinomycin: the relation of cellular complexing of  $\text{Na}^+$  to water and to transport kinetics. *J Gen Phys* 50:1353-1357 1967

Cope FW. Nuclear magnetic resonance evidence for complexing of sodium ions in muscle. *Proc Natl Acad Sci* 54:225-227 1965

Cope FW. Nuclear magnetic resonance evidence using  $\text{D}_2\text{O}$  for structured water in muscle and brain. *Biophys J* 9:303-319 1969

Czeisler JL, Fritz OG, Swift TJ. Direct evidence from nuclear magnetic resonance studies for bound sodium in frog skeletal muscle. *Biophys J* 10:260-268 1970

Damadian R, Goldsmith M, Minkoff L. NMR in cancer. XVI. FONAR image of the live human body. *Physiol Chem Phys* 9:97-108 1977

Damadian R, Minkoff L, Goldsmith M *et al.* Field focusing nuclear magnetic resonance (FONAR): Visualisation of a tumor in a live animal. *Science* 194:1430-1432 1976

Damadian R. Tumor detection by nuclear magnetic resonance. *Science* 171:1151-1153 1971

De Bono DP, Samani NJ, Spyt TJ, Hartshorne T, Thrush AJ, Evans DH. Transcutaneous ultrasound measurement of blood-flow in internal mammary artery grafts. *Lancet* 339:379-381 1992

Doppler CJ. Uber das farbige Licht der Dopplesterne. *Abhandlungen der Konig-lichen Bohmischen Gesellschaft der Wissenschaften* 2:465 1842

Doucette JW, Corl PD, Payne HM, *et al.* Validation of a doppler guide wire for intravascular measurement of coronary flow velocity. *Circulation* 85:1899-1911 1992

Edelstein WA, Hutchinson JMS, Johnson G, Redpath TW. Spin warp NMR imaging and application to human whole body imaging. *Phys Med Biol* 25:751-756 1980

Eisinger J, Shulman RG, Blumberg WE. Relaxation enhancement by paramagnetic ion binding in deoxyribonucleic acid solutions. *Nature* 192:963-964 1961

Ernst RR, Anderson WA. Application of fourier transform spectroscopy to magnetic resonance. *Rev Sci Instr* 37:93-102 1966

Feinstein SB, Cheirif J, Ten Cate FJ *et al.* Safety and efficacy of a new transpulmonary ultrasound contrast agent: initial multicentre clinical results. *J Am Coll Cardiol* 16:316-314 1990

Freeman R, Hill HDW. Fourier transform study of NMR spin lattice relaxation by 'progressive saturation.' *J Chem Phys* 54:3367-3377 1971.

Freeman R, Hill HDW. High resolution studies of nuclear spin-lattice relaxation. *J Chem Phys* 51:3140-3141 1969

Freeman R, Hill HDW. High resolution study of NMR spin echoes: 'J spectra.' *J Chem Phys* 54:301-313 1971.

Fritz OG, Swift TJ. The state of water in polarized and depolarized frogs nerves. *Biophys J* 7:675-678 1967

Ganz W, Tamura K, Marcus HS *et al.* Measurement of coronary sinus blood flow by continuous thermodilution in man. *Circulation* 44:181-195 1971

Garcia EV, Van Train K, Maddahi J *et al.* Quantification of rotational thallium-201 myocardial tomography. *J Nucl Med* 26: 17-26 1985

Gehring PJ, Hammond PB. The interrelationship between thallium and potassium in animals. *J Pharmacol Exp Ther* 155:187 1967

Gerlach W, Stern O. On the position of the quantum lines in a magnetic field. *Ann Phys* 74:675-699 1924

Gerwitz H, O'Keefe DD, Pohost GM, Strauss HW, McIllduff JB, Daggett WM. The effect of ischaemia on thallium-201 clearance from the myocardium. *Circulation* 61:791-797 1980

Goldman MR, Bradt TJ, Pykett IL *et al.* Quantification of experimental myocardial infarction using nuclear magnetic resonance imaging and paramagnetic ion contrast enhancement in excised canine hearts. *Circulation* 66:1012-1016 1982

Gorter CJ, Broer LJF. Negative result of an attempt to observe nuclear magnetic resonance in solids. *Physica* 9:591-596 1942

Gorter CJ, Kronig R De L. On the theory of absorption and dispersion in paramagnetic and dielectric media. *Physica* 3:1009-1020 1936

Gorter CJ. Negative result of an attempt to detect nuclear magnetic spins. *Physica* 3:995-998 1936

Gorter CJ. Paramagnetic relaxation in a transversal magnetic field. *Physica* 3:1006-1008 1936

Gorter CJ. Paramagnetic relaxation. *Physica* 3:503-514 1936

Gould KL, Mozersky DJ, Hokanson DE, Baker DW, Kennedy JW, Sumner DS, Strandness DE. A non invasive technic for determinating patency of saphenous vein coronary bypass grafts. *Circulation* 46:595-600 1972

Green MA, Mathias CJ, Welch MJ *et al.* Copper-62-labeled pyruvaldehyde Bis(N<sup>4</sup>-methylthiosemicarbazonato) copper(II): Synthesis and evaluation as a positron emission tomography tracer for cerebral and myocardial perfusion. *J Nuc Med* 31:1989-1996 1990

Hahn EL. Spin echoes. *Phys Rev* 80:580-594 1950

Hansen JR. Pulsed NMR study of water mobility in muscle and rat brain tissue. *Biochim Biophys Acta* 230:482-486 1971

Hartley CJ, Cole JS. An ultrasonic pulsed Doppler system for measuring blood flow in small vessels. *J Appl Physiol* 37:626-629 1974

Hazelwood CF, Nichols BL, Chamberlain NF. Evidence for the existence of a minimum of two phases of ordered water in skeletal muscle. *Nature* 222:747-750 1969

Hazelwood CF, Nichols BL, Chang DC, Brown B. On the state of water in developing muscle: a study of the major phase of ordered water in skeletal muscle and its relationship to sodium concentration. *Hopkins Med J* 128:117-131 1971

Hinshaw WS, Bottomley PA, Holland GN. Radiographic thin-section image of the human wrist by nuclear magnetic resonance. *Nature* 270:722 1977

Hollis DP, Saryan LA, Morris HP. A nuclear magnetic resonance study of water in two Morris hepatomas. *Hopkins Med J* 131:441-444 1972

Iijima N, Shiroy S, Yoshida Y. *et al.* Spin echo nuclear magnetic resonance in cancerous tissue. *Physiol Chem Phys* 5:431-435 1973

Ito H, Tomooka T, Saki N *et al.* Lack of myocardial perfusion immediately after successful thrombolysis. *Circulation* 85:1699-1705 1992

Kaul S, Chester DA, Pohost GM, Strauss HW, Okada RD, Boucher CA. Influence of peak exercise heart rate on normal thallium-201 myocardial clearance. *J Nucl Med* 27:26-30 1986

Kety SS, Schmidt CF. The determination of cerebral blood flow in man by the use of nitrous oxide in low concentrations. *Am J Physiol* 143:53-66 1945

Koga S, Echigo A, Oki T. Nuclear magnetic resonance spectra of water in partially dried yeast cells. *Appl Microbiol* 14:466-467 1966

Kolin A. An electromagnetic flowmeter. Principles of the method and its application to blood flow measurements. *Proc Soc Exp Biol Med* 35:53-56 1991

Larmor J. On the theory of the magnetic influence on spectra, and on the radiation of moving ions. *Philos Magazine* 44:503-512 1897

Larmor J. The influence of a magnetic field on radiation frequency. *Proc R Soc* 60:514-515 1896-1897

Lauterbur PC, Mendonca-Dias MH, Rudin AM. Augmentation of tissue water proton spin-lattice relaxation rates by in vivo addition of paramagnetic water ions. In: Dutton PL, Leigh LS, Scarpaa A. eds. *Frontier of Biological Energetics*. New York: Academic Press p752, 1978

Lauterbur PC. Image formation by local induced interactions: examples employing nuclear magnetic resonance. *Nature* 242:190-191 1973

Lebowitz E, Greene MW, Bradley-Moore P *et al.* TI-201 for medical use. *J Nuc Med* 18:509 1977

Mansfield P, Maudsley AA. Planar and line-scan spin imaging by NMR. *Proc XIXth Congress Ampere Heidelberg* p247-252 1976

Mansfield P, Pykett IL, Morris PG, Coupland RE. Human whole body line-scan imaging by NMR. *Brit J Radiol* 51:921-922 1978

Martinez D, Silvidi AA, Stokes RM. Nuclear magnetic resonance studies of sodium ions in isolated frog muscle and liver. *Biophys J* 9:1256-1260 1969

Meiboom S, Gill D. Modified spin echo method for measuring nuclear relaxation times. *Rev Sci Instr* 29:688-691 1958

Mildvan AS. Mechanism of enzyme action. *Ann Rev Biochem* 43:357-399 1974

Morse OC, Singer JR. Blood velocity measurements in intact subjects. *Science* 170:440-441 1970

Mullani N, Goldstein K, Gould L *et al.* Myocardial perfusion with Rubidium-82. 1. Measurement of extraction fraction and flow with external detectors. *J Nuc Med* 24:898-906 1983

Mullins LJ, Moore RD. The movement of thallium ions in muscle. *J Gen Physiol* 43:759 1960

Muzik O, Beanlands RSB, Hutchins GD, Manger TJ, Nguyen N, Schwaiger M. Validation of Nitrogen-13-Ammonia tracer kinetic model for quantification of myocardial blood flow using PET. *J Nuc Med* 34:83-91 1993

Neilsen AP, Morris KG, Murdock R, Bruno FP, Cobb FR. Linear relationship between the distribution of TI-201 and blood flow in ischaemic and nonischaemic myocardium during exercise. *Circulation* 61:797-801 1980

Odeblad E, Bhar BN, Lindstrom G. Proton magnetic resonance of human red blood cells in heavy water exchange experiments. *Arch Biochem Phys* 63:221-225 1956

Odeblad E, Bjorn W. Proton magnetic resonance of human milk. *Acta Radiol* 49:389-392 1958

Odeblad E, Bryhn U. Proton magnetic resonance of human cervical mucus during the menstrual cycle. *Acta Radiol* 47:315-320 1957

Odeblad E, Lindstrom G. Some preliminary observations of the proton magnetic resonance in biologic samples. *Acta Radiol* 43:469-476 1955

Odeblad E. An NMR-method for determination of ovulation. *Acta Obstet Gynecol Scand* suppl 8:39-47 1968

Odeblad E. Biophysical composition of cervical mucus and sperm migration during treatment with Conluten and Conlunett. *Acta Obstet Gynecol Scand* suppl 8:7-19 1968

Odeblad E. Micro-NMR in high permanent field: theoretical and experimental investigations with an application to the secretions from single glandular units in the human uterine cervix. *Acta Obstet Gynecol Scand* suppl 2:1-188 1966

Odeblad E. Studies on vaginal contents and cells with proton magnetic resonance. *Ann NY Acad Sci* 83:189-206 1959

Pohost GM, Zir LM, Moor RH *et al.* Differentiation of transiently ischaemic from infarcted myocardium by serial imaging after single dose of TI-201. *Circulation* 55:294-308 1977

Purcell EM, Torrey HC, Pound RV. Resonance absorption by nuclear magnetic moments in a solid. *Phys Rev* 69:37-38 1946

Rabi II, Millmann S, Kusch P, Zacharias JR. The magnetic moments of  ${}^6\text{Li}$ ,  ${}^7\text{Li}$ ,  ${}^{19}\text{F}$ . *Phys Rev* 53:495 1938

Rabi II, Millmann S, Kusch P, Zacharias JR. The molecular beam magnetic resonance method for measuring nuclear magnetic moments. *Phys Rev* 55:526-535 1939

Rabi II, Zacharias JR, Millmann S, Kusch P. A new method for measuring nuclear magnetic moments. *Phys Rev* 53:318 1938

Rossen JD, Oskarsson H, Stenberg RG, Braun P, Talman CL, Winniford MD. Simultaneous measurement of coronary flow reserve by left anterior descending coronary artery Doppler and great vein thermodilution methods. *J Am Coll Cardiol* 20:402-407 1992

Rovai D, Ghelardini G, Trivella MG *et al.* Intracoronary air-filled albumin microspheres for myocardial blood flow measurement. *J Am Coll Cardiol* 22:2014-2021 1993

Rumberger JA, Feiring AJ, Higgins CR, Lipton MJ, Ell SR, Marcus ML. Use of ultrafast CT to quantitate myocardial perfusion: a preliminary report. *J Am Coll Card* 9:59-69 1987

Schelbert HR, Phelps ME, Hoffman EJ *et al.* Regional myocardial perfusion assessed by with N-13 labeled ammonia and positron emission computerised axial tomography. *Am J Cardiol* 43:209-218 1979

Schelbert HR, Phelps ME, Huang SC, *et al.* N-13 ammonia as an indicator of myocardial blood flow. *Circulation* 63:1259-1272 1981

Shaw TM, Elsken RH, Kunsman CH. Moisture determination of foods by hydrogen nuclei magnetic resonance. *J Agric Fod Chem* 36:1070-1076 1953

Shaw TM, Elsken RH, Kunsman CH. Proton magnetic resonance absorbtion and water content of biologic materials. *Phys Rev* 85:708 1952.

Shaw TM, Elsken RH, Palmer KJ. Nuclear magnetic resonance absorbtion in glycine. *Phys Rev* 85:762 1952



Shaw TM, Elsken RH. Investigation of proton magnetic resonance line width of sorbed water. *J Chem Phys* 21:565-566 1953.

Shaw TM, Elsken RH. Nuclear resonance absorption in hygroscopic materials. *J Chem Phys* 18:1113-1114 1950

Shaw TM, Palmer KJ. Nuclear magnetic resonance absorption in proteins. *Phys Rev* 83:213 1951.

Shelton ME, Green MA, Mathias CJ, Welch MJ, Bergmann SR. Assessment of regional myocardial and renal blood flow with copper-PTSM and positron emission tomography. *Circulation* 82:990-997 1990

Singer JR. Blood flow rates by nuclear magnetic resonance measurements. *Science* 130:1652-1653 1959

Singer JR. Flow rates using nuclear or electron paramagnetic resonance techniques with applications to biological and chemical processes. *J Appl Phys* 31:125-127 1960

Siostrzonek P, Kranz A, Heinz M *et al.* Non invasive estimation of coronary flow reserve by transesophageal Doppler measurement of coronary sinus flow. *J Am Coll Cardiol* 72:1334-1337 1993

Smith FW, Mallard JR, Hutchinson JMS *et al.* Clinical application of nuclear magnetic resonance. *Lancet* 1:78-79 1981.

Smith FW, Mallard JR, Reid A. Hutchinson JMS. Nuclear magnetic resonance tomographic imaging in liver disease. *Lancet* 1:963-966 1981

Solomon I. Relaxation processes in a system of two spins. *Phys Rev* 99:559-565 1955

Sussman MV, Chin L. Nuclear magnetic resonance spectrum changes accompanying rigor mortis. *Nature* 211:414 1966

Vold RL, Waugh JS, Klein MP, Phelps DE. Measurement of spin relaxation in complex systems. *J Chem Phys* 48:3831-3832 1968

Walsh MN, Bergman SR, Steele RL *et al.* Delineation of impaired regional myocardial perfusion by Positron Emission Tomography with H<sub>2</sub><sup>15</sup>O. *Circulation* 78:612-620 1988

Weich HF, Strauss HW, Pitt B. The extraction of TI-201 by the myocardium. *Circulation* 56:188-191 1977

Weisman ID, Bennett LH, Maxwell LR Sr, Woods MW, Burk D. Recognition of cancer *in vivo* by nuclear magnetic resonance. *Science* 178:1288-1290 1972

Weiss RM, Otoadese EA, Noel MP, DeJong SC, Heery SD. Quantitation of absolute regional myocardial perfusion using cine computed tomography. *J AM Coll Cardiol* 23:1186-1193 1994

Weiss RM, Santos RM, Ginkel DL, Grover-McKay K, Marcus ML. Quantitation of the subendocardial to subepicardial perfusion rate with cine CT. *Circulation* 80(suppl II):109 1989

Wyatt DG. Problems in measurement of blood flow by magnetic induction. *Phys Med Biol* 5:289-320 1961

Yamagishi M, Yasu T, Ohara K, Kuro M, Miyatake K. Detection of coronary blood flow associated with left main coronary artery stenosis by transesophageal Doppler color flow echocardiography. *J Am Coll Cardiol* 17:87-93 1991

Young IR, Brul M, Clarke GJ *et al.* Magnetic resonance properties of hydrogen: Imaging the posterior fossa. *AJR* 187:895-901 1981

Young IR, Hall AS, Pallis CA *et al.* Nuclear magnetic resonance imaging of the brain in multiple sclerosis. *Lancet* 2:1063-1066 1981

Zeeman P. On the influence of magnetism on the nature of light emitted by a substance.  
*Phil Mag* 43: 226-239 1897

Zimmer L, McCall D, D'Addabbo L *et al.* Kinetics and characteristics of thallium exchange in cultured cells. *Circulation* 59:138 1979

## Chapter 2: Theory

### 2.1 The basic principles of magnetic resonance.

Inside the nucleus of every atom, except that of hydrogen, are two basic types of particles, positively charged protons, and neutrons with no electrical charge. These together with orbiting electrons which are negatively charged, make up the atom. The number of protons and electrons are usually the same in order to maintain electrical neutrality, however there is often an unequal number of protons and neutrons.

The angular momentum of the nucleus is determined by the number of protons and/or number of neutrons in an atom. If there are unpaired protons or neutrons (nucleons) in a nucleus then it will have a net spin and angular momentum. Nuclear angular momentum describes the rotational motion of the nucleus and is shown in Figure 2.1. If there are no unpaired nucleons then there will be zero nuclear angular momentum.

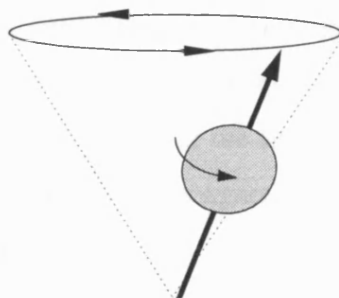


Figure 2.1 shows the angular momentum of a hydrogen atom.

#### 2.1.1 Magnetic properties of the nucleus.

Hydrogen is the simplest of all atoms with unpaired nucleons, as it has only one- a proton. This is an important atom for medical magnetic resonance imaging because it makes up nearly two thirds of all the atoms in the human body. The positively charged nucleus of a hydrogen atom has an angular momentum or spin. The effect of this is it allows the nucleus to interact with applied magnetic fields, they have a tendency to line up with them. Different nuclei have different spins, but the easiest spins to observe are those

like hydrogen with a spin quantum number of 1/2. Magnetic resonance can be performed by using any nuclei with a spin.

The nucleus of a hydrogen atom behaves like a tiny magnet when it is placed within an external magnetic field. It does this by aligning its self parallel with the north-south axis of the applied field. We find that one half of the spins will be aligned parallel with the applied magnetic field, and one half will be aligned anti parallel to this field. These two alignments correspond to the lower and upper energy states of the dipole, the difference being  $\Delta E$ . This is proportional to the magnetic field  $B_0$ , and a characteristic of the nucleus, the gyromagnetic ratio,  $\gamma$ . Finally,  $h$  is Planck's constant, which relates energy to frequency in quantum mechanics.

$$\Delta E = h \gamma B_0 \quad [2.1]$$

Due to the energy difference between the two energy states, an externally applied magnetic field creates a net excess of nuclei aligned in the lower energy state, aligned parallel to the field. This is represented by a vector called the net magnetisation ( $M$ ). Powerful magnets are used in magnetic resonance imaging and spectroscopy to make the net magnetisation large and, with the use of RF pulses, becomes observable. The alignment of protons is dependent upon the field strength. If the field is weak, there is a small energy difference between the two energy states, and protons will distribute more evenly between the parallel and antiparallel states. However, if the field is strong, then more protons will align in the upper energy state, parallel to the magnetic field, and a large net magnetisation will result. This is shown in figure 2.2.

### **2.1.2 Hydrogen magnetic resonance imaging.**

There are many elements which can be imaged using magnetic resonance techniques, but hydrogen is favoured for two major reasons;

- i) its sensitivity
- ii) its natural abundance.

Hydrogen has the highest gyromagnetic ratio ( $\gamma$ ) of any element. The larger this value is, the larger will be the  $\Delta E$  for an applied magnetic field. The sensitivity is the efficiency with which the signal is detected, and this increases with increasing signal frequency. The combination of the high gyromagnetic ratio (producing the greatest signal

per nucleus) and the abundance of hydrogen enable it to be used for imaging in the human body.

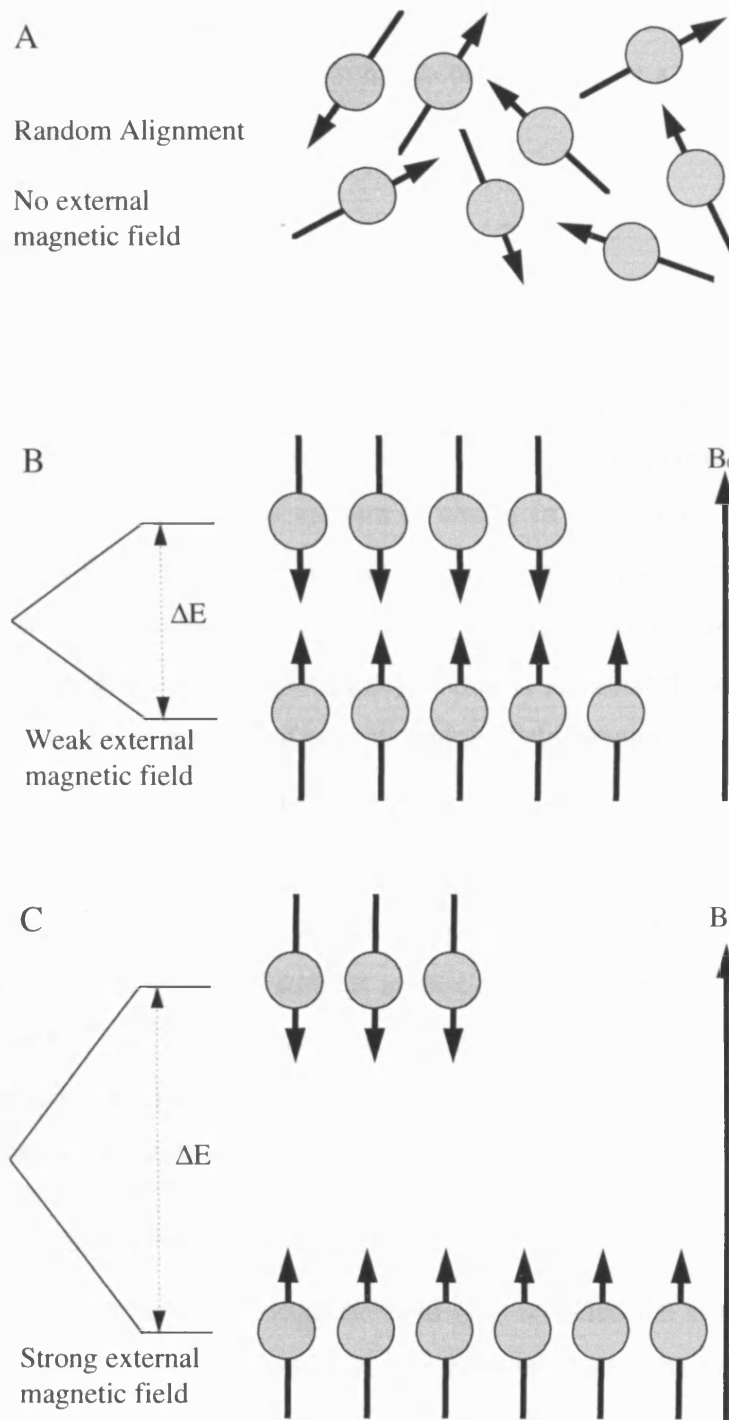


Figure 2.2 shows the alignment of the protons with the magnetic field  $B_0$ . A, shows that when there is no magnetic field there is random alignment. With the application of a magnetic field as in B, there is alignment of protons with slightly more aligning parallel than antiparallel with the magnetic field. C, shows that with the application of a strong magnetic field, even more protons will align parallel to the magnetic field.

### 2.1.3 Radio frequencies in the MR signal.

The static external magnetic field has the effect of aligning the protons and establishing an equilibrium magnetisation,  $M$ . In order to observe this magnetisation, and therefore image the body, this equilibrium has to be disrupted by a radio frequency pulse. There are two ways of looking at this process,

- I) quantum mechanically
- II) with classical theory.

#### 2.1.3.I Quantum mechanical view.

According to this theory, the magnetic field creates an energy difference between protons aligned with and against the magnetic field. A radiofrequency pulse consists of packets of energy called photons the amount of energy in each packet is dependent upon the frequency of the RF pulse. If the amount of energy in the photon matches  $\Delta E$ , then a photon absorbs energy from the RF pulse enabling it to flip from the lower energy state to the higher energy state. The special frequency required, is called the resonant or Larmor frequency, and is related to the type of nucleus and the field strength Eq.[2.2].

$$\omega_0 = \gamma B_0 \quad [2.2]$$

$\omega_0$  is the resonant frequency (radians/second),  $\gamma$  is the gyromagnetic ratio (radians/second/Tesla), and  $B_0$  is the applied magnetic field strength (Tesla). At 1 Tesla the resonance frequency of a hydrogen atom is approximately 42.6 MHz ( $\gamma=42.58$  MHz/T), this rises to 63.9 MHz at 1.5T. If spins are not irradiated at the Larmor frequency, then the nucleus is not able to resonate. Resonance results in the nucleus absorbing the RF energy, causing the magnetic moments to change their energy state.

#### 2.1.3.II Classical view.

The direction of the main magnetic field ( $B_0$ ) is called the  $z$  axis, and the plane perpendicular to this is called the  $x$ - $y$  axis or transverse plane. The net magnetisation is initially aligned along the  $z$  axis, this can be seen in figure 2.3. Spins can only be detected when their magnetisation is in the  $x$ - $y$  plane, which is achieved by using an RF pulse to rotate them into this plane.

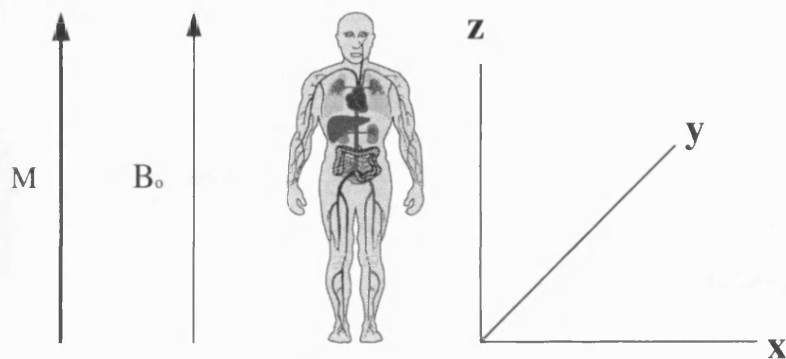


Figure 2.3 showing the axis conventions.

When placed in a magnetic field, hydrogen atoms precess at the Larmor frequency corresponding to the main magnetic field strength. By adding an oscillating RF magnetic field, the spins of the hydrogen atoms are tipped out of equilibrium. This second RF field is called the  $B_1$  field, and is produced by an oscillating current in the transmitter coil, located perpendicular to the main magnetic field. The effect of this RF pulse is to cause the net magnetisation  $M$  to be rotated away from its equilibrium alignment along the  $z$  axis. The angle with which  $M$  rotates off the  $z$  axis and into the  $x$ - $y$  plane is called the flip angle ( $\alpha$ ), and is dependent upon the amplitude or strength of the RF pulse ( $B_1$ ) and its duration ( $\tau$ ) as shown in Eq.[2.3]. This is also illustrated in figure 2.4.

$$\alpha = \gamma B_1 \tau \quad [2.3]$$

The effect of a  $90^\circ$  pulse is that it forces the phases of the individual magnetic moments into a coherent relationship. This results in an average, so the component is transverse as all the individual magnetic moments have the same phase and add together to produce an  $M$  in the  $x$ - $y$  plane and is shown in figure 2.5.

The motion of the magnetisation vectors is simplified by the use of the rotating frame of reference. Here the viewer is in effect rotating at the same rate as the magnetisation vector around the  $z$  axis. The resultant effect is that the precession appears to be frozen, and when the RF pulse is applied, the magnetisation tilts rather than spirals into the transverse plane.

When the magnetisation is in the transverse plane,  $M$  precesses around the main magnetic field. The precession of  $M$  in the transverse plane has the effect of inducing a voltage in a coil called the receiver coil, which constitutes the MR signal. The transmit and receive coils can be the same coil.



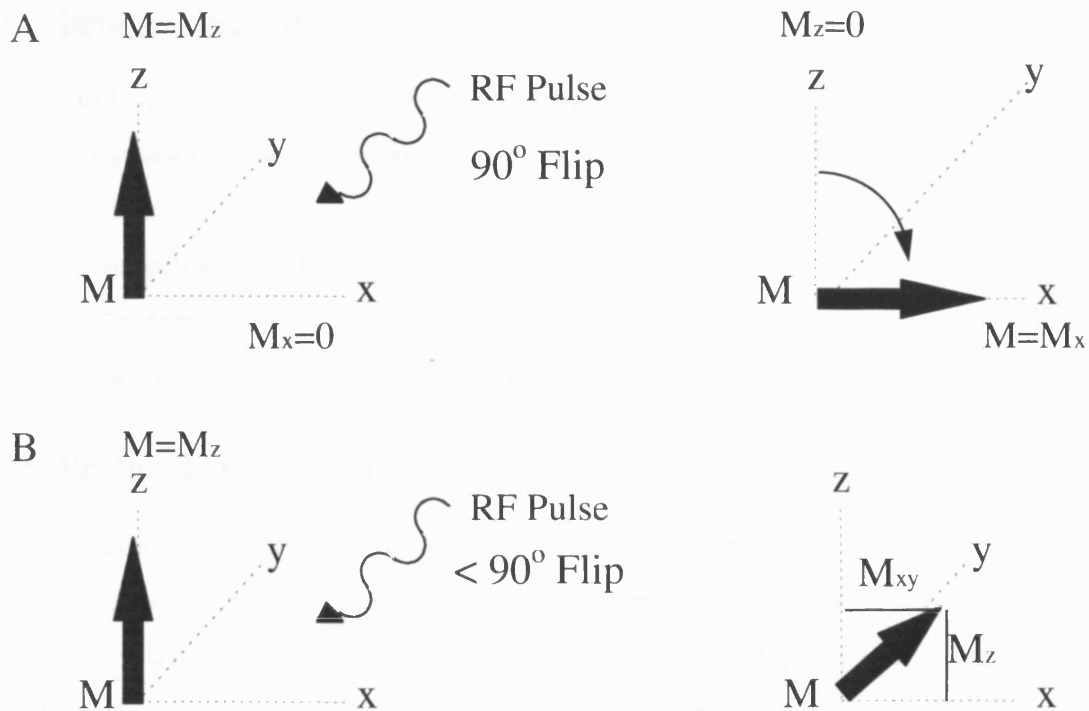


Figure 2.4 Shows the effect of the RF pulse on the  $M$  vector. The flip angle of the  $M$  vector can be controlled by the strength and duration of the RF pulse. A, shows the  $M$  vector flipped into the  $x$ - $y$  plane at 90°. This results in all the longitudinal magnetisation being flipped into transverse the transverse plane. In B, it can be seen that  $M$  has been flipped less than 90°, resulting in both a transverse and longitudinal component of  $M$ .

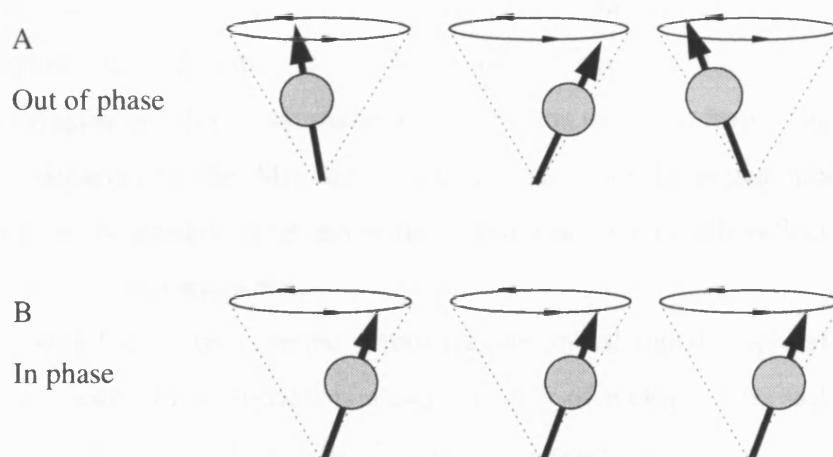


Figure 2.5 shows the precession of protons. In A, they are precessing out of phase but in B, they are precessing in coherence, which will result in a component of magnetisation  $M$ , in the transverse plane.

## 2.2 Image contrast.

Contrast refers to the difference in signal intensity between tissues, enabling them to be distinguished on an MR image. The contrast found within MR images is dependent upon three main factors:

- i) physical properties- the density of the protons,
- ii) chemical environment- the molecules hydrogen protons will interact with,
- iii) biological properties of the tissues- intact membranes and flow.

### 2.2.1 Proton density, $T_1$ , and $T_2$ .

Relaxation describes the re-establishment of equilibrium after RF excitation. There are two types of relaxation- longitudinal ( $T_1$ ) and transverse ( $T_2$ ), which can vary between tissues. Spin density is the number of spins visible by MR per volume and is often interchanged with the term proton density. This has to be distinguished from the actual number of hydrogen protons present ( $N[H]$ ) in a tissue, which cannot always be imaged using MR due to their physicochemical environment. The proton density does not vary very much between tissues.

### 2.2.2 Proton density.

The number of protons in a given volume contributes to all images, and if there are no protons there will be no image intensity, regardless of the image weighting. There are protons throughout the body, although not all can be easily imaged e.g. lungs. The protons used for MR imaging are those that make up the nucleus of the hydrogen atom. The only significant contributors to the MR signal are the nuclei of hydrogen atoms in water molecules or in some groups of fat molecules. Proton density in MR reflects the mobile subset of all protons in fat and water.

The proton density in a sample determines the initial signal amplitude of the free induction decay signal (FID). If there is a large number of protons, there will be a strong signal which will later be affected by  $T_1$  and  $T_2$  to produce a signal dependent upon imaging factors, e.g. repetition time (TR), echo time (TE). Materials with a high proton density include fats, blood, and cerebrospinal fluid (CSF). However, if there are few mobile protons in the tissue the image will be black. Materials with a low proton density will remain at a low signal level; examples include, air, calcifications, dense cortical bone,

fibrous tissue, and implanted materials such as plastics. Proton density imaging can be combined with  $T_1$  and  $T_2$  -weighted imaging to help distinguish the underlying pathology, and is illustrated in figure 2.6.

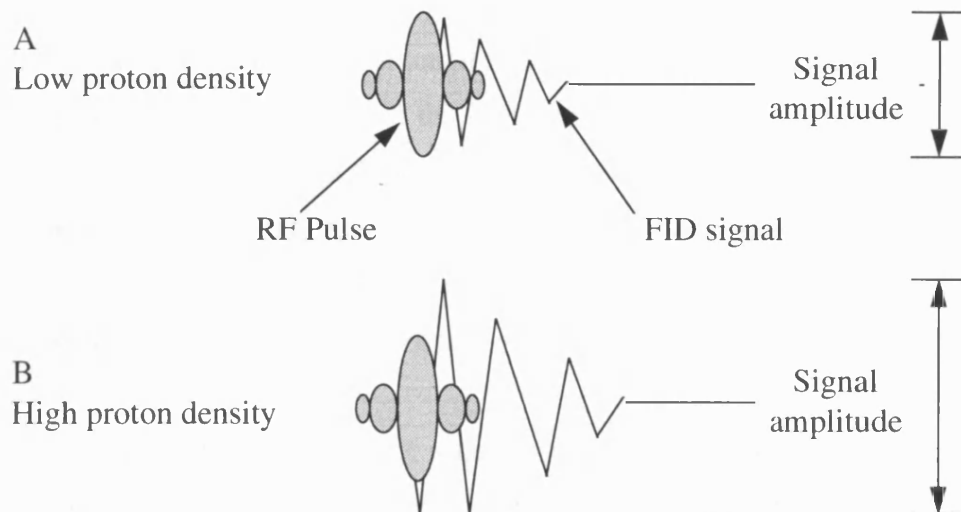


Figure 2.6 shows the effect of proton density on the amplitude of the free induction decay (FID) signal.

MR sequences with a relatively long TR and short TE are referred to as proton density or spin density images. This has the effect of decreasing both the  $T_1$  and  $T_2$  weighting resulting in a greater contribution to the image of the spin or proton density.

### 2.2.3 $T_1$ Relaxation.

MR is dependent upon there being a slight difference in energy between the parallel and antiparallel aligned nuclei. When spins are placed in a magnetic field, they are not able to instantaneously line up with the magnetic field. The time delay in the spins orientating with the magnetic field is called the spin lattice time or  $T_1$ . The lattice refers to the thermal reservoir to which the population is coupled.

The  $T_1$  in an MR imaging sequence describes the time taken by the spins to regain equilibrium after they have been excited by a  $90^\circ$  RF pulse. When the pulse is initially applied, there is no longitudinal magnetisation as it has all been tipped into the transverse plane. Slowly, the magnetisation begins to recover back to equilibrium.  $T_1$  is an exponential time constant, describing the time taken for 63% of the equilibrium longitudinal magnetisation to recover.

When imaging, several excitations are required to produce an image, with a period

TR between the excitations. An equilibrium value for the longitudinal magnetisation is reached that is a balance between the rate of  $T_1$  relaxation and the TR. This equilibrium value is reduced and is smaller than the maximal value which is determined by the proton density.

As the excitation pulse tips the longitudinal magnetisation into the transverse plane (where it is detected), the strength of the MR signal is proportional to the quantity of longitudinal magnetisation present the instant before the RF pulse was applied. If there is a long TR, there will be enough time for the protons to realign before the next excitation pulse, resulting in a strong signal. However, if the TR is short with respect to  $T_1$ , there will only be a partial realignment, and the signal will be reduced in strength. This is termed signal saturation.

Contrast is produced within MR imaging by using the differences in  $T_1$  relaxation time and translating this into differences in tissue signal intensity. Tissues that relax quickly, e.g. fat, have short  $T_1$ 's, and produce high signal whereas protons that recover slowly, have a long  $T_1$  and produce less signal. This is shown in figure 2.7.

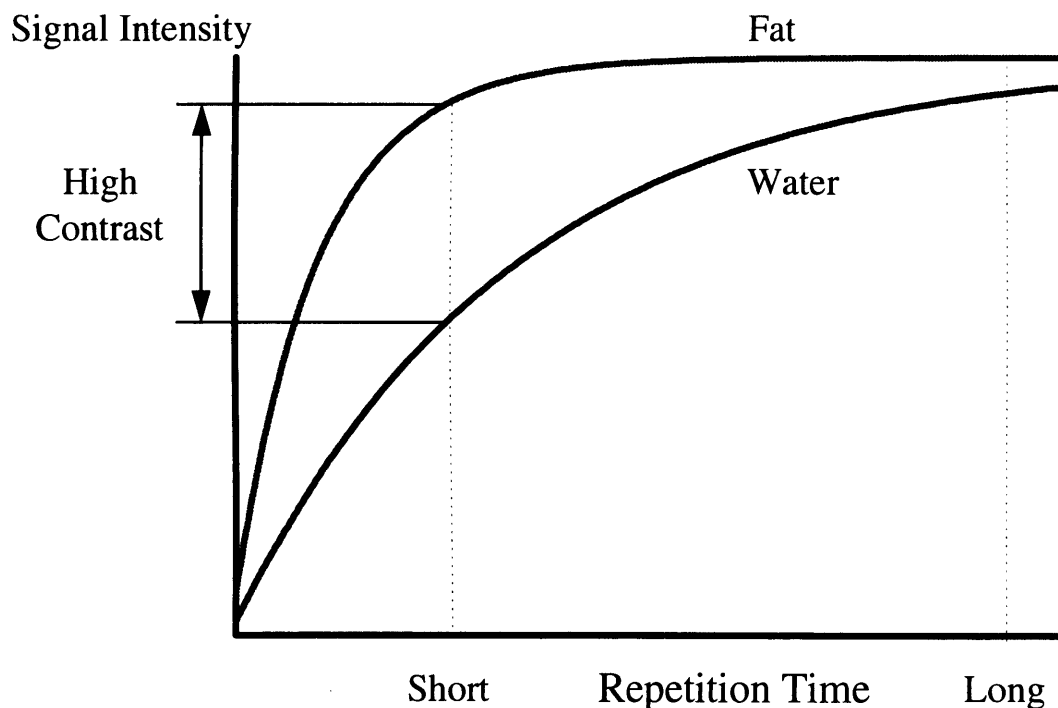


Figure 2.7 shows the effects of TR on image contrast of fat (short  $T_1$ ) and water (long  $T_1$ ). Maximal contrast is achieved in this example at short a TR.

### 2.2.4 $T_2$ Relaxation.

When protons are first tipped into the transverse plane they precess in the same phase, producing a detectable MR signal, called the FID. This signal will rapidly disappear through the process of  $T_2$  relaxation also called spin-spin relaxation as it exchanges energy with its neighbouring spins.

After the application of the  $90^\circ$  pulse, the transverse magnetisation vectors from different protons all have the same phase, called phase coherence. However, as each spin precesses at a frequency given by its local magnetic field, if there was a completely homogeneous magnetic field, the spins would remain coherent indefinitely. But, there are local magnetic field inhomogeneities, causing spins to experience slightly different magnetic fields resulting in phase dispersion or dephasing. This reduces the net transverse magnetisation, causing MR signal loss.

There are two major factors which cause local magnetic field inhomogeneities:

- i) microscopic effects related to the magnetic interactions between neighbouring molecules,
- ii) the macroscopic effect of the inhomogeneities in the applied magnetic field.

The dephasing caused by molecular interactions are related to  $T_2$ . The dephasing caused by both of these factors together are known as  $T_2^*$ . The  $T_2$  is always longer than the  $T_2^*$ , which has a rapid loss of signal. Following the RF pulse there is a rapid decay of signal due to both magnetic field inhomogeneity and from dephasing caused by a nearby molecule passing. The rapid decay of the signal is known as the free induction decay (FID), and decreases exponentially with  $T_2^*$ , that is 37% decrease after one  $T_2^*$  interval.

The transversal image contrast is dependent upon the TE. This is the time between the middle of the excitation and the middle of the read out used for the frequency encoding. By making the TE longer, i.e. shifting the readout farther from the excitation pulse, the signal loss due to transverse relaxation is increased. This is illustrated in figure 2.8.

To observe  $T_2$  decay that is purely the part of relaxation due to molecular interactions, a spin echo sequence is used. This employs a  $180^\circ$  pulse at a time TE/2 which has the effect of eliminating the static magnetic field inhomogeneities, leaving only the magnetic field fluctuations from the chemical interactions. The echo is recorded at time TE. The signal intensity from a tissue with a long  $T_2$  is greater than from a tissue with a short  $T_2$  for a given TE.

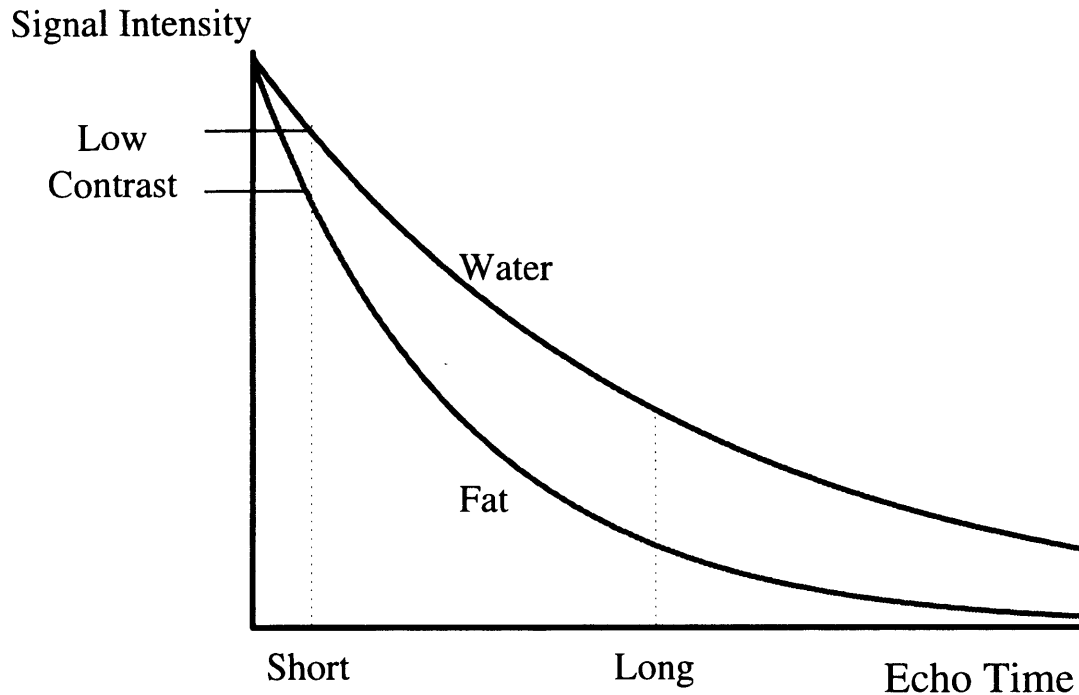


Figure 2.8 shows the effects of echo time (TE) on the image contrast of fat (short  $T_2$ ) and water (long  $T_2$ ). When a long TE is used maximal contrast is achieved between fat and water.

### 2.2.5 Molecular mechanisms for relaxation.

There are many pathways by which  $T_1$  and  $T_2$  relaxation occur. They are dependent upon close interactions between water and other molecules. Molecules are in a constant state of motion, tumbling and colliding with other molecules and they have their own minute magnetic field. These intramolecular motions and interactions produce fluctuations in the local magnetic field experienced by a proton.

A small molecule such as water moves quickly and so produces magnetic field fluctuations. Large bulky molecules such as proteins move very slowly and so produce less magnetic field fluctuations compared to water. The rate at which the magnetic field fluctuates affects longitudinal and transverse relaxation. The correlation time describes the rate of magnetic field fluctuation. With rapid molecular motion the correlation times are short and with slow motion the correlation times are long. Longitudinal relaxation occurs because the magnetic field fluctuations have a correlation time that enables magnetisation exchange between spins.

$T_1$  relaxation depends on how effectively energy is distributed back to the lattice. To optimally add energy to the system the RF field should fluctuate at the resonant or

Larmor frequency of the system. Also, for energy to be efficiently redistributed, the magnetic fields of the lattice must fluctuate at or near this resonant frequency.

Small molecules like water have a higher rate of molecular motion than the Larmor frequency and they are inefficient at returning energy to the lattice and therefore have long  $T_1$  relaxation times. If there is slower molecular motion then the magnetic field fluctuates closer to the Larmor frequency and there is a more efficient energy transfer resulting in a short  $T_1$  relaxation time. This is the case for medium-sized molecules such as cholesterol. Large molecules such as long-chain fatty acids also allow efficient  $T_1$  relaxation. This is because these molecules have a slower rate of translational molecular motion and so the magnetic field fluctuates at well below the resonant frequency of the system. However, the rotational motion of the terminal fatty acid groups is at higher frequencies enabling efficient energy transfer and short  $T_1$  relaxation times.

### **2.2.6 Protein binding and relaxation.**

Proteins and other macromolecules are in solution with body water, so it is not in a pure state. This occurs within cells and also in extracellular fluid collections. As proteins are added to pure water the rapidly moving free water becomes structured: around the macromolecules it becomes motionally perturbed but not bound. Bound water is where the hydrogen molecules are bonded to a fixed site on the macromolecule. All water molecules that are affected by macromolecules are referred to as hydration layer water. This process has the effect of slowing down the molecular motion of the water and bringing it closer to the Larmor frequency, therefore increasing its relaxation efficiency.

### **2.2.7 Factors affecting $T_2$ relaxation.**

$T_2$  relaxation is the loss of phase coherence of the precessing nuclei. This reduces the detected transverse magnetisation.  $T_2$  relaxation efficiency is increased by low frequency magnetic field fluctuations caused by large molecules and solids. These have the effect of altering the local magnetic field value by causing nuclear spins to precess at slightly higher or lower frequencies resulting in phase dispersion and loss of phase coherence. These, therefore, have short  $T_2$  relaxation times.

Small molecules such as water have high rates of molecular motion and the high frequency magnetic field fluctuations tend to average out the frequency deviations to zero.

The magnetic field is then determined by the external field and phase coherence is maintained for a longer period of time resulting in long  $T_2$  relaxation times.

## **2.3 Other sources of MR image contrast.**

The major sources of image contrast in MR imaging are  $T_1$ ,  $T_2$  and proton density as discussed. However, there are other sources of contrast which can be exploited for clinical diagnostic imaging.

### **2.3.1 Magnetic susceptibility.**

This is a material's ability to distort the applied magnetic field. All substances will respond when placed in a magnetic field. The degree to which the substance becomes magnetised or the ratio of the applied magnetic field ( $B_0$ ) to the resultant field ( $M$ ) is the substance's magnetic susceptibility ( $\chi$ ). The net induced magnetisation is generally proportional to the applied magnetic field Eq. [2.4].

$$M = \chi B_0 \quad [2.4]$$

The response of the substance to an externally applied magnetic field is determined by the electronic configuration of the component atoms i.e. the presence of unpaired electrons. The MR phenomenon is dependent upon the nucleus, but the image is also affected by whether the electrons are paired or unpaired.

Most tissues in the body have paired electrons so the spin density angular momentum is cancelled out. However, when the substance is placed in an external magnetic field the orbital momentum of each electron results in the induction of a weak magnetic field in the opposite direction to the applied field. These substances therefore have a weak negative susceptibility and are called diamagnetic.

In substances which have unpaired electrons some of the unpaired electrons respond to the external magnetic field and orient with it. If there are sufficient numbers of unpaired electrons present then this effect dominates the weaker diamagnetic effects and a strong positive magnetic susceptibility results. Substances with unpaired electrons may be paramagnetic, superparamagnetic or ferromagnetic dependent upon their degree and permanence of their magnetic field.



### 2.3.1.I Paramagnetism.

These materials exert a weak positive susceptibility where the induced magnetisation returns to zero when the applied field is removed.

Paramagnetic substances affect the MR signal by improving the efficiency of  $T_1$  and  $T_2$  relaxation. In the absence of unpaired electrons nearby protons realign with the main magnetic fields through spin-lattice and spin-spin relaxation mechanisms. This is possible due to the variation in the local magnetic fields produced by the motion of water protons. In the presence of unpaired electrons a greater magnetic dipole is produced by the larger angular momentum of the electron resulting in a more efficient proton-electron dipole-dipole interaction.

This interaction requires that the unpaired electrons have to be accessible to the water protons and will decrease as the distance increases (to the sixth power of the distance between the dipoles). This dependence on proximity usually requires the substances containing the unpaired electrons to be in an aqueous solution so the water protons can get close enough. Paramagnetic substances are endogenous as well as exogenous and examples include gadolinium, methemoglobin and melanin, and appear bright on  $T_1$ -weighted images.

When the substance with unpaired electrons cannot get close enough to the protons for proton-electron dipole-dipole interactions to occur there is another form of relaxation enhancement that occurs. This requires that the substance is heterogeneously distributed in the tissue and results in local magnetic field heterogeneity. This has the effect of varying the Larmor frequency and therefore phase of the water protons as they diffuse through the field inhomogeneities. These frequencies and phase variations are not corrected during gradient echo and spin echo refocussing. This then results in a decrease in transverse magnetisation manifested as a short  $T_2^*$  relaxation time and is shown as a low signal area on a  $T_2^*$ -weighted image.

The  $T_2^*$  relaxation enhancement is dependent upon the strength of the magnetic field and high field strength units have an advantage in detecting these effects. This type of shortening preferentially affects  $T_2$  shortening and there is no parallel effect with  $T_1$ .

### **2.3.1.II Superparamagnetism.**

These are usually crystalline structures in which the dipoles of the unpaired electrons are tightly packed. This has the effect of allowing groups of electron dipoles to act together as a unit called a domain.

Superparamagnetic substances have a much greater positive magnetic susceptibility effect than paramagnetic substances but the magnetism will return to zero when the applied magnetic field is removed. They are usually solids that act as independent domains increasing image contrast by their  $T_2$  shortening effect. Examples of these include haemosiderin and superparamagnetic iron oxide (SPIO).

### **2.3.1.III Ferromagnetism.**

These substances remain permanently magnetised even after the applied magnetic field is removed. They have interacting domains and the orientation of the magnetic dipoles reaches an equilibrium based upon the crystalline structure. It is the interacting domains that are termed ferromagnetic and they have a high positive magnetic susceptibility. Ferromagnetic materials are iron, cobalt and nickel and many of their alloys.

## **2.3.2 Contrast agents.**

Image contrast can be increased by the use of exogenous materials. These are used to provide physiologic information such as tissue perfusion or status of the blood brain barrier. This is achieved by creating changes in MR signal enhancement by the arrival and accumulation of contrast within the tissue.

An effective contrast agent alters the  $T_1$  or  $T_2$  so that a change in signal intensity is observed. Positive contrast enhancement produces a brighter tissue of interest after administration of contrast. The use of negative contrast agents darkens the target tissue in an image. The signal in an image will increase when the proton density increases or the  $T_1$  decreases or the  $T_2$  increases. The effectiveness of a paramagnetic contrast agent is expressed in terms of relaxivity. This is the slope of a graph of the relaxation rate verses the concentration of contrast agent (Young *et al* 1991). This is dependent upon field strength and temperature, and is expressed in units of  $\text{mM}^{-1} \text{s}^{-1}$ .

Most contrast agents in clinical use are paramagnetic and reduce both  $T_1$  and  $T_2$  relaxation times. At low concentrations, the  $T_1$  effects dominate, which results in a signal

intensity increase. At higher concentrations the  $T_2$  effects dominate as large susceptibilities are created due to the large number of unpaired electrons resulting in signal loss. The relationship between signal intensity and paramagnetic contrast media concentration is non linear.

### 2.3.2.I Principles of relaxation enhancement.

Paramagnetic materials are able to influence  $T_1$  and  $T_2$  relaxation times through the interactions of their unpaired electrons and the hydrogen nuclei of water molecules. The theory of these interactions has been explained by Solomon (1955) and Bloembergen (1957). Their equations are broken down into two components, a dipolar term, describing the spatial contribution to relaxivity and scalar terms which describe the contribution of contact or bonds on relaxivity.

The dipolar-dipolar part of the equation describes the magnitude of the interaction of the paramagnetic compound with the surrounding protons, and states that this is dependent upon the ability of these protons to approach the paramagnetic centre (Chang *et al* 1993).

$$R_{1,2} = q (\mu_{\text{eff}})^2 \tau_c / r^6 \quad [2.5]$$

The above equation, Eq.[2.5], predicts that the inner sphere relaxivity ( $R_{1,2}$ ) is a function of  $q$ , the number of water molecules bound per metal ion. The effective magnetic moment is described by  $\mu_{\text{eff}}$ ,  $r$  is the distance between the paramagnetic centre and the water proton and  $\tau_c$  is the correlation time. Optimal relaxation enhancement is achieved when molecules with nuclear spin are able to have access to many sites near the paramagnetic molecule, and to move in close proximity enabling inner sphere relaxation. The relaxivity is proportional to the number of water molecules in the inner sphere ( $q$ ). When a metal ion such as gadolinium ( $q=8-9$ ) is chelated to large ligands (e.g. DTPA) to reduce the *in vivo* toxicity (Mann 1993), this decreases the  $q$  to 1, and reduces its relaxivity.

The scalar component is the probability of a contact interaction between an unpaired electron from the paramagnetic metal ion and the proton nucleus of a nearby water molecule.

The correlation time  $\tau_c$ , is the minimum time required for a molecule to rotate one radian, that is to "flip" in the orientation of its magnetic field. This can be further broken down into three components Eq.[2.6],

$$\tau_c = \tau_r + \tau_s + \tau_m \quad [2.6]$$

where  $\tau_r$  is the rotational correlational time, which describes the rotation of the complex or the rotational tumbling time of the entire water-metal unit.  $\tau_s$  is the longitudinal electron spin relaxation time, and describes the time taken for electron spins to reach their equilibrium state after being disturbed. Finally,  $\tau_m$  describes the inner sphere water exchange correlation time, or rate of water exchange.

Good relaxation agents have large numbers of unpaired electrons and long electron spin relaxation times. They also allow surrounding protons (generally water) to pass close to the nucleus of the metal ion. The Larmor frequency (field strength) will also influence relaxation rates, as optimally there will be enhanced relaxation if the water-metal complex has a rotational correlation time around the Larmor frequency.

### **2.3.2.II Tissue relaxivity.**

The ability of a contrast agent to influence relaxation rates within tissues is dependent upon two factors;

- i) chemical environment
- ii) compartmentalisation of water.

In vivo, the contrast agent complex is affected by its binding to macromolecular structures. If this occurs it has the effect of increasing its rotational correlation time  $\tau_r$  and hindering its rotational mobility. In turn this increases its relaxivity.

In general, tissue water is compartmentalised into

- i) Intracellular (~80%)
- ii) Interstitial, composed of fluid spaces between cells and capillaries (~15%)
- iii) Intravascular (~5%)

Contrast agents will affect the magnetisation of water within the tissue, but some compartments will contain the contrast agent and others will not. As there is an exchange of water molecules between compartments the magnetisation of water molecules in compartments without contrast can be affected by compartments with contrast agent. In this situation it is the exchange of water between the tissue compartments which determines the effect of the contrast agent upon the tissue.

There will be a monoexponential relaxation rate when there is a fast movement of water between tissue compartments relative to  $T_1$ . In this case even though the contrast

agent may be confined to a single compartment, the exchange of water has the effect of averaging the relaxation rates between compartments.

Where water exchange between compartments is slower than the relaxation of magnetisation there will be no averaging of the relaxation between the compartments (McLoughlin *et al* 1973). Here water magnetisation relaxes with multiple time constants, with each compartment separately being affected by the relaxation of water. The MR signal is obtained from water in all tissue compartments. When the exchange of water is not fast, care has to be taken in interpreting the signal intensity information, as this can lead to errors in predicting physiological parameters (Donahue *et al* 1994) .

### **2.3.3 Flow**

If protons move during the MR imaging sequence, the MR signal will change. Flow effects can be seen in two ways;

- i) Time of flight. This affects the longitudinal magnetisation and is dependent upon the radiofrequency history of the spins. This also varies according to whether spin echoes or gradient echoes are used for imaging.
- ii) Phase shift. There is a phase accumulation by flowing protons. This is because as spins move along the gradient this alters the phase of the transverse magnetisation.

### **2.3.4 Blood and haemorrhage.**

Blood has a high water content and therefore a high proton density and long  $T_1$  relaxation time which is dependent upon haematocrit. The  $T_2$  relaxation time is dependent upon the oxygen saturation of blood as deoxyhaemoglobin is strongly paramagnetic.

Haemorrhage has a variety of appearances on MR images. When fresh arterial blood is filling a haemorrhage, this has a long  $T_1$  and  $T_2$ , so appears dark on  $T_1$ -weighted images and bright on  $T_2$ -weighted images. As the blood becomes deoxygenated, it has a dark appearance on  $T_2$  and  $T_2^*$ -weighted images. When the haemoglobin is converted to methemoglobin which allows better water access to the iron group, the  $T_2^*$  effect is then lost. This is replaced by an enhancement on  $T_1$ -weighted images. Finally, iron is broken down and removed.

### 2.3.5 Chemical shift

This refers to the difference in resonant frequency of protons due to the differences in their chemical environments. The electron cloud that surrounds the nucleus of an atom shields it from the applied magnetic field. This has the effect of altering the magnetic field experienced by the nucleus so that its resonant frequency is shifted.

These shifts tend to be small in protons. For hydrogen atoms, there is a different resonant frequency depending upon the type of chemical bonds. Protons in water experience slightly different magnetic fields than protons in fat, independent of the applied magnetic field. This results in a slightly higher resonant frequency of water (3.5ppm) compared to fat. The effect of this for imaging is that there is a mispositioning of fat signals, leading to a chemical shift artefact.

The chemical shift phenomenon is exploited within spectroscopy. Here, frequencies encode chemical information so large chemical shifts values are required. The actual shift is dependent upon the magnetic field strength, so strong magnets are needed to improve the separation of the chemical peaks.

### 2.3.6 Magnetisation transfer contrast.

During normal proton density imaging we are able to see the concentration of mobile water protons. These have a long  $T_2$  and resonate at a very narrow range of frequencies around the Larmor frequency. However there are a lot of MR invisible water protons which are associated with large immobile proteins and cell membranes. The restricted protons have very short  $T_2$ 's ( $<0.1\text{ms}$ ) so cannot be seen at TE's currently available for imaging.

To exploit the MT effect in clinical imaging systems, an RF pulse is applied at a frequency away from the resonant Larmor frequency. This off resonance pulse saturates the magnetisation in the restricted proton pool. As both pools of protons exchange magnetisation, there is a reduction in the signal intensity of the mobile protons. This effect is called magnetisation transfer (MT) contrast (Wolff *et al* 1989). Where there are no restricted protons e.g. CSF, urine and blood, there is minimal signal change.

This can be applied clinically during contrast enhanced imaging to reduce the signal from organs e.g. brain. This increases the ability to detect lesions with short  $T_1$ 's, e.g.

contrast enhanced tumours (Tan *et al* 1992), as the signal from the surrounding brain tissue is reduced due to MT saturation.

## **2.4 Basic magnetic resonance pulse sequences.**

A pulse sequence refers the timing of commands that an MR scanner uses to create images. Pulse sequences enable the effect of intrinsic tissue parameters on an image to be controlled. This enables the desired image contrast to be achieved.

The two main timings used are;

- i) TR- repetition time
- ii) TE- echo time.

TR is the time from the beginning of the first RF pulse ( $90^\circ$  in spin echo imaging), through the entire pulse sequence, until the first pulse is applied to start the process again. This affects the signal intensity through longitudinal relaxation.

TE is the time from the beginning of the first RF pulse ( $90^\circ$  in spin echo imaging) to the time the echo is received. This affects signal intensity through transverse relaxation.

### **2.4.1 Spin echo imaging.**

This is the most common pulse sequence used in clinical MR imaging. It consists of two RF pulses,  $90^\circ$  and  $180^\circ$  which are separated by a time interval of  $TE/2$ , and is illustrated in figure 2.9.

Before the application of the  $90^\circ$  RF pulse some of the magnetisation points along the  $+z$  axis, called longitudinal magnetisation. The  $90^\circ$  RF pulse tips all the available longitudinal magnetisation into the transverse  $x$ - $y$  plane. Here the strength of the precessing magnetisation can be measured. This pulse produces a free induction decay (FID) signal which rapidly decays because of the dephasing of the protons as they are located in slightly different magnetic fields.

After a short time  $TE/2$  a  $180^\circ$  RF pulse is applied. This has the effect of rephasing the transverse magnetisation which had begun to lose phase coherence. This is because some of the protons precess faster than others. At a time  $TE$  an echo is formed as a result of all the protons precessing at the same phase. This is called a spin echo, and this signal is measured.

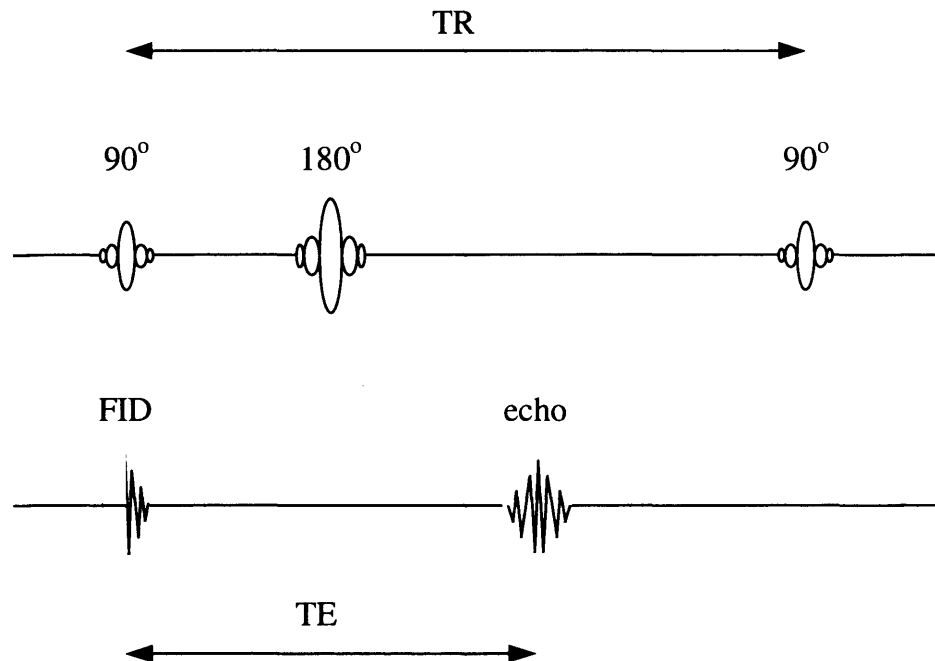


Figure 2.9 diagrammatically illustrates the spin-echo pulse sequence.

The transverse magnetisation dephases to zero after the spin echo. The longitudinal magnetisation regrows slowly. Time has to be allowed between repetitions to enable sufficient recovery of the longitudinal magnetisation. This has the effect of increasing the scan times.

#### 2.4.2 Gradient echo imaging.

This is a much faster method of MR image acquisition than the spin echo sequence, and is illustrated in figure 2.10. Here the excitation RF pulse is reduced to a smaller flip angle. This only tips some of the longitudinal magnetisation into the transverse  $x$ - $y$  plane. The  $180^\circ$  refocussing pulse is replaced by gradient reversal. Here, the initial negative lobe of the gradient dephases the transverse magnetisation. A symmetric reversal of the gradient to a positive lobe is applied at time  $TE/2$ . This rephases the reversible components of the transverse magnetisation to form an echo at time  $TE$ .

The reduction of the initial RF pulse to  $<90^\circ$  enables the reduction in  $TR$ , as less time is required for recovery of the longitudinal magnetisation. This reduces scan times.

The formation of an echo by gradient reversal does not eliminate dephasing effects caused by inhomogeneous magnetic fields as in spin echo imaging. Therefore the resultant



image is governed by a relaxation time  $T_2^*$ . This is a combination of true  $T_2$  relaxation and relaxation caused by magnetic field inhomogeneities.

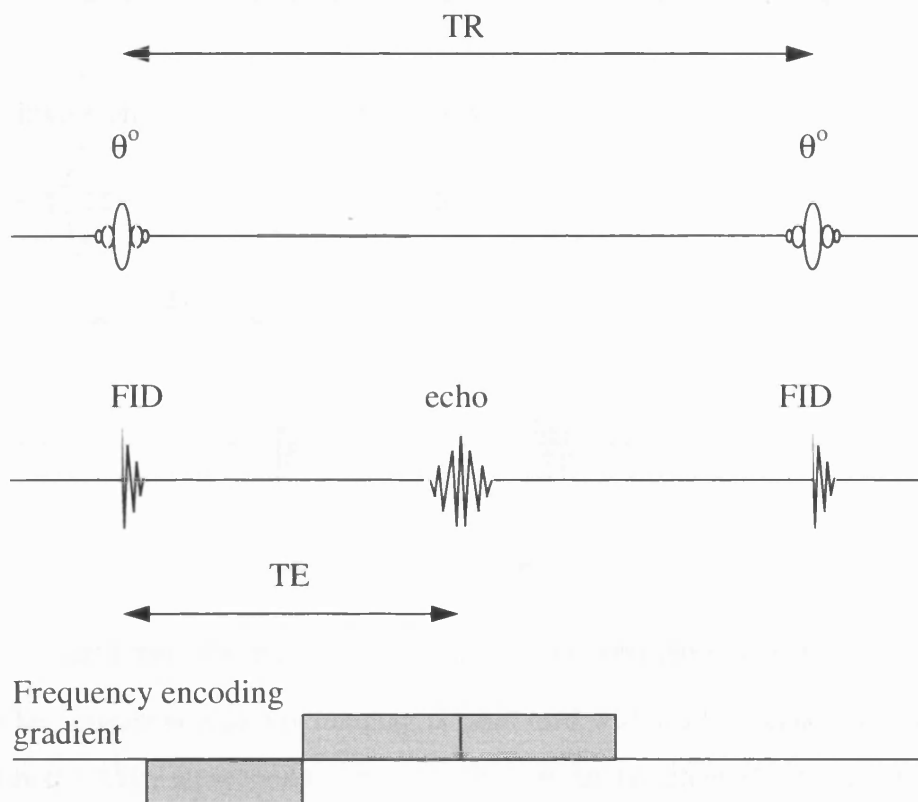


Figure 2.10 diagrammatically illustrates the gradient echo pulse sequence.

### 2.4.3 Inversion recovery.

This method of imaging prepares the magnetisation before the imaging sequence is applied (either spin echo or gradient echo). It has the effect of producing images with high  $T_1$  contrast. This is illustrated in figure 2.11.

The longitudinal magnetisation projects along the  $+z$  axis before the start of the sequence. A  $180^\circ$  inversion pulse tips the positive longitudinal magnetisation ( $+z$ ) to the negative component ( $-z$ ). A time  $TI$ , called the inversion time, enables recovery of the longitudinal magnetisation. After this either the gradient echo or spin echo sequence is applied to acquire the image.

Inversion recovery imaging has the advantage over  $T_1$ -weighted spin echo imaging in that it has a greater dynamic signal range. For spin echo imaging the  $T_1$  signal ranges

from 0 to 1. Inversion recovery imaging has a  $T_1$  signal the ranges from -1 to +1. This increase in the dynamic signal range can provide better  $T_1$  contrast between tissues.

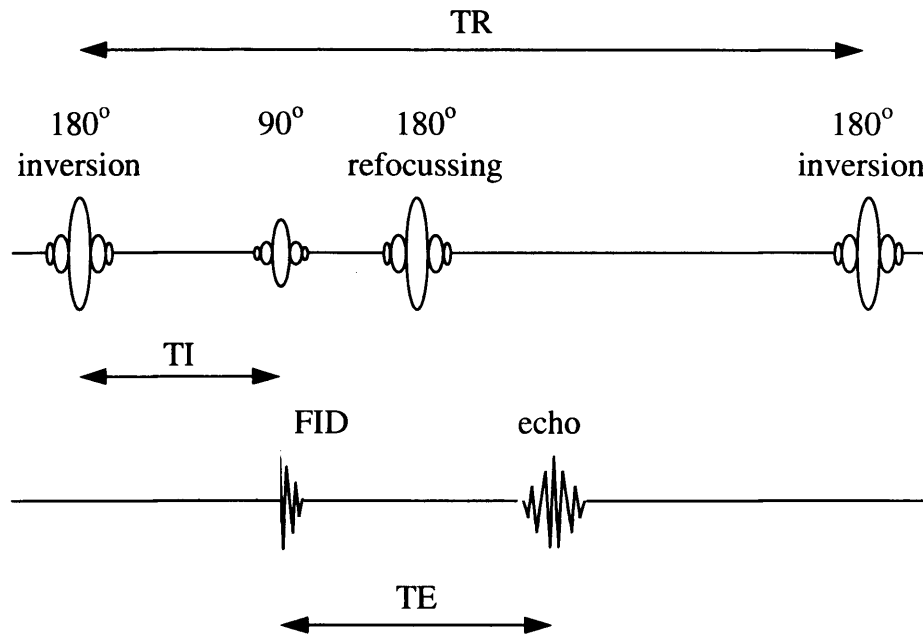


Figure 2.11 diagrammatically illustrates the inversion recovery pulse sequence.

When inversion recovery imaging is combined with gradient echo pulse sequences e.g. snapshotFLASH, subsecond image acquisition is can be achieved. This employs a  $180^\circ$  inversion pulse, a time  $TI$ , followed by a short  $TR$  (2-10 ms) gradient echo sequence which is rapidly repeated to acquire an image.

## 2.5 Magnetic resonance image formation.

All the protons have frequencies that are all identical, that is at the Larmor frequency. However in order to image the body, the frequencies need to become slightly different, so that spins can be distinguished. MR imaging uses the Larmor relationship to achieve this. In the uniform  $B_0$  field, all nuclei precess at the same frequency, the application of a position dependent magnetic field perturbation called a gradient has the effect of tuning the resonant frequencies according to their spatial location along the gradient.

The gradient is a weak magnetic field that is produced by additional coils placed in the bore of the magnet, and adds to the main magnetic field Eq.[2.7]. The gradient ( $G$ ), produces a change in the magnetic field  $\Delta B_0$ , dependent upon its precise spatial location ( $x$ ) along the gradient.

$$\Delta B_0 = G x \quad [2.7]$$

The superimposition of the gradient on the main magnetic field, affects the resonance frequencies of the protons along the gradient as predicted by Eq.[2.8],

$$\omega_0 = \gamma B_0 + \gamma Gx \quad [2.8]$$

For two dimensional imaging, a selective RF pulse is applied, and at the same time a gradient is also applied. This excites the spins in a single slice. A second gradient encodes the location along one dimension in the frequency of the MR signal. At the same time, a third gradient encodes the location in the phase of the MR signal.

### 2.5.1 Slice selection.

If an RF pulse of a specific frequency is applied when the slice select gradient is activated, only nuclei corresponding to that frequency will resonate. The location of the excited protons is dependent upon the frequency of the slice selecting pulse, and can be shifted by increasing or decreasing the frequency of the RF pulse.

An RF pulse is made up of a spread of frequencies. This spread is called the bandwidth. The RF pulse will excite spins whose Larmor frequencies fall within the bandwidth of the RF pulse. The thickness of the slice of tissue affected is dependent upon two factors:

- i) the strength of the slice select gradient,
- ii) the bandwidth of the RF pulse.

If the strength of the slice select gradient is increased, there will be an increase in the range of frequencies across the distance. If then an RF pulse of a fixed bandwidth is used, there will be fewer spins excited, and the slice thickness is reduced. If however a weak slice select gradient is applied, the same RF pulse would produce a thick slice.

### 2.5.2 Frequency encoding.

This is performed at detection of the signal in contrast to slice selection which is performed at excitation. During detection, the spatial position of the spins along the x axis is encoded into the frequency of the signal by applying the frequency gradient. This has the effect of tuning the Larmor frequencies of the nuclei, and therefore the signals they produce vary according to their spatial position. This type of encoding is referred to as frequency

encoding, but as the protons' signal is read by the scanner this gradient is also called the readout gradient. This is illustrated in the figure below.

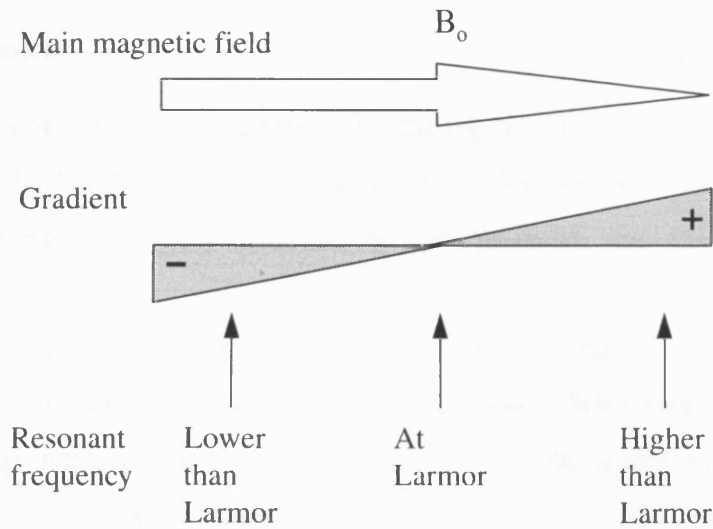


Figure 2.12, shows how the resonant frequency is varied by the superimposition of a gradient field on the existing main magnetic field ( $B_0$ ).

### 2.5.3 Fourier transform.

This is the complex mathematical method employed to decode the MR signal into the individual frequencies that are simultaneously present in signal. The Fourier transform (FT), determines the density of the spins along the  $x$  axis, and so is applied to each frequency encoding line, isolating the number of spins at that frequency.

### 2.4.4 Phase encoding.

The final dimension that requires encoding is achieved by phase encoding with the use of another gradient in the final perpendicular direction, after the slice selection, but before the frequency encoding.

Phase encoding imposes a linear relationship between precessional frequency and position, as was achieved for frequency encoding. Here the phase shift acquired by protons at the end of the phase encoding pulse is used, Eq.[2.9].

$$\theta = \gamma GyT \quad [2.9]$$

The phase shift  $\theta$ , is dependent upon the magnitude of the phase encoding gradient,  $G$ , and its position along the phase encoding axis,  $y$ , and the duration of the gradient  $T$ .

Phase encoding requires multiple read outs, which is why MR imaging takes so long, as each phase encoding step usually requires a separate excitation.

### 2.5.5 Scan times.

If one slice was acquired at a time MR imaging would take a long time and clinical imaging may not be feasible. Fortunately, as there is a lot of dead time between one read out and the next excitation, this time can be used to excite and read out signal from additional slices.

Scan times are also dependent upon the number of data averages that are used. Multiple data acquisitions improve the signal to noise (S/N) ratio. The number of acquisitions ( $N_{aq}$ ) improves the S/N ratio (improves with the square root of the  $N_{aq}$ ) by reducing the background noise caused from periodic motion. This has the penalty of increasing the scan time Eq.[2.10];

$$\text{Scan Time} = TR \times N_y \times N_{aq} \quad [2.10]$$

where  $N_y$  are the number of phase encoding steps. However this is slightly different for fast sequences, such as snapshot FLASH (Haase 1990) where the TR is very short, and the entire image can be acquired in a single shot. The TR factor is entirely eliminated for echoplanar imaging, which acquires all the phase encoding lines after a single excitation.

## 2.6 References

- Bloembergen N. Proton relaxation times in paramagnetic solutions. *J Chem Phys.* 27:572-753, 1957.
- Chang C. Magnetic resonance imaging contrast agents. Design and physicochemical properties of Gadodiamide. *Invest Radiol.* 28:S21-S27, 1993.
- Donahue K, Burstein D, Manning W, Gray M. Studies of Gd-DTPA relaxivity and proton exchange rates in tissue. *Magn Reson Med.* 32:66-76, 1994.
- Haase A. Snapshot FLASH MRI. Applications to  $T_1$ ,  $T_2$  and chemical shift imaging. *Magn Reson Med.* 13:77-89, 1990
- Mann J. Stability of gadolinium complexes in vitro and in vivo. *J Comput Assit Tomogr.* 17 (suppl 1):S19-S23, 1993.
- McLaughlin A, Leigh J. Relaxation times in systems with chemical exchange: approximate solutions for the nondilute case. *J Magn Reson.* 9:296-304, 1973.
- Solomon I. Relaxation processes in a system of two spin states. *Phys Rev.* 99:559-565, 1955.
- Tan Hu JI, Sepponen RE, Lipton MJ, Kuusela T. Synergistic enhancement of MRI with Gd-DTPA and magnetisation transfer. *J Comput Assit Tomogr.* 16:19-24, 1992.
- Wolff SD, Balaban RS. Magnetisation transfer contrast (MTC) and tissue water proton relaxation *in vivo*. *Magn Reson Med.* 10:135-144, 1989.
- Young I, Clarke G, Bailes D. Enhancement of relaxation rate with paramagnetic contrast agents in NMR imaging. *J Comput Assit Tomogr.* 5:543-547, 1981.

## **Chapter 3: Dynamic $T_1$ measurement using snapshot FLASH.**

### **3.1 Introduction**

Relaxation times are rate constants that describe the speed with which the magnetisation changes. The  $T_1$  or longitudinal relaxation time describes how rapidly spins realign with the main external magnetic field following R.F. stimulation.  $T_2$  or transverse relaxation describes the time taken for the spins to lose phase coherence following perturbation by an R.F. pulse.

#### **3.1.1 General factors affecting the accuracy and precision of $T_1$ relaxation measurements.**

The accuracy of  $T_1$  measurement describes the proximity of the measured  $T_1$  to the 'true'  $T_1$ , and so describes systematic errors. The precision describes the reproducibility of the  $T_1$  measurements.

Factors which may affect the accuracy of  $T_1$  measurements on a clinical MR imaging scanner are: multiexponential signal decay, adequate mathematical model to fit the  $T_1$  signal decay and the correct set up of imaging sequences.

Most tissues exhibit multiexponential  $T_1$  and  $T_2$  decay as they are composed of compartments which have different relaxation times (Bakker *et al* 1984). When imaging protocols are applied to patients, they are limited by their ability to detect multiexponential decay which is dependant upon being able to image the decay of the different compartments. This requires lots of high quality images to be acquired with different degrees of relaxation. The multiexponential signal decay then has to be fitted mathematically to obtain  $T_1$  relaxation values. This can be difficult if there is poor temporal resolution between the various compartments, due to the decay of the short component before the signal is collected. The subsequent signal may then be closer to a single

exponential than a multiexponential. This is dependant upon how much the various components differ (Mather-De Vre 1984).

Mathematical models used in the calculation of  $T_1$  may lead to inaccuracies due to assumptions that may be made in the model. The behavior of the signal to a pulse sequence is predicted, and there may be assumptions made of the effective flip angle for slice selective pulse sequences, and may not hold true (Redpath 1982). Within human studies there may be R.F. attenuation in deep tissues which may have the effect of reducing the flip angle (Bottomley *et al* 1978, 1984). This has the effect of introducing inaccuracies in the measurement of  $T_1$ .

Another problem is that of slice profiles when using a multislice technique. The influence of excitation of magnetisation in adjacent slices can produce significant errors in the accuracy of  $T_1$  measurements (Just *et al* 1988).

The scanning protocols in most clinical scanners are preset by the manufacturer, and it is assumed that the different imaging sequences are properly calibrated, e.g. correct rephasing of magnetisation. One consequence of slice selective excitation is that the spins in an excited slice will accumulate a different phase depending upon their position in the main magnetic field. This results in an incoherent  $x$ - $y$  magnetisation, which can be overcome by reversing the slice select gradient (Sutherland *et al* 1977). Consequently, if sequences are not properly calibrated, relaxation times may vary depending upon the sequence used for measurement.

Precision of  $T_1$  measurement, describes the variability of relaxation time measurements. Factors which affect precision fall into three main categories: imager imperfections, partial volume effects and variations in  $T_1$  reflecting the changes in the actual  $T_1$  of the tissue.

Imager imperfections which can cause imprecision include image noise which is always present, and will affect the relaxation time measurements. Also the temporal stability of the phantoms or subject affects precision. An example would be temperature fluctuations which will reflect in changes in the measured relaxation time, and so measurements will be imprecise.

The uniformity of tissue can be a source of imprecision due to partial volume effects. If measurements are taken for follow-up studies, repositioning will also then play a part in the precision of the measurements.



Finally there may be variation in the samples themselves. Within subjects this may be differences in the same tissue but different locations, or due to physiological variation, or due to pathology e.g. alcohol intoxication (Mander *et al* 1985).

### 3.1.2 Methods of $T_1$ measurement using MRI.

The different methods of measuring  $T_1$  fall into three major categories: multishot, single shot and dynamic imaging.

#### 3.1.2.1 Multishot techniques.

These require more than one imaging experiment to measure the  $T_1$ .

##### 3.1.2.1.I Progressive Saturation and Saturation Recovery.

In progressive saturation, shown in Figure 3.1 below.

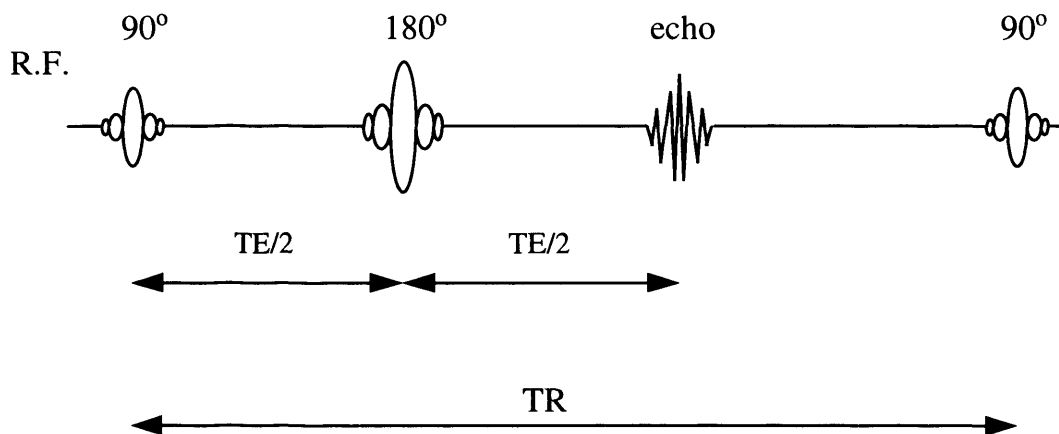


Figure 3.1. Shows a spin echo pulse sequence for partial or progressive saturation. TR is the repetition time, and is the time from the application of one R.F. pulse to perturb the longitudinal magnetisation to the next R.F. pulse. TE is the echo time, and is the time from the application of an R.F. pulse to the peak of the signal induced in the R.F. coil receiving the signal. To calculate  $T_1$  using this method, the imaging sequence should be repeated with different values of TR with TE kept constant.

There is an initial slice selective 90° pulse which perturbs all the magnetisation into the transverse plane, which precesses during the time TE and relaxes exponentially with the time constant  $T_2$ . A 180° pulse is then applied which refocuses the transverse magnetisation including any dephasing of the magnetisation due to magnetic field inhomogeneities. The echo as a result is then read. During the time TR, the longitudinal magnetisation recovers

with a time constant  $T_1$ . If there is a short time period ( $<5 \times T_1$ ) before the next  $90^\circ$  pulse then only a fraction of the longitudinal magnetisation will have recovered, and the transverse magnetisation as well as the acquired signal will be a function of the  $T_1$  and TR. If this is repeated, eventually a steady state is reached. If several images are obtained with different values of TR, then the  $T_1$  value can be calculated by a non-linear fit of the longitudinal recovery curve.

Saturation recovery involves an initial pulse which saturates the system, i.e. there is zero net magnetisation. After a delay time (T), a  $90^\circ$  pulse is applied which samples the amount of relaxed magnetisation. The time delay T is used instead of TR, and can be made as short as instrumentation permits, enabling accurate measurements of very short  $T_1$ s.

This latter method however can not be easily applied to clinical imaging due to the initial burst of R.F. energy used to saturate the magnetisation, which dissipates a large amount of energy into the patient. Also there is the problem of longer imaging times due to the time delay T. The basic sequence can be altered by using an initial  $90^\circ$  pulse to tip the spins into the transverse plane, followed by a "spoiler" gradient to dephase the transverse magnetisation (Hickey *et al* 1986).

### 3.1.2.1.II Inversion recovery.

This method uses an initial slice selective  $180^\circ$  pulse to invert the magnetisation. It then relaxes with the time constant  $T_1$ , for a time period TI. A  $90^\circ$  pulse is then applied which reads the relaxed magnetisation. The final signal is proportional to the relaxation of magnetisation during the inversion time TI. This is shown in Figure 3.2 below.

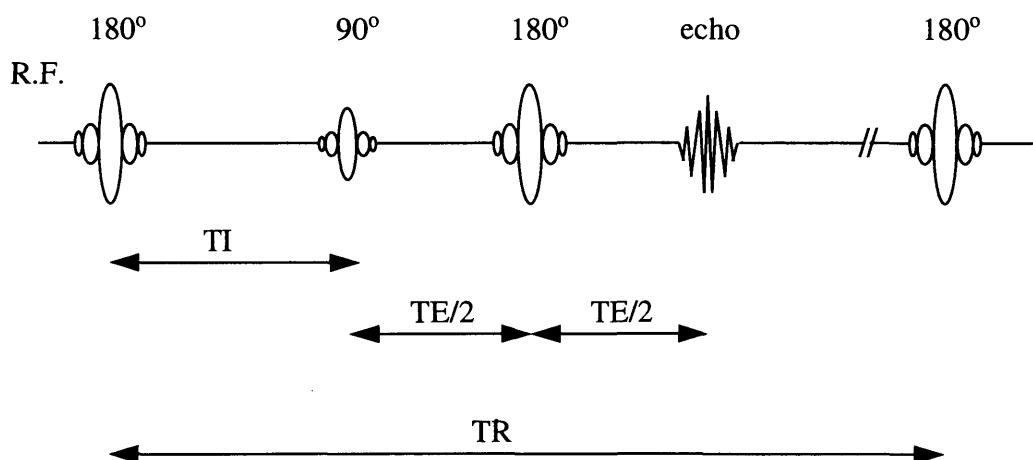


Figure 3.2. Shows an inversion recovery spin echo pulse sequence. TI is the inversion time, TR is the repetition time and TE is the echo time. To calculate  $T_1$  the imaging sequence has to be repeated with different values of TI, with TE kept constant.

The sequence TR i.e. time between  $180^\circ$  pulses, must be long enough to allow the perturbed magnetisation to fully relax therefore must be  $\geq 5 \times$  longest  $T_1$ . However this would make the sequence clinically impractical as imaging times would be too long. The sequence is adapted, so there is a short TR, and the partial recovery of the magnetisation after the  $90^\circ$  pulse and next  $180^\circ$  inversion pulse is accounted for. If several images are acquired with different TIs then the  $T_1$  can be calculated by a non-linear fit of the longitudinal recovery.

This sequence has a wide dynamic signal range which extends from  $-1$  to  $+1$  ( $\times M_0$ ). However on commercial scanners the image is generally reconstructed and displayed as a magnitude image. This introduces problems when calculating the  $T_1$ , because if the phase inversion is left uncorrected, it becomes impossible to distinguish the negative signal from a long  $T_1$  and the positive signal from a much shorter  $T_1$ . This is known as contrast reversal (Young *et al* 1985), and several methods have been proposed to correct for the polarity of the signal (Bakker *et al* 1984, Park *et al* 1986, Borrello 1990, Gowland *et al* 1991).

### 3.1.2.1.III Two point measures.

This allows longitudinal magnetisation to be derived from the intensity ratio from two images. These are for;

- i) inversion recovery (IR), two images with different TIs.
- ii) progressive saturation (PR), two images with different TR's
- ii) saturation recovery (SR), two images with different T's.

The theoretical ratio of these signal intensities is used in a look-up table to determine the  $T_1$ . The accuracy of the  $T_1$  is dependent upon the pulse intervals chosen. In the PS or IR sequence, if the measures are made too early or too late in the longitudinal recovery, the intensity ratio will be insensitive to the  $T_1$ . At these extremes noise introduces large errors in the derived relaxation times. A large ratio of the two parameters (TR for PS or TI for IR) allows a wider range of relaxation times to be determined, but is time consuming. For PS, a ratio of four between the two TR's is considered to be a good compromise (Freeman *et al* 1972, Lin *et al* 1986). IR requires that one of the images is obtained near the null condition (Freeman *et al* 1972).

#### 3.1.2.1.IV Hybrid schemes.

One of these involves a partial saturation and inversion recovery experiment (Edelstein *et al* 1980) which can be separate experiments or can be interleaved into the same sequence. It again employs a look-up table for the signal intensity of the ratios of IR/PS.

#### 3.1.2.1.V. Variable Tip-angles.

Here a pulse angle of  $\theta^\circ$  is used to perturb a fraction of the z-magnetisation into the transverse plane. This magnetisation is a function of the pulse tip angle  $\theta^\circ$ , and of the amount of longitudinal relaxation occurring in the time interval TR (Gupta 1977). Gradients are used to form an echo to enable an image to be derived. A spoil gradient pulse is applied after the echo to ensure that all the transverse magnetisation has been dephased before the next sequence repetition. The pulse sequence is shown in Figure 3.3. To calculate the  $T_1$  a minimum of two repetitions of the imaging sequence are required at different excitation pulse angles  $\theta^\circ$  (Frahm *et al* 1987).

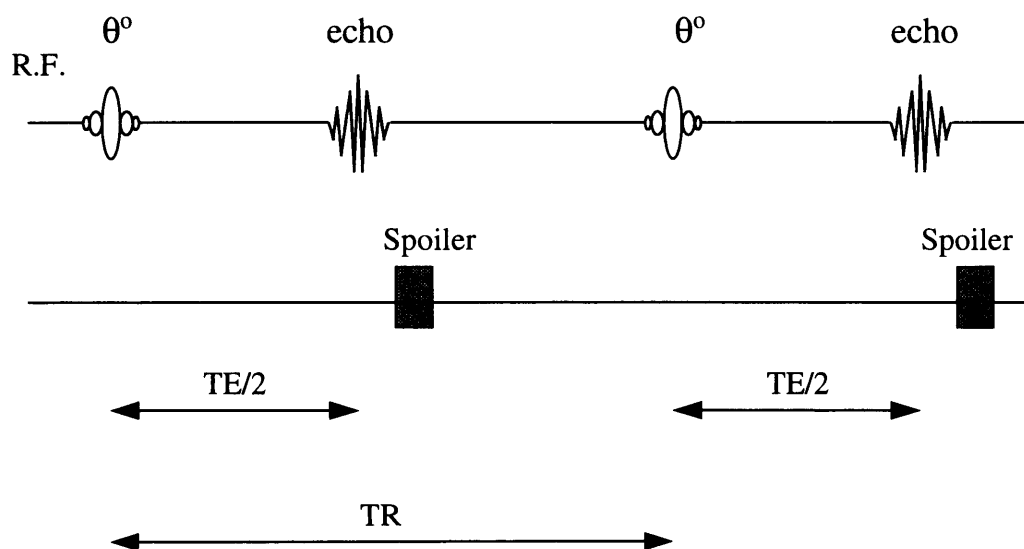


Figure 3.3. Shows a variable tip angle gradient echo sequence. This sequence employs a spoiler gradient to ensure that all the transverse magnetisation is completely dephased before the sequence is repeated. To calculate  $T_1$  using this sequence, images are collected with the excitation pulse at different tip angles, with the TE kept constant.

In the calculation of  $T_1$ , it is assumed that pulses are applied along the same axis and that the magnetisation has reached steady state, which generally occurs after the first few repetitions (Homer *et al* 1985). The transverse relaxation is described by  $T_2^*$  which is the effective transverse relaxation during the time period TE. Also assumed is that  $TR \gg T_2^*$  to ensure that the transverse relaxation is completely dephased prior to the next repetition. Several images are acquired at different values of excitation pulse flip angle, with all other parameters constant.  $T_1$  can be calculated as a straight line fit when the signal intensity  $S(\theta)/\sin\theta$  is plotted against  $S(\theta)/\tan\theta$ .

Parameter optimisation studies have shown that this method using two different pulse flip angles, is more precise than a multiple point measurement with the same overall repetition time (Wang *et al* 1987). Also pulse flip angles should be well separated and short repetition times are required ( $TR < T_1$ ). The limitation of this sequence is that in the presence of an inhomogeneous magnetic field, the final signal intensity may be poor, as a  $180^\circ$  pulse cannot be employed in the echo formation. There is also the problem of pulse tip angle variation when this changes across a slice.

### **3.1.2.2 Single shot techniques**

These techniques acquire the images required for  $T_1$  calculation in one imaging experiment. They have a time advantage over other imaging methods, as they require no more than one imaging sequence repetition for calculation of  $T_1$ .

#### **3.1.2.2.I Stimulated echo**

Here the magnetisation is tipped into the transverse plane by the first  $90^\circ$  pulse. This then dephases during the time interval TE, during which time one line of phase encoding is performed. The second  $90^\circ$  pulse is then applied which causes half the magnetisation to be stored in a plane parallel to the longitudinal axis, while still preserving its phase information. The other half of the magnetisation is rephased by this pulse to form the primary echo after a time TE/2. This echo has half the signal intensity of a spin echo. The final  $90^\circ$  pulse, brings the magnetisation stored along the longitudinal plane, back into the transverse plane. The pulse also has the effect of refocussing the magnetisation to form an echo after a further time TE/2, known as the stimulated echo (Hahn 1950, Frahm *et al* 1985, Sattin *et al* 1985(I)). This sequence is shown in Figure 3.4.

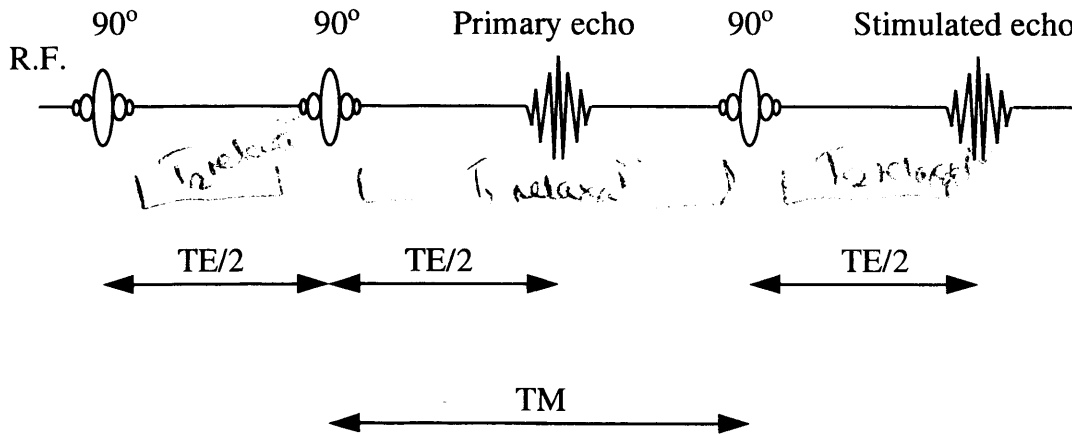


Figure 3.4. Shows the stimulated echo pulse sequence.  $TM$  is the time interval between the second and third  $90^\circ$  pulses. The signal intensity of the stimulated echo decreases exponentially with  $T_1$  as  $TM$  is increased. The calculation of  $T_1$  using this sequence requires only one imaging experiment with the acquisition of both the primary and stimulated echos and a known time interval  $TM$ .

During the time interval between the second and third  $90^\circ$  pulses ( $TM$ ), the stored magnetisation experiences only longitudinal relaxation. If  $TM \geq 5 \times T_1$ , all the spins will have relaxed back to thermal equilibrium. Therefore, there will be no stored magnetisation left to refocus with the third  $90^\circ$  pulse, and no stimulated echo. The signal intensity of the stimulated echo is dependent upon the  $T_2$  relaxation that occurs during the time interval  $TE$ , and the  $T_1$  relaxation that occurs during the time interval  $TM$ . Also the time interval between sequence repetition must be long enough to ensure that all the magnetisation has relaxed back to thermal equilibrium, and therefore avoid partial saturation of the signal. The calculation of the  $T_1$  involves the ratio of the signal obtained for the stimulated echo to that obtained for the primary echo (Sattin *et al* 1985 (II) ).

This method acquires both images within one sequence repetition, so it has the advantage that it reduces the effect of patient motion on the measurement of  $T_1$ . The disadvantage however is that there is poor signal to noise ratio, as there is only half the signal intensity compared to a conventional spin echo, which can lead to errors in  $T_1$  calculation (Edelstein *et al* 1986). To double the signal-to-noise ratio would require four times the image acquisitions.

This technique can be varied to allow multiple points along the relaxation curve to be acquired in one imaging experiment, enabling the study of multiexponential  $T_1$  relaxation. Here the third  $90^\circ$  pulse is divided into a number of smaller read pulse tip angles, which partially sample the stored longitudinal magnetisation, each of which is

separated by a different time interval  $T_M$ . Each of the read pulse tip angles has the effect of reducing the residual stored magnetisation, and therefore the next stimulated echo. It has been shown that ideally the read pulse tip angles should begin at small values and increase to  $90^\circ$  for the final pulse (Haase *et al* 1985, Mareci *et al* 1986). Alternatively, all the read pulse tip angles could be set to very have a very small tip angle (eg  $5^\circ$ ), which would simplify the calculation of  $T_1$  (Haase *et al* 1985). However this has the major disadvantage of reducing the signal to noise ratio of the stimulated echo. The division of the third  $90^\circ$  pulse into multiple read pulses can have the effect of forming unwanted echoes during each acquisition interval. This will produce ghost artefacts, degrading the quality of the image, and affecting  $T_1$  calculation. This effect can be overcome by the use of phase cycling, involving extra signal acquisitions, and the application of gradients to suppress the unwanted echoes (Barker *et al* 1985).

### 3.1.2.2.II Multiple excitation.

This method of single shot imaging uses multiple read out pulses to sample the longitudinal magnetisation as it approaches steady state. This is in contrast to the previous methods, which have considered the magnetisation when it is already in steady state.

This sequence is based on the imaging version of the Look and Locker spectroscopic sequence (Look *et al* 1970) and is schematically represented in Figure 3.5. This involves a series of low tip angle excitation pulses ( $\theta^\circ < 90^\circ$ ) separated by a short time interval  $\tau$ , which tips some of the longitudinal magnetisation into the transverse plane. This magnetisation is phase encoded, and is read as a gradient echo, the resultant signal is proportional to the longitudinal magnetisation before the excitation pulse. A  $180^\circ$  pulse cannot be used to refocus the magnetisation in the transverse plane as this would have the effect of inverting the remaining longitudinal magnetisation. Before each excitation pulse the remaining residual transverse magnetisation is spoiled.

During the time interval  $\tau$ , between the excitation pulses, the magnetisation relaxes with a time constant  $T_1$ . However, there is an overall decay towards a steady state value which allows the calculation of  $T_1$ , as this value is dependent upon the excitation pulse tip angle  $\theta^\circ$ , actual  $T_1$ , and inter pulse time interval  $\tau$ .

The dynamic range can be increased by addition of a  $90^\circ$  pulse or a  $180^\circ$  inversion pulse (Kaptein *et al* 1976, Graumann *et al* 1986,1987, Brix *et al* 1990). The magnetisation

is sampled by the train of excitation pulses as it relaxes from zero or a negative value, exponentially towards a steady state.

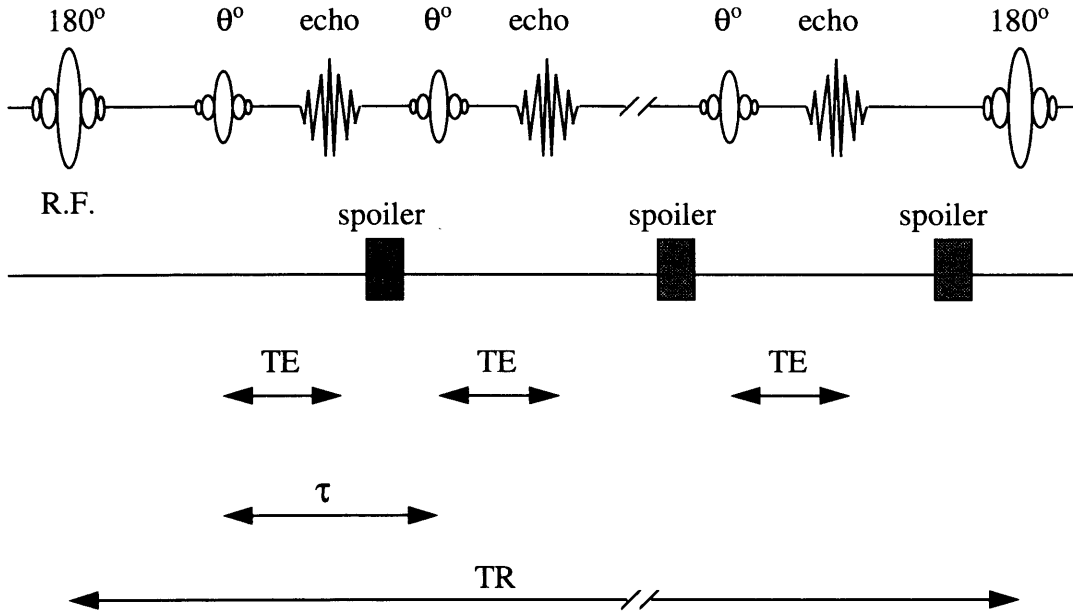


Figure 3.5 Shows a multiple readout gradient echo sequence. The initial preparation pulse of  $180^\circ$  can be replaced by a  $90^\circ$  pulse or even completely omitted. The interval  $\tau$  is the time between the readout pulses and TE is kept constant between these pulses. A spoiler gradient pulse is employed to ensure that all the transverse magnetisation is completely dephased before the next readout pulse is applied. To calculate  $T_1$  all the echos in the readout train are used to generate a series of images with different  $T_1$  weightings but with the same sequence repetition time.

The parameters used in this sequence have been investigated and optimised (Kay *et al* 1991, Zhang *et al* 1992, Gowland *et al* 1992). Low flip angles of the excitation pulses enable maximum dynamic range of the magnetisation and minimise the error in the calculated  $T_1$ . However, larger tip angles are required to increase the signal-to-noise ratio; a good compromise of  $15^\circ$ - $30^\circ$  has been suggested (Zhang *et al* 1992). The interpulse time interval has been optimised to range between 70-100ms for accurate  $T_1$  values ranging between 150-900ms (Zhang *et al* 1992). Accurate measurements for a range of  $T_1$  values can be obtained when the interpulse delay samples points spread over the expected relaxation curve (Kay *et al* 1991).



### **3.1.2.3 Dynamic imaging**

If  $T_1$  is changing rapidly, as is the case in imaging during the dynamic injection of a contrast agent, then methods of  $T_1$  measurement that require multiple images may not be practical. Measurement of  $T_1$  can be achieved in the shortest time by repeatedly acquiring just a single  $T_1$  weighted image, which in conjunction with a static measure of the equilibrium magnetisation, can be used to calculate  $T_1$ . In this context, the inversion recovery snapshot FLASH sequence (Haase 1990) for measuring  $T_1$  assuming monoexponential relaxation (Bluml *et al* 1993) has been studied in this chapter.

Here, an inversion pulse is applied, and after a short time interval TI, series of low flip angle excitation pulses is applied ( $\theta^\circ \ll 90^\circ$ ) separated by a short time interval t, which tips some of the longitudinal magnetisation into the transverse plane. This magnetisation is phase encoded, and is read as a gradient echo, giving a single image in one shot. The contrast in the image is determined by the position of the central phase encoding step in the longitudinal relaxation curve, and can be altered by changing the TI.

## **3.2 Aims**

### **3.2.1 Signal loss due to reduction in overall sequence repetition time.**

The study presented in this chapter investigates the effect on the measured signal intensity in a snapshot FLASH sequence supplied with a standard clinical MRI scanner, when the overall sequence repetition time is reduced. This is the case when first pass dynamic  $T_1$  measurements are required.

### **3.2.2 Effect of the read pulse flip angle on signal intensity.**

Also investigated was the effect the flip angle of the read out ( $\alpha$ ) pulses on signal intensity and the subsequent error introduced into  $T_1$  measurements by this.

### **3.2.3. Correction for specified inaccuracies.**

A correction for these sources of error are attempted, and the accuracy of the correction is investigated.

### 3.2.4 Ability to predict the TI to null during dynamic snapshot FLASH.

This study also investigated a method to calculate the inversion time required to null the signal from the desired tissue when this tissue is partially saturated, as is the case during dynamic investigation using the snapshot FLASH sequence.

## 3.3 Theory.

### 3.3.1 The snapshot FLASH sequence.

In this chapter the effect on the measured signal intensity in a snapshot FLASH sequence when the overall sequence repetition time ( $TR_o$ ) cannot be considered long with respect to  $T_1$  is presented. Normally, the start of the sequence in dynamic cardiac studies is triggered from the ECG, and therefore  $TR_o$  will be an integer multiple of the R-wave interval. For simplicity, a single slice experiment is analysed.

The  $T_1$ -weighted snapshot FLASH sequence (illustrated schematically in Fig. 3.6) can be written:

$$\left[ TD - 180^\circ - TI - [\alpha - TR]_{Nk} \right]_{Ni}, \quad [3.1]$$

where TD is an optional delay before the start of the sequence; TI is the inversion time; and  $\alpha$  is the flip angle of the read pulse for acquisition of one line of  $k$ -space. The inner loop is repeated for  $Nk$  lines of  $k$ -space, and the outer loop is repeated  $Ni$  times, according to the number of images required. When more than one image is acquired, the signal intensity is affected by the pulses from the previous image, and analysis becomes more complicated. Also, the  $\alpha$  pulses cause increasing saturation through the sequence and therefore, for simplicity, it is assumed that the signal intensity seen in the final image reflects the intensity of the mid-line of  $k$ -space, from which most of the image contrast is derived. Rostrup *et al.* (1995) showed the effect of the  $\alpha$  pulses on measured signal intensity. Their results are extended in this study to show the correction needed when the overall sequence repetition does not allow complete relaxation.

Using the notation in Figure 3.6, expressions for the  $z$ -magnetisation at four stages in the snapshot FLASH sequence have been written by Dr M.A. Horsfield. These are shown in the Appendix 1, together with the theoretical solutions for signal intensity saturation correction, and prediction of inversion time to null tissue ( $TI_{null}$ ).

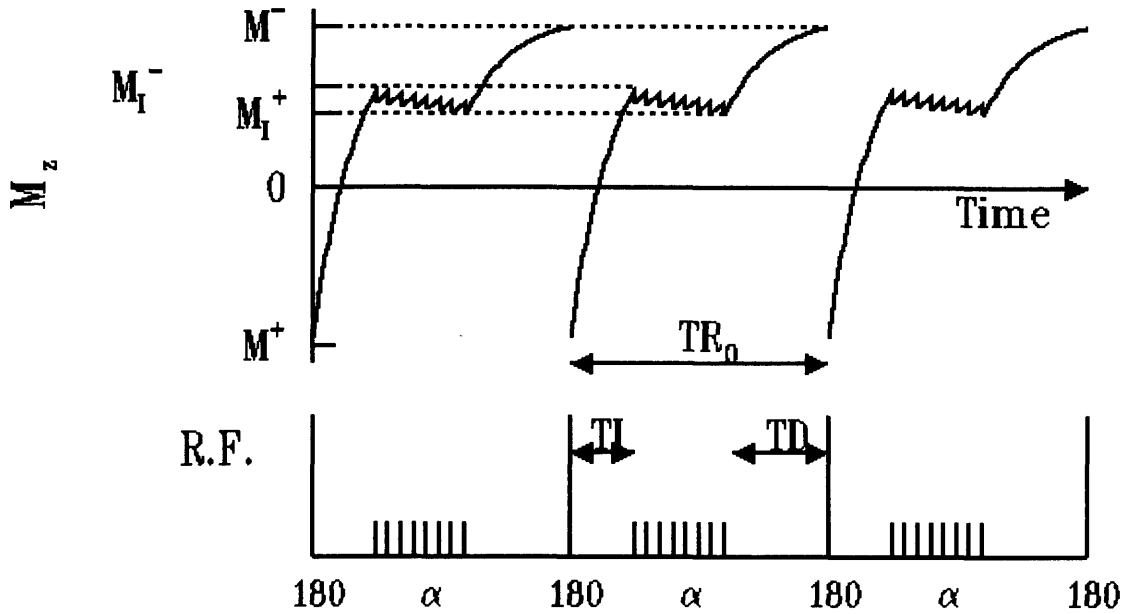


Figure 3.6. Schematic representation of the z-magnetization during the snapshot FLASH sequence in the steady-state.  $TR_0$  is the image repetition time; TI is the inversion time and TD is the post-image recovery/trigger delay. The longitudinal magnetization values are shown just before the inversion pulse ( $M^-$ ); just after the inversion pulse ( $M^+$ ); just before the start of image acquisition ( $M_I^-$ ); and at the end of image acquisition ( $M_I^+$ ).

### 3.3.2 The theoretical effects of the overall sequence repetition time.

The predicted theoretical signal intensity response to variations in the overall sequence repetition time are plotted in Fig. 3.7, below. This is shown for typical values of  $T_1$  and  $TR_0$ .  $T_{1pre}$  is 750 ms, typical of myocardium. The  $TR_0$  varies between 0.5 and 5 times  $T_{1pre}$  (between 0.375 s and >3.75 s). The effective inversion time to achieve nulling pre-contrast then varies accordingly between 165 and 519 ms. As can be seen, considerable differences in the shape of signal intensity response occur as  $TR_0$  is shortened, and it would only be possible to evaluate  $T_1$  by taking into account both the inversion time and the overall sequence repetition time. As  $TR_0$  is shortened, the response becomes flatter around the null-point, with steeper response at lower  $T_1$  values.

A comparison between using a simple equation Eq. [A1.7] and a more complex equation Eq. [A1.9] to estimate  $R_1$  ( $= 1/T_1$ ) is shown in Fig. 3.8. These equations estimate the  $R_1$  in the event of low flip angle read pulse flip angles; the simple equation when  $TR_0$  is short, whereas the complex equation when  $TR_0$  is long w.r.t.  $T_1$ . The use of the simple

equation is shown to give considerable deviation from the actual  $R_1$  value towards the smaller  $R_1$  values (around the null-point). At large  $R_1$  values, the short sequence repetition time has little effect on the rapidly relaxing spins and the accuracy of the measurement is not affected.

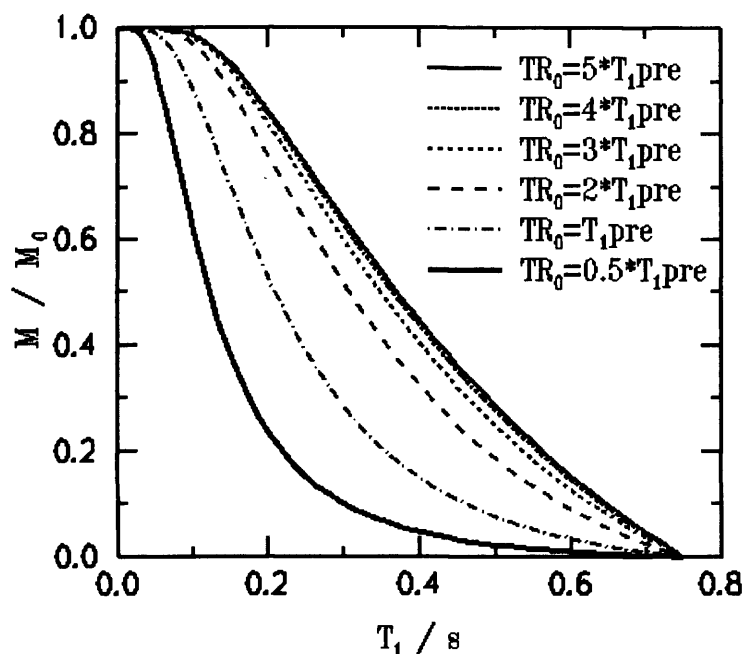


Figure 3.7 Signal intensity as a function of  $T_1$  for various overall repetition times. The values are normalised to an image without the inversion pulse and with a long repetition time.

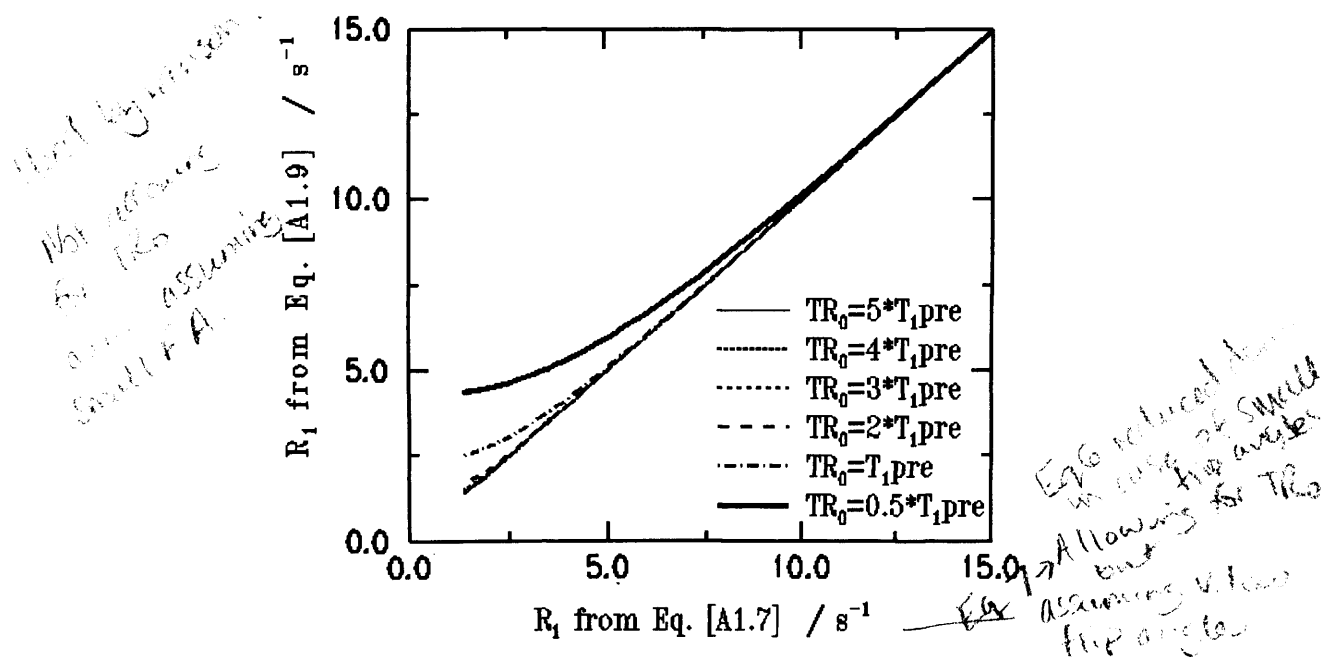


Figure 3.8. Simulated errors in  $R_1$  measurement caused by using the simple equation (Eq. [A1.9]) as the overall TR is reduced.

### 3.3.3 Theoretical effects of the read pulse flip angle.

The effect of increasing the flip angle of the  $\alpha$  pulses on the image signal intensity ratio ( $M(t)/M_0$ ) across the range of  $T_1$  values is shown in Figure 3.9, using the full analysis Eq. [A1.6].  $M(t)$  is the z-magnetisation value at time (t), and  $M_0$  is the signal intensity which would be observed with a very long inversion time. For clinical imaging, low flip angle  $\alpha$  pulses may not be practical where the signal-to-noise ratio must also be considered. The behaviour of the full analysis Eq. [A1.6] for increasing flip angles and the following sequence parameters: 64 lines of k-space with the mid-line being line 32;  $TR=4.7$  ms;  $T_{1pre}=750$  ms;  $TR_0 = T_{1pre}$  are examined. The approximation of low flip angle  $\alpha$  pulses will clearly lead to errors in  $T_1$  estimation for even quite modest flip angles. The full equation, Eq. [A1.6], should be used when flip angles exceed a few degrees.

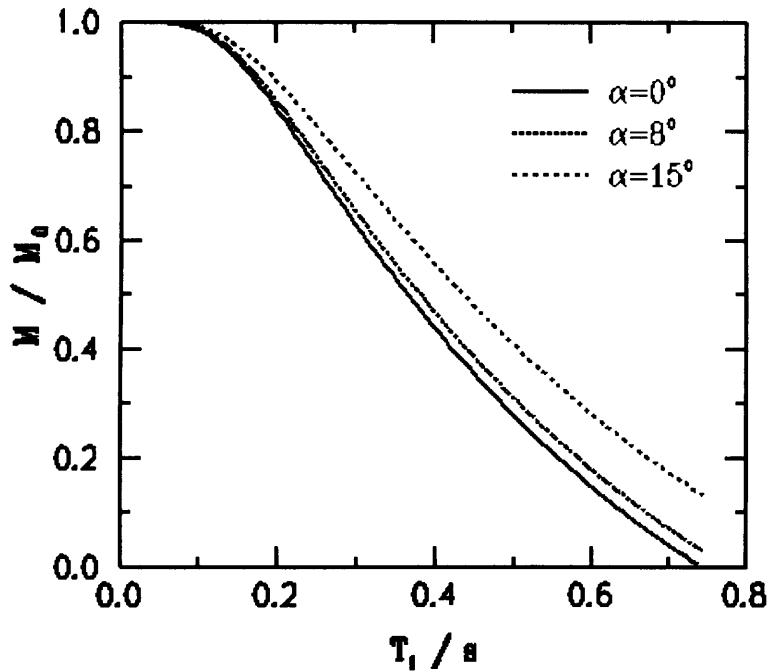


Figure 3.9. The simulated effect of increasing flip angle on the image signal intensity ratio, for a range of  $T_1$  values at  $TR_0 > 5 \times T_{1pre}$ .

However, the use of the full equation Eq. [A1.6], leads to the further complication in that the signal intensity measured even with full relaxation before the image acquisition now depends not only on the proton density, but also on the  $T_1$  of the tissue. Thus the  $M_0$  value in the full equation Eq. [A1.6] cannot strictly be found from a single scan without an inversion pulse. Figure 3.10 shows the variation in signal amplitude (normalised to the

value for very short  $T_1$ ) that would be seen in the " $M_0$ " image, for increasing flip angles, and across the range of  $T_1$  values, again for the example sequence parameters above. For flip angles up to about  $8^\circ$ , the change in signal amplitude in the  $M_0$  image is relatively small at the higher  $T_1$  values. Therefore, if the tissue  $T_1$  is known to be towards the higher end of the range of values to be measured at the time when the  $M_0$  image is acquired, a correction factor can be computed for the  $M_0$  value in subsequent dynamic measurement using the full equation Eq. [A1.6].

In order to choose the best flip angle, the measured signal amplitude over the range of  $T_1$  values must be assessed. Figure 3.11 shows the measured signal amplitude over a range of flip angles for the same sequence parameters as above. Clearly, for the lowest  $T_1$  values, the signal amplitude continues to increase as the flip angles increases up to  $90^\circ$ . However, over the whole range of  $T_1$  values, flip angles above  $12^\circ$  do not increase the signal amplitude greatly in this example. Although not taken into account in Figure 3.11, the inversion time needs to be reduced still further if the same  $T_1$  is to be nulled.

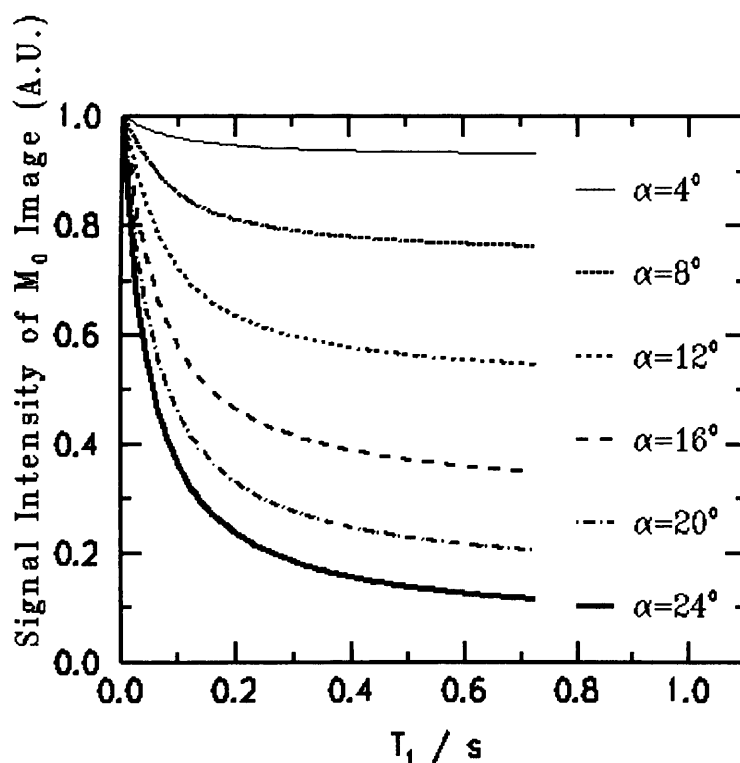


Figure 3.10. The simulated effect of flip angle increase on the signal intensity of an " $M_0$ " image for a range of  $T_1$  values.

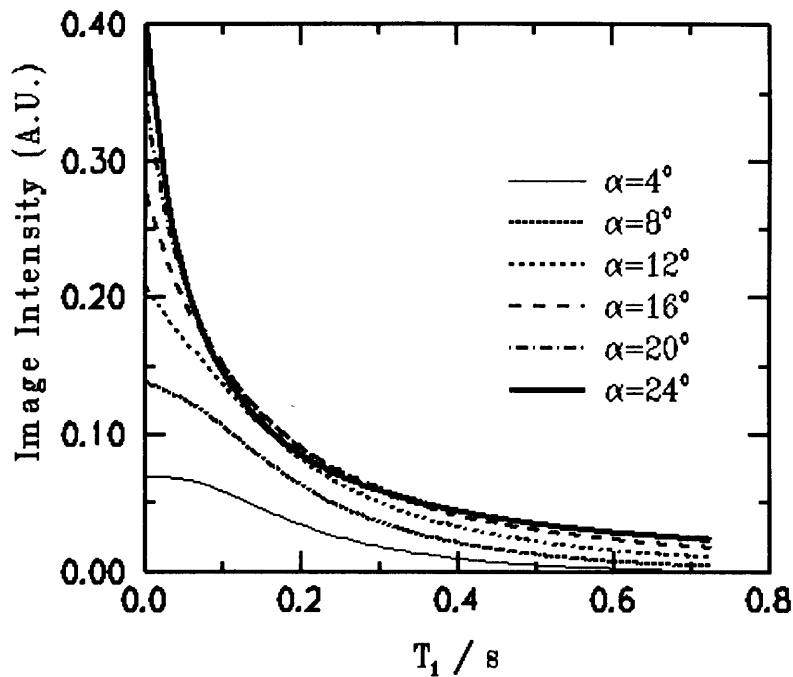


Figure 3.11. The simulated effect of flip angle increase on signal amplitude for a range of  $T_1$  values. For  $T_1$  values above 0.1 s, no improvement in image intensity is seen if the flip angle is increased above  $12^\circ$ , for the set of sequence parameters described in the text.

### 3.4 Methods.

All experiments were performed using a whole body MRI system (MAGNETOM, Siemens, Erlangen, Germany) operating at 1.0 Tesla. A linearly polarised body coil was used for R.F. transmission and reception of the NMR signal. The system was equipped with actively shielded magnetic field gradient coils, giving gradient strengths of up to  $15 \text{ mT m}^{-1}$  with rise times of 1ms.

#### 3.4.1 Assessment of effects on $T_1$ measurement of phantoms.

##### 3.4.1.1 Effect of flip angle and 2 vs. 3 parameter fit on $T_1$ measurement using saturation recovery gradient echo imaging.

The effect of an incorrect  $90^\circ$  pulse on the measurement of  $T_1$  using a saturation recovery gradient echo sequence was investigated.

Two phantoms each containing water doped with a different concentration (0.5432 and 0.1086 mmol/L) of Gd-DTPA (Omniscan, Nycomed, Norway). These were predicted to give  $T_1$  values of 0.4s and 1.2s using the equation:

$$\frac{1}{T_1} = \frac{1}{T_{1water}} + [Gd] \times \rho \quad [3.2]$$

Here,  $\rho$  is the relaxivity of Gd-DTPA, the literature value of which is  $4.6 \text{ mM}^{-1} \text{ s}^{-1}$ .

The phantoms were placed in the MRI scanner and imaged using a saturation recovery gradient echo sequence, with TR values decreasing from 5000 to 58 in 12 steps. The field of view (FOV) was 500 mm, 2 slice of 10mm thickness were acquired, with a  $192 \times 256$  data matrix and the echo time (TE) was 10 ms. Two slices had to be acquired to enable a long TR, but only one of the slices was used for  $T_1$  measurement, and there was a large distance between them. The inline adjust was switched off after the first scan, and the transmitter voltage was noted.

The transmitter voltage was altered after the  $90^\circ$  pulse measurements, to give flip angles of  $45^\circ$ ,  $60^\circ$ ,  $75^\circ$ ,  $105^\circ$ ,  $120^\circ$  and  $135^\circ$ . The  $T_1$  relaxation time was estimated for the two phantoms using a non-linear two parameter curve fitting to a plot of signal intensity vs. TR was performed using an equation of the form:

$$M = M_0 (1 - e^{-TR/T_1}) \quad [3.3]$$

A three non linear three parameter curve fitting was then performed to an equation of the form;

$$M = \frac{M_0 (1 - e^{-TR/T_1})}{(1 - \cos(\alpha) e^{-TR/T_1})} \quad [3.4]$$

#### 3.4.1.2 Signal loss due to effects of $T_2$ relaxation.

A phantom consisting of 17 separate vials each containing water doped with a different concentration (0.238 to 40.238 mmol/L) of Gd-DTPA (Omniscan, Nycomed, Norway), was used to give a range of  $T_1$  values from 0.75s to approx. 0.005s using equation [3.2].

A spin-echo sequence with TE values decreasing from 1000 to 10ms, in 13 steps. The field of view (FOV) was 300 mm, 1 slice of 10mm thickness was acquired, with a  $64 \times 128$  data matrix and the repetition time was 3000 ms. Non-linear curve fitting to a plot of signal intensity vs. TE was performed using an equation of the form:

$$M = M_0 \times e^{-TE/T_2} \quad [3.5]$$

This allowed estimation of  $T_2$ , which was found to range between 0.633 and 0.005 seconds.



The relative signal loss due to  $T_2$  effects was then calculated for a TE of 2ms, corresponding to the TE of the snapshot FLASH sequence, using an equation of the form;

$$\frac{M}{M_0} = e^{-(R_2 + \rho \times [Gd]) \times TE} \quad [3.6]$$

### 3.4.2 $T_1$ measurement of phantoms.

A phantom consisting of 7 separate vials each containing water doped with a different concentration (0.238 to 1.608 mmol/L) of Gd-DTPA (Omniscan, Nycomed, Norway), was used.

The  $T_1$  values of these solutions were measured three times using a saturation-recovery gradient-echo sequence. These were conducted over a six month period, at different times on different days. The TR values decreased from a maximum of 4300ms to a minimum of 26ms, in 18-15 steps. The field of view (FOV) was 300 mm, 1 slice of 10mm thickness was acquired, with either a 256 or 192 × 256 data matrix and the echo time (TE) was 10 ms. A two parameter non-linear curve fitting to a plot of signal intensity vs. TR was performed using Eq.[3.3]. This allowed a mean estimation of  $T_1$ , which was found to range between 0.196 and 0.776 seconds.

### 3.4.3 The effect of a reduction in the overall sequence repetition rate and ability to predict null point.

The errors in  $T_1$  values estimated using Appendix 1 Eq. [A1.9] were evaluated for the snapshot FLASH sequence. Also, the accuracy of Eq. [A1.10] in predicting the inversion time to null a particular  $T_1$  was assessed. One of the solutions of Gd-DTPA had a  $T_1$  similar to that of myocardium (0.776s); this vial was used to mimic the behaviour of myocardium before the introduction of contrast agent.  $TR_0$  was varied as a multiple of the myocardial  $T_1$  ( $T_{1pre}=0.776s$ ), from  $0.5 \times T_{1pre}$  through  $1 \times T_{1pre}$ , to greater than  $5 \times T_{1pre}$ , in order to simulate different R-R intervals and multiples of the R-R interval. For each  $TR_0$  the inversion time was adjusted according to Eq. [A1.10] so that the myocardium equivalent solution should have been nulled if Eq. [A1.10] proved to be accurate. The other acquisition parameters for the snapshot FLASH sequence were:  $\alpha = 8^\circ$ ; TR = 4.7 ms; TE = 2 ms; FOV = 300 mm; 64×64 data matrix; 1 slice of 15mm thickness. Eleven consecutive images at each  $TR_0$  were obtained to ensure that the magnetisation reached a

steady state from one image to the next; the signal intensity used in the analysis below was always measured from the final image. In addition, a single image was acquired after full relaxation and without an inversion pre-pulse, the " $M_0$ " scan. The procedure was repeated four times, to ascertain the degree of error in the  $T_1$  measurement.

#### **3.4.4 The effect of altering the read pulse flip angle.**

The effect of changing the flip angle of the  $\alpha$  pulses on the accuracy of  $T_1$  measurement was also investigated. The above procedure was repeated four times at flip angles of  $1^\circ$ ,  $8^\circ$  and  $15^\circ$ , for  $TR_0$  corresponding to the myocardial  $T_1$ , ( $TR_0 = T_{1pre} = 0.75s$ ). Fifteen degrees is the largest flip angle allowed with this sequence on our MRI scanner. The degree of error in  $T_1$  measurement was also assessed at these flip angles.

### **3.5 Results.**

#### **3.5.1 Assessment of effects on $T_1$ measurement of phantoms.**

##### **3.5.1.1 Effect of flip angle and 2 vs. 3 parameter fit on $T_1$ measurement using saturation recovery gradient echo imaging.**

A plot of the flip angle vs.  $T_1$  relaxation time for the two and three parameter non-linear curve fittings is shown in Figure 3.12 below. As can be seen, when the flip angle of the saturation pulse is  $< 90^\circ$ , there is an overestimation of  $T_1$  relaxation times for both phantoms, and using both curve fitting methods. As the flip angle is increased to  $> 90^\circ$ , both methods underestimate the  $T_1$  relaxation time, as expected. However, at a flip angle of  $90^\circ$ , we have found that only the two parameter curve fitting is closest to the  $T_1$  value.

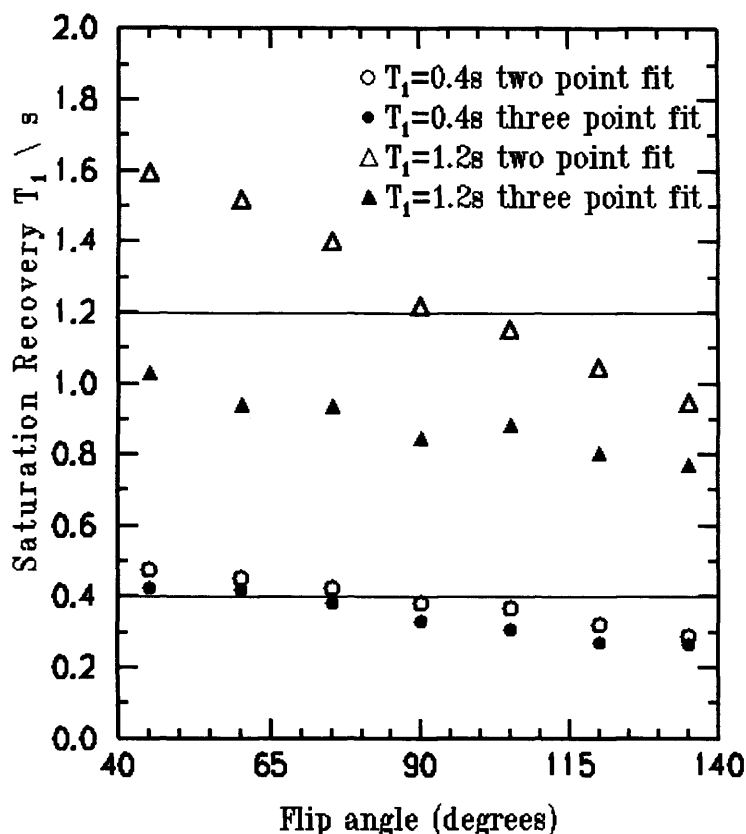


Figure 3.12. Graph to show the effect of a two vs. three parametre nonlinear curve fitting to estimate  $T_1$  relaxation times using a saturation recovery gradient echo method.

### 3.5.1.2 Signal loss due to $T_2$ relaxation.

A plot of Gd-DTPA vs.  $R_2$  is shown in Figure 3.13, together with a regression fitting. The slope of this gives the transverse relaxivity, the literature value of which is  $5.1 \text{ mM}^{-1}\text{s}^{-1}$  at 10mHz 37°C, and we estimated to be  $4.78 \text{ mM}^{-1}\text{s}^{-1}$  (standard error, SE=0.05) at 42mHz and room temperature. The intercept of the curve gives the  $R_2$  of the solvent, which is water in this case. The literature value for this is approx.  $0.3\text{s}^{-1}$ , we found  $-0.25\text{s}^{-1}$  SE=0.59.

This data was then used to estimate the relative signal loss due to  $T_2$  effects over a range of gadolinium concentrations, at the TE used for the snapshot FLASH sequence (TE= 2ms). The results of this are shown in Figure 3.14. At high gadolinium concentrations there is a substantial amount of signal loss due to  $T_2$  effects even at the short echo time of 2ms. At the lower gadolinium concentrations, corresponding to the snapshot FLASH  $T_1$  measurement range, there is still quite a large amount of signal loss, which may have a effect upon the accuracy of  $T_1$  measurement.

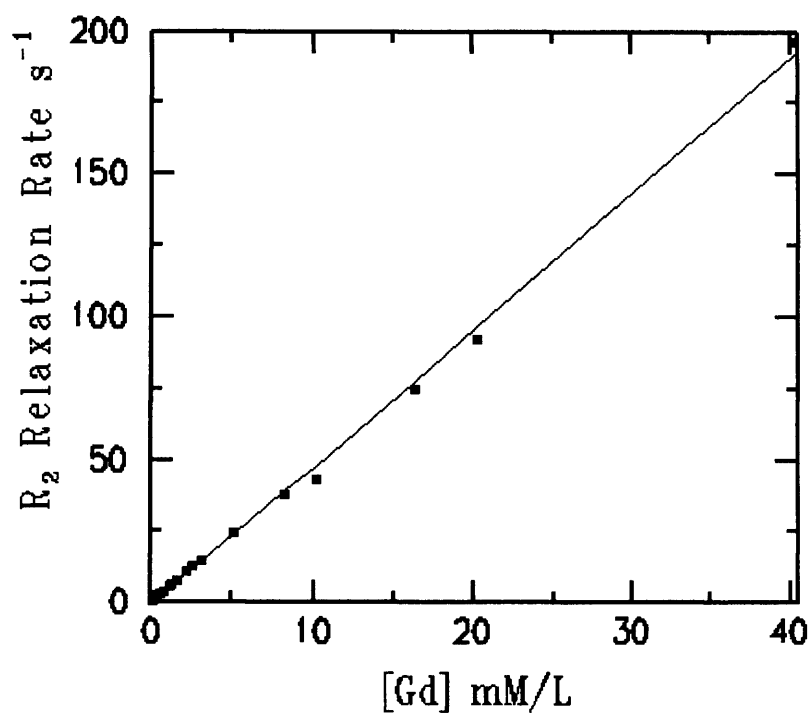


Figure 3.13. Graph showing the effect of [Gd] on the transverse relaxation time ( $R_2$ ). The line is the regression fit of the data points.

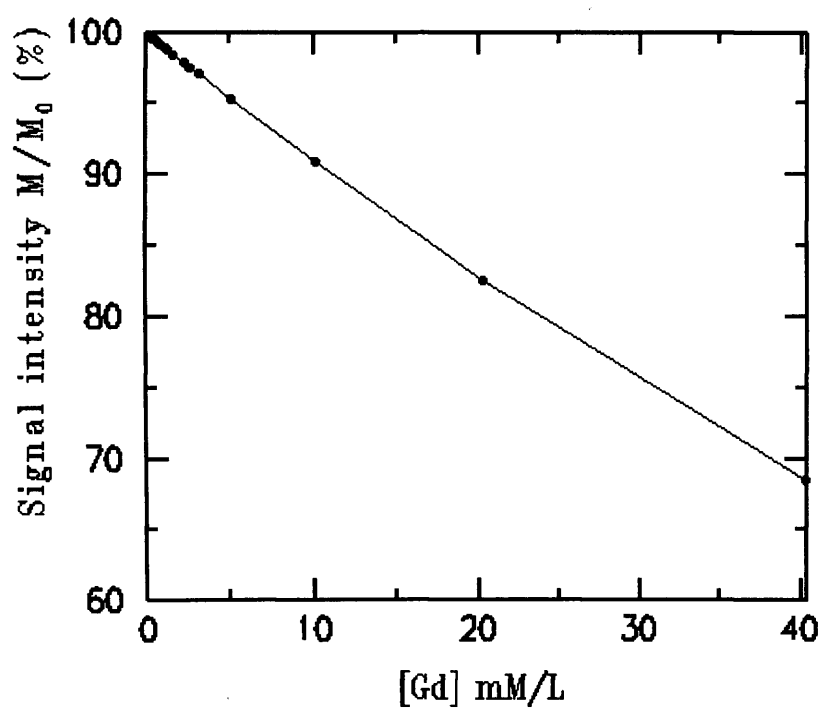


Figure 3.14. Graph showing the signal loss as a percentage of the  $M_0$  value, due to  $T_2$  effects. This has been estimated at the echo time used in the dynamic snapshot FLASH sequence (TE=2ms).

### 3.5.2 The effect of a reduction in the overall sequence repetition rate and ability to predict null point.

All results are shown as ratios of magnetisation measured using the snapshot FLASH sequence in steady state to that without the inversion pre-pulse. The ratio shown represents the mean of the four measurements, and the error bars show  $\pm 2$  standard deviations. A correction for background noise in these magnitude images was performed using the method described by Henkelman (1985), the magnitude of the noise having been measured in a region of the image outside the sample. Figure 3.15, shows the magnetisation ratio for three values of  $TR_0$  ( $5 \times T_{1pre}$ ,  $1 \times T_{1pre}$ , and  $0.5 \times T_{1pre}$ ) overlaying the theoretical curves. The flip angle of  $\alpha$  for this plot was  $8^\circ$ . Note that nulling of the myocardium equivalent solution is maintained throughout the changes in  $TR_0$  by adjustment of the inversion time.  $TI_{eff}$  was reduced from 519 ms for the longest  $TR_0$  down to 165 ms for the shortest  $TR_0$ .

The estimates of  $T_1$  using either Eq. [A1.6] or Eq. [A1.7] were made using an iterative search scheme. Either Eq. [A1.6] or Eq. [A1.7] was used to predict the signal intensity ratio (magnetisation in steady-state to magnetisation when measured without an inversion pulse), and the value of  $T_1$  in these equations was systematically searched in order to find the one which gave the measured intensity ratio. The flip angle in Eq. [A1.6] was fixed to the value calibrated by the scanner.

Figure 3.16, summarises the errors that are introduced into the estimation of  $R_1$  by using Eq. [A1.9], when  $TR_0$  is reduced. The mean and standard deviation of the  $R_1$  values were calculated using Eq. [A1.9] and the full Eq. [A1.6]. These values are plotted against the  $R_1$  measurement using the saturation recovery sequence, for the values of  $TR_0$ :  $5 \times T_{1pre}$ ,  $1 \times T_{1pre}$ , and  $0.5 \times T_{1pre}$  ( $\alpha = 8^\circ$ ).

When  $TR_0 > 5 \times T_{1pre}$ , both methods essentially obtained the same result, and this is in agreement with the saturation recovery measurement of  $T_1$ , so was not plotted. However as the  $TR_0$  is reduced, the use of Eq. [A1.9], introduces considerable error at the shorter  $R_1$  values. The  $TR_0$  reduction from  $1 \times T_{1pre}$  to  $0.5 \times T_{1pre}$ , increased the mean standard deviation of the  $R_1$  for Eq. [A1.6] from  $0.17 \text{ s}^{-1}$  to  $0.69 \text{ s}^{-1}$  and for Eq. [A1.9] from  $0.11 \text{ s}^{-1}$  to  $0.4 \text{ s}^{-1}$  respectively. This was due to the reduced signal to noise ratio at the lower values of  $TR_0$ .

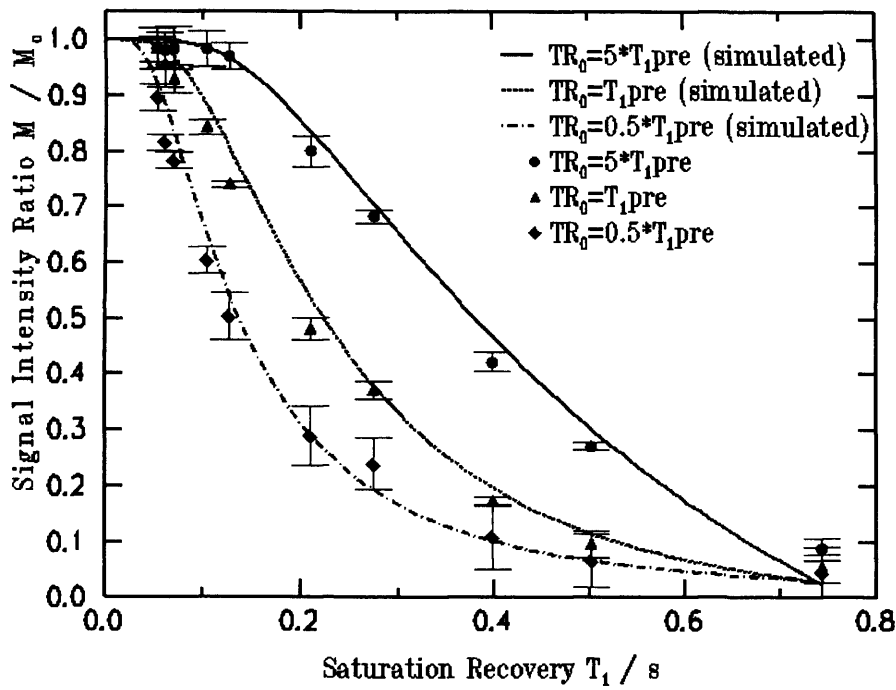


Figure 3.15. Normalised signal intensity response for three values of  $TR_0$ , flip angle= $8^\circ$ . Simulated and mean measured data ( $\pm 2 \times$  standard deviation) are shown.

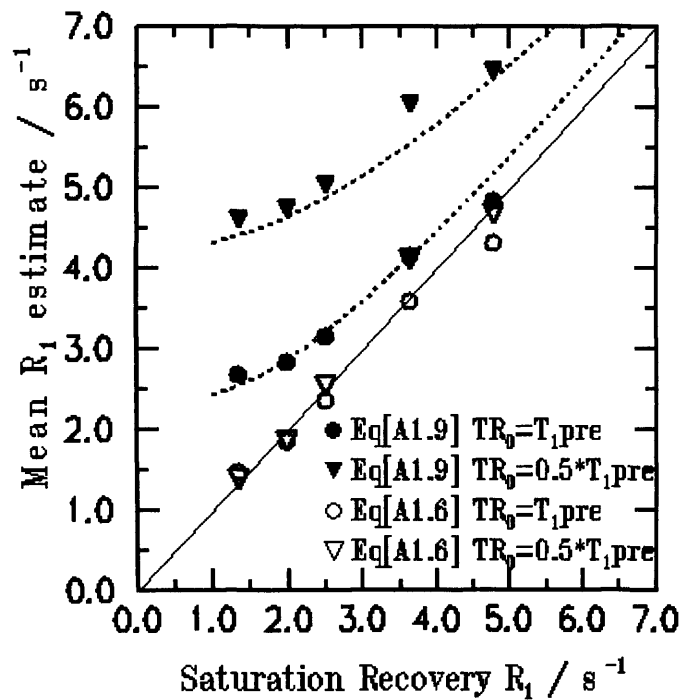


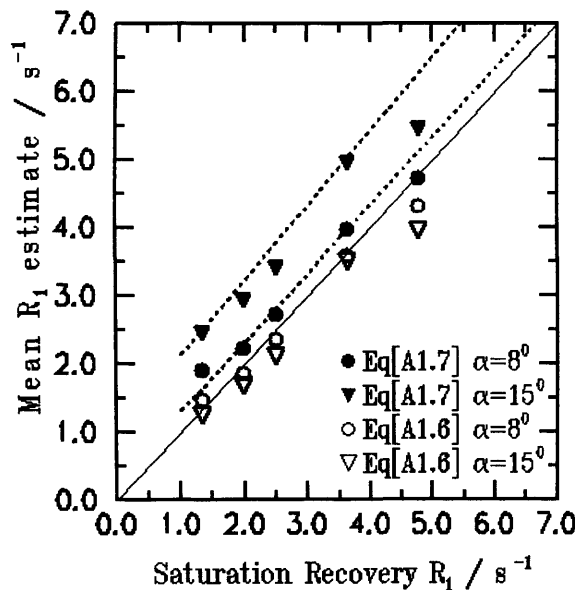
Figure 3.16. Mean estimation of  $R_1$  for three values of  $TR_0$  using the simplified analysis of Eq. [A1.9], and the full analysis of Eq. [A1.6], for  $TR_0=5 \times T_{1pre}$ ,  $TR_0=T_{1pre}$  and  $TR_0=0.5 \times T_{1pre}$ . These are the same experimental data as shown in Figure 10, presented to show the errors that occur in  $R_1$  estimation when using the simple analysis. The dashed lines represent the theoretical  $R_1$  estimates that would be expected when using Eq. [A1.9] to analyse data with a short  $TR_0$  and  $\alpha = 8^\circ$ .

### 3.5.3 The effect of altering the read pulse flip angle.

The accuracy of  $T_1$  measurement at the flip angles of  $1^\circ$ ,  $8^\circ$  and  $15^\circ$  were calculated using Eq. [A1.7], which does not allow for the effect of larger flip angles, and also the full Eq. [A1.6]. The data for a flip angle of  $1^\circ$  showed the most unbiased estimate of  $R_1$  compared to the saturation recovery method, so was not plotted. However because of the poor signal-to-noise ratio, this flip angle also showed the highest mean standard deviations for both Eq. [A1.7] and Eq. [A1.6], compared to the other flip angles of  $8^\circ$  and  $15^\circ$  and is shown in Table 3.1. As the flip angles are increased there is a trend towards overestimation of  $R_1$ . This systematic error is corrected by the use of Eq. [A1.6], and is shown in Figure 3.17.

Equation Used	Flip Angle of $\alpha$ pulses.		
	$1^\circ$	$8^\circ$	$15^\circ$
Simple analysis Eq. [7]	$0.73 \text{ s}^{-1}$	$0.15 \text{ s}^{-1}$	$0.22 \text{ s}^{-1}$
Full analysis Eq. [6]	$0.69 \text{ s}^{-1}$	$0.17 \text{ s}^{-1}$	$0.2 \text{ s}^{-1}$

Table 3.1. Standard deviation of the  $R_1$  for each flip angle using the simple and full analysis.



*Eq 7 allows for  
short TR but  
assumes a small  
flip angle.*

Figure 3.17. Mean estimation of  $R_1$  for flip angles,  $1^\circ$ ,  $8^\circ$  and  $15^\circ$  when  $TR_0 = T_1$  myo; other sequence parameters are as described in the text.  $R_1$  was estimated using the low flip angle approximation of Eq. [A1.7], and the full analysis of Eq. [A1.6]. the error introduced by the low flip angle approximation is relatively small until the flip angle exceeds about  $8^\circ$ . The dashed lines represent the theoretical  $R_1$  estimates that would be expected when using Eq. [A1.7] to fit the data where the flip angle cannot be considered small.

### 3.6 Discussion.

This chapter has investigated the effect of flip angle of the  $\alpha$  pulses, and reduction in the overall sequence repetition time, and their effect on the calculation of  $T_1$  using a snapshot FLASH. These findings show that if these factors are ignored, there will be a systematic underestimation of  $T_1$ . The application of Eq. [A1.6], allows for the saturation of the magnetisation, and leads to accurate  $T_1$  estimation even at short  $TR_0$ 's, and practical flip angles.

This work has implications for perfusion imaging, where a fast sequence such as snapshot FLASH is used in combination with cardiac gating. Fast cardiac gated  $T_1$  imaging during the passage of a bolus of contrast agent, enables qualitative studies of myocardial perfusion *in vivo* (Wilke *et al* 1994). If  $T_1$  can be measured accurately then it may be possible, through the change in concentration of a contrast agent (Burstein *et al* 1991) to quantify myocardial perfusion (Larsson *et al* 1994, Deisbourg *et al* 1992). However, the use of a single exponential model of  $T_1$  relaxation does not allow the complexities of multicomponent behaviour to be measured.

It can be seen from Fig. 3.11 that deviations in the flip angle do not have a major impact on the computed  $T_1$  for moderate changes of flip angle. It is therefore expected that if the flip angle varies throughout the slice, as can be the case for the short R.F. pulses used in snapshot FLASH sequences, then this should not affect the computed  $T_1$  greatly. The use of centric phase encoding helps to reduce the saturation effect of the flip angle (Chein 1991). It has been shown that, although the flip angle of the  $\alpha$  pulses contributes to inaccuracy, the largest effect is due to the reduction in overall sequence repetition. This is a factor which has to be taken into account when a fast imaging sequence such as the snapshot FLASH sequence is cardiac gated, and requires multiple rapid measurements.

The use of short overall sequence repetition times has consequences for the range of  $T_1$  values which can be measured accurately. As can be seen from Figure 3.7, a common problem is the inaccuracy in  $T_1$  estimation at low values of  $T_1$ : magnetisation recovers very quickly with almost complete relaxation after the inversion pulse with very little signal decrease up to quite large values of  $T_1$ . As  $TR_0$  is reduced, the change in signal intensity with  $T_1$  becomes considerably greater at these low  $T_1$  values. However, this is at the expense of the very flat response around the null point. This latter point necessitates using a



scheme for the correction of noise (Henkelman 1985) if accurate  $T_1$  measurement is to be maintained for  $T_1$  values around the null-point.

The signal loss due to  $T_2$  relaxation was estimated at a range of contrast agent values. This has implications for the correction factor required for the  $M_0$  image, as failure to do so will lead to an overestimation of the  $T_1$  relaxation rate. However, for calculation of the  $M_0$  correction factor for the snapshot FLASH sequence requires the estimation of  $T_2^*$  signal loss, which is likely to be greater than the  $T_2$  signal loss. This we were not able to calculate upon our scanner due to technical difficulties with the sequence.

### 3.7 Conclusions.

This study has shown that a simplistic analysis of the snapshot FLASH sequence can lead to significant errors in  $T_1$  measurement if either the overall sequence repetition time is reduced to improve temporal resolution or large flip angle read-out  $\alpha$  pulses are used. A fuller analysis is required which takes into account both of these effects and removes the distorting influences of short overall sequence repetition times and large flip angle  $\alpha$  pulses. An additional benefit of using a shortened overall sequence repetition time is that the accuracy of the estimated  $T_1$  should be improved at low  $T_1$  values. However, this is at the expense of sensitivity at higher  $T_1$ .

The improved accuracy of monoexponential  $T_1$  estimates has the implications not only for perfusion studies of the heart, but for any system where rapid  $T_1$  measurements are required.

### 3.8 References

Bakker CJG, de Graaf CN, van Dijk P. Restoration of signal polarity in a set of inversion recovery NMR images. *IEEE Trans Med Imag* MI-3:197-202 1984

Bakker CJG, Vriend J. Multi-exponential water proton spin lattice relaxation in biological tissues and its implications for quantitative NMR imaging. *Phys Med and Biol* 29:509-518 1984

Barker GJ, Mareci TH. Suppression of artifacts in multiple echo magnetic resonance. *J Magn Reson*, 83:11-28 1989

Bluml S, Schad LR, Stepanow B, Lorenz WJ. Spin lattice relaxation time measurement by means of a turboFLASH technique. *Magn Reson Med*, 30:289-295 1993

Borrello JA, Chenevert TL, Aisen AM. Regional phase correction of inversion recovery MR images. *Magn Reson Med*, 14:56-67 1990

Bottomley PA, Andrew ER. RF magnetic field penetration, phase shift and power dissipation in biological tissues: implications for NMR imaging. *Phys Med Biol*, 23:630-643 1978

Bottomley PA, Foster TA, Argersinger RE, Pfeifer LM. A review of normal tissue hydrogen relaxation times and relaxation mechanisms from 1-100 MHz: dependance on tissue type, NMR frequency, temperature, species, excision and age. *Med phys* 11:425-448 1984

Brix G, Schad LR, Deimling M, Lorenz WJ. Fast and precise  $T_1$  imaging using a TOMROP sequence. *Magn Reson Imaging*, 8:351-356 1990

Burstein D, Taratuta E, Manning WJ. Factors in myocardial 'perfusion' imaging with ultrafast MRI and Gd-DTPA administration. *Magn Reson Med*, 20:299-305 1991

Chein D, Edelman RR. Ultrafast imaging using gradient echos. *Magn Reson Q*, 7(1):31-56 1991

Diesbourg LD, Prato FS, Wisenberg G, Drost DJ, Marshall TP, Carrol SE, O'Neil B. Quantification of myocardial blood flow and extracellular volumes using a bolus injection of Gd-DTPA: Kinetic modeling in canine ischemic disease. *Magn Reson Med*, 23:239-253 1992

Edelstein WA, Glover GH, Hardy CJ, Redington, RW. The intrinsic signal-to-noise ratio in NMR imaging. *Magn Reson Imaging*, 3:604-618 1986

Edelstein WA, Hutchinson JMS, Johnson G, Redpath TW. Spin warp NMR imaging and applications to whole body imaging. *Phys Med Biol*, 25:751-756 1980

Frahm EK, Hänicke W, Merboldt K-D. Transverse coherence in rapid FLASH NMR imaging. *Magn Reson Med*, 72:307-314 1987

Frahm EK, Merboldt K-D, Hänicke W, Haase A. Stimulated echo imaging. *J Magn Reson*, 64:81-93 1985

Freeman R, Hill HDW, Kaptein R. An adaptive scheme for measuring NMR spin-lattice relaxation times. *J Magn Reson*, 7:82-98 1972

Gowland PA, Leach MO. A simple method for the restoration of signal polarity in multi-image inversion recovery sequences for measuring  $T_1$ . *Magn Reson Med*, 18:224-231 1991

Gowland PA, Leach MO. Fast and accurate measurements of  $T_1$  using a multipoint single inversion recovery sequence. *Magn Reson Med*, 26:79-88 1992

Graumann R, Barfuß H, Hentschel D, Oppelt A. TOMROP: a sequence for determining the longitudinal relaxation time  $T_1$  in magnetic resonance imaging. *Electromedica*, 55(2):67-72 1987

Graumann R, Deimling M, Heilmann T, Oppelt A. A new method for fast and precise  $T_1$  determination. Abstr. SMRM 5th Meeting, SMRM, Berkley California, 922-923 1986

Gupta RK. A new look at the method of variable nutation angle for the measurement of spin lattice relaxation times using fourier transform NMR. *J Magn Reson*, 25:231-235 1977

Haase A, Frahm J. NMR imaging of spin-lattice relaxation using simulated echos. *J Magn Reson*, 65:481-490 1985

Haase A. Snapshot FLASH MRI. Applications to  $T_1$ ,  $T_2$ , and chemical-shift imaging. *Magn Reson Med*, 13:77-89 1990

Hahn EL. Spin echos. *Phys Rev*, 80: 580-594 1950

Henkelman RM. Measurement of signal intensities in the presence of noise correction. *Med Phys*, 12(2):232-233 1985

Hickey DS, Checkley D, Aspden RM, Naughton A, Jenkins JPR, Isherwood I. A method for the clinical measurement of relaxation times in magnetic resonance imaging. *Br J Radiol*, 59:565-576 1986

Homer J, Beevers MS. Driven-equilibrium single pulse observation of  $T_1$  relaxation. A reevaluation of a rapid 'new' method of determining NMR spin-lattice relaxation times. *J Magn Reson*, 63:287-297 1985

Just M, Higer HP, Pfannenstiel P. Errors in  $T_1$  determination using multi-slice technique and gaussian slice profiles. *Magn Reson Imaging*, 6:53-56 1988

Kaptein R, Dijkstra K, Tarr CE. A single scan fourier transform method for measuring spin-lattice relaxation times. *J Magn Reson*, 24:295-300 1976

Kay I, Henkelman RM. Practical implementation and optimisation of one-shot  $T_1$  imaging. *Magn Reson Imaging*, 22:414-424 1991

Larsson HBW, Stubgaard M, S ndergaard L, Henriksen O. *In vivo* quantification of the unidirectional influx constant for Gd-DTPA diffusion across the myocardial capillaries with MR imaging. *J Magn Reson*, 4:433-440 1994

Lin MS, Fletcher JW, Donati RM. Two point  $T_1$  measurement: Wide coverage optimisations by stochastic simulations. *Magn Reson Med*, 3:518-533 1986

Look DC, Locker DR. Time saving in measurement of NMR and EPR relaxation time. *Rev Sci Instrum* 41:250-251 1970

Mander AJ, Smith MA, Kean DM, Chick J, Douglas RHB, Rehman AU, Weppner GJ, Best JJK. Brain water measured in volunteers after alcohol and vasopressin. *Lancet* ii, 1057 1985

Mareci TH, Sattin W, Scott KN. Tip angle reduced  $T_1$  imaging. *J Magn Reson*, 67:55-65 1986

Mather-De Vre R. Biomedical implications of the relaxation behavior of water related to NMR imaging. *Br J Radiol*, 57:955-976 1984

Park HW, Cho MH, Cho ZH. Real-value representation in inversion recovery NMR by use of a phase-correction method. *Magn Reson Med*, 3 15-23 1986

Redpath TW. Noise correlation in multicoil receiver systems. *Magn Reson Med*, 24:85-89 1992

Rostrup E., Larsson H.B.W., Fritz-Hansen T., Ring P., Henriksen O. , *Book of Abstracts: Proceedings of the Society of Magnetic Resonance, and European Society for Magnetic Resonance in Medicine and Biology*, p 1062, 1995.

Sattin W, Mareci TH, Scott KN. Exploiting the stimulated echo in nuclear magnetic resonance imaging. I. Method. *J Magn Reson*, 64:177-182 1985

Sattin W, Mareci TH, Scott KN. Exploiting the stimulated echo in nuclear magnetic resonance imaging. II. Applications. *J Magn Reson*, 65:298-307 1985

Sutherland RJ, Hutchinson JMS. Three dimensional NMR imaging by selective excitation. *Journal of Phys E: Scientific Instruments*, 11:79-83 1977

Wang HZ, Reiderer SJ, Lee JN. Optimising the precision in  $T_1$  relaxation estimation using limited flip angles. *Magn Reson Med*, 5:399-416 1987

Wilke N., Jerosch-Herold M., Stillman A.E., *et al.* Concepts of myocardial perfusion imaging in magnetic resonance imaging. *Magn Reson Q*, 10(4), 249 1994

Young IR, Bailes DR, Bydder GM. Apparent changes of appearance of inversion recovery images. *Magn Reson Med*, 2:81-85 1985

Zhang YT, Yeung HN, Carson PL, Ellis JH. Experimental analysis of  $T_1$  imaging with a single scan, multipoint, inversion recovery technique. *Magn Reson Med*, 25:337-343 1992

## **Chapter 4: The dynamic measurement of myocardial $T_1$ relaxation *in vivo* using snapshot FLASH**

### **4.1 Introduction**

#### **4.1.1 Reasons for measuring relaxation *in vivo***

The measurement of relaxation times in MR imaging stems from the early observations of relaxation times in experimental animals. Relaxation times enable the characterisation of tissue. Fat has a very short  $T_1$ , and so it can easily be distinguished from other tissue. This has been used by researchers to assess percentage foetal fat (Deans *et al* 1989). Damadian (1971) found that tumourous tissue exhibited an increase in  $T_1$  and  $T_2$ . Bloch *et al* (1991) applied a computer algorithm to  $T_2$  maps of the head and neck to demarcate tumour boundaries. This would then enable the target volume for radiotherapy to be automatically located.

The measurement of relaxation times have been used to assess other parameters. For example,  $T_1$  relaxation times are temperature dependant, and can therefore be used to encode the temperature distribution within tissue (Parker *et al* 1983). Clinically,  $T_1$  measurement enables the non-invasive temperature mapping of hypoxic tumours during hyperthermia treatment (Dickinson *et al* 1986, Hall *et al* 1990).

Using cluster analysis,  $T_2$  relaxation times together with diffusion weighted MR imaging has been used to assess the development of acute ischaemic stroke (Welch *et al* 1995, Warach *et al* 1992,1995).  $T_2^*$  maps of the brain are employed in functional MR imaging (fMRI) (Carswell 1993). It relies on the changes in blood oxygenation state as deoxyhaemoglobin is paramagnetic. This enables the assessment of changes in cerebral blood flow and therefore areas of increased brain activity in response to a task to be located.

Relaxation times are very complex, and the use of relaxation time maps alone to reach a diagnosis cannot be relied upon. This is because clinical studies have shown that there is a wide variation in relaxation times in both normal and pathological tissues

(Bottomley 1987). However, relaxation time measurements have been shown to be useful in evaluating the effectiveness of therapy. When performed over a period of time on the same patient, they can enable the monitoring of disease progression or the effectiveness of treatment (Anderson *et al* 1989). Tofts *et al* (1990) found relaxation time measurements to be useful in differential diagnosis of brain disease when used in conjunction with conventional imaging.

Finally, the contrast between tissues can be optimised for a particular imaging sequence if the relaxation times are known (Perman *et al* 1984). The sequence timing parameters can be chosen to allow the desired contrast to detect pathology, enabling the optimum imaging protocol for a given scan time (Bydder *et al* 1985).

The use of synthetic images can further allow optimisation of the sequence. Source images are acquired with one pulse sequence and the proton density and relaxation times are calculated (Bobman *et al* 1986). This information is then used to generate images for an entirely different pulse sequence enabling optimisation of contrast retrospectively, without any additional imaging time.

#### **4.1.2 Measurement of myocardial $T_1$ relaxation *in vivo***

As  $T_1$  and  $T_2$  are altered in some pathological tissues (Damadian 1971), it was hoped that accurate measurement of these parameters would distinguish between normal and pathological tissue. However, the wide biological heterogeneity of relaxation times (Bottomley *et al* 1987) may at least partly be attributable to the inaccuracy of the experimental methods used in the clinical scanning situation (Johnson *et al* 1987, Masterson *et al* 1989).

A one-shot sequence that allows precise  $T_1$  measurements is TOMROP (*T One by Multiple Read Out Pulses*) (Brix *et al* 1990) first proposed for spectroscopy by Look and Locker (1970), and adapted for imaging by Graumann *et al.* (1987). This was denoted one-shot, as it requires only one imaging experiment to acquire a series of images for  $T_1$  calculation. In this sequence, the longitudinal magnetisation is repeatedly sampled (1 sample per image) as it approaches a steady state, either from an unperturbed state or following a  $90^\circ$  or  $180^\circ$  pulse. This process is repeated for each phase encoding step, to produce a series of images with different  $T_1$  weightings, and requires approximately 10 minutes of imaging time. Variants of this (Crawley *et al* 1987, Kay *et al* 1991, Gowland *et al* 1992, Zhang *et al* 1992) have been used to measure multi-exponential relaxation



(Graumann *et al* 1986,1987, Kay *et al* 1991, Gowland *et al* 1992) required for accurate evaluation of  $T_1$  in some tissues.

An alternative sequence enabling multiple images to be obtained is to measure  $T_1$  an inversion recovery snapshot FLASH (*Fast Low Angled Shot*) or TurboFLASH imaging sequence (Haase 1990). Here an inversion pulse is applied, and as the longitudinal magnetisation recovers, all the phase encoding steps are acquired for a series of images. The acquired images will have different  $T_1$  weightings depending on which point in the longitudinal relaxation curve they were acquired. There is a change in longitudinal magnetisation due to the application of the read-out pulses and a method of correction for this has been shown (Deichmann *et al* 1992).

If  $T_1$  is changing rapidly then methods that need multiple images may not be practical. Measurement of  $T_1$  can be achieved in the shortest time by repeatedly acquiring just a single  $T_1$ -weighted image which, in conjunction with a static measure of the equilibrium magnetisation, can be used to calculate  $T_1$ . In this context, the inversion recovery snapshot FLASH sequence (Haase 1990) for dynamically measuring  $T_1$  assuming mono-exponential relaxation (Bluml *et al* 1993) is investigated. Here, an inversion pulse is applied and, after the inversion time (TI), a train of read-out pulses gives a single image in one shot. The contrast in the image is determined by the position of the central phase encoding step in the longitudinal relaxation curve and can be altered by changing TI.

#### **4.1.3 Considerations for *in vivo* myocardial $T_1$ measurement**

The measurement of myocardial  $T_1$  *in vivo* needs several practical considerations. As the heart is moving, imaging is targeted to the point at which there is minimal heart movement, late diastole. This is achieved through ECG gating where the R-wave triggers imaging and a delay can be incorporated to image at the chosen point in the cardiac phase. The added advantage of imaging the heart at the same cardiac phase is that the myocardial blood volume is likely to be comparable.

The myocardial  $T_1$  values obtained *in vivo* can be compared between types of *in vivo* measurement regimes, i.e. with and without ECG gating, and dynamic measurement with a choice of inversion time. The correction that is applied where there is a reduction in the overall sequence repetition time due to the ECG gating of scans, has been validated in phantoms in the previous chapter. In this chapter, these techniques are applied *in vivo*. A recent study suggests that phantom validation does not ensure accurate  $T_1$  measurements *in*

*vivo* due to variations in the RF pulse flip angle (Kingsley *et al* 1997). This may be homogenous over a phantom, but may vary over the body and may lead to systematic errors in  $T_1$  measurement where accurate flip angles are required. The phantom study has shown that the largest error is due to the reduction in the overall sequence repetition time which has now been corrected for and applied to obtain myocardial  $T_1$  values *in vivo*.

## 4.2 Aims

The study presented in this chapter investigates the effect of rapid  $T_1$  measurement in the heart using a standard clinical snapshot FLASH sequence. The snapshot FLASH sequence has the temporal resolution to image rapidly changing dynamic processes, such as the first pass of a bolus of contrast agent. Using a standard clinical MRI scanner its subsecond image acquisition enables imaging studies to be cardiac gated. However, errors may be introduced in  $T_1$  measurement when the snapshot FLASH sequence is cardiac gated because this may not allow full longitudinal relaxation ( $>5 \times \text{longest } T_1$ ) before the acquisition of each image.

At baseline the myocardial  $T_1$  is at its longest as the bolus of contrast agent has not reached the myocardium. It is important that this baseline measure is correct as the estimate of contrast agent concentration is achieved through calculation of the change in the relaxation rate  $R_1 (=1/T_1)$ .

As the bolus of contrast agent reaches the myocardium, the myocardial  $T_1$  is reduced ( $R_1$  is increased). The effect of heart rate on the error in  $T_1$  estimation over a range of  $T_1$  values (representing pre and post contrast myocardium) is explored.

The inversion time in a dynamic snapshot FLASH sequence is set to null the signal from the tissue to be imaged. This increases the signal range when the contrast agent is introduced into the tissue. However, the dynamic signal range for this sequence extends from  $-1$  to  $+1 \times M_0$ . The image is generally reconstructed and displayed as a magnitude image, which can introduce errors into the calculation of  $T_1$ . If the correct inversion time is not chosen there will be two possible calculated  $T_1$  values due to contrast reversal (Young *et al* 1985).

During the calculation of the baseline (pre contrast) myocardial  $T_1$ , multiple images with different values of TI can be used (MTI). This is time consuming since full

longitudinal relaxation is allowed between inversion pulses, but the baseline myocardial  $T_1$  value obtained will be more accurate.

The approximate myocardial  $T_1$  at 1.0T is 0.75s which would require an effective inversion time of 0.45s. However, if the  $T_1$  of the myocardial tissue was increased, e.g. due to oedema, or if the signal from the left ventricular blood was to be imaged, e.g. for kinetic modelling purposes, errors in the calculated  $T_1$  would be introduced due to contrast reversal when using dynamic snapshot FLASH. Here, the dependence of the calculated  $T_1$  value on the TI used is investigated.

MRI scans of the myocardium are ECG gated to obtain images at the same phase of the cardiac cycle, so the blood volume is constant. Images of the heart were obtained at late systole.

Here the effect of ECG gating of myocardial MRI scans is explored. The snapshot FLASH sequence has the effect of "freezing" cardiac motion, so acquiring images when cardiac motion is minimal is not essential. As the heart rate may vary slightly during dynamic imaging measures, there may be errors in the correction for the overall sequence repetition time. This would not arise if the sequence was not ECG gated, and there would be a constant time interval between the dynamic imaging measures. The cardiac phase and therefore the myocardial blood volume may vary between the dynamic measurements, and this would be reflected in the calculated  $T_1$  values.

The myocardial  $T_1$  values found using multiple images with different values of TI (MTI) are compared within and between volunteers. This is to establish a baseline (pre contrast) myocardial  $T_1$  value, and the range of  $T_1$  values for normal myocardium in the study population.

In summary, the aims of this chapter are to investigate the effect on the measured  $T_1$  of: a) the heart rate or sequence repetition time ( $TR_0$ ), b) the inversion time and, c) ECG gating of scans *vs.* no gating. The baseline pre contrast myocardial  $T_1$  is also established from normal volunteers.

### 4.3 Method

All experiments were performed using a whole body MRI system (MAGNETOM IMPACT, Siemens, Erlangen, Germany) operating at 1.0 Tesla. A linearly polarised body coil was used for R.F. transmission and reception of the NMR signal. The system was

equipped with actively shielded magnetic field gradient coils, giving gradient strengths of up to 15mT m<sup>-1</sup> with rise times of 1ms.

#### 4.3.1 The effect of the heart rate (TR<sub>0</sub>) on $T_1$ values in normal and abnormal myocardium.

The snapshot FLASH sequence was used to measure *in vivo* myocardial  $T_1$ . After obtaining ethics committee approval, fourteen patients admitted to our hospital with acute myocardial infarction were scanned within 2-4 days of the event. These patients were also assessed using <sup>201</sup>thallium single photon emission computed tomography (SPECT).

Short axis images through the left ventricle were obtained using a three slice snapshot FLASH sequence, the slices were positioned above, through and below the papillary muscle. The imaging parameters were  $\alpha=8^\circ$ ; TR=4.7ms; TE=2ms; FOV=250ms; 64×64 data matrix; 10mm thick slices. Acquisition was cardiac gated so that the midline of  $k$ -space was acquired in ventricular systole. The heart rate of each patient was recorded during the scan.

On each image, the left ventricular myocardium was divided radially and evenly into ten regions of interest (ROI's) (Figure 4.1, below), and the mean signal intensity was found for each ROI.

##### 4.3.1.1 Baseline (pre contrast) $T_1$ measurement

To measure the baseline myocardial  $T_1$ , first an  $M_0$  scan for each slice was acquired after full relaxation. This is achieved by turning off the inversion pre pulse in the snapshot FLASH sequence. The heart was then imaged using the snapshot FLASH sequence, eight measurements were made with the inversion time decreased from 1.85s to 0.15s, allowing full longitudinal relaxation between each image slice (MTI method).

The baseline  $R_1$  was calculated by non linear curve fitting to a plot of inversion time vs. mean signal intensity using an equation of the form:

$$SI = M_o (1 - 2 e^{-TI_{eff}/T_1}) \quad [4.1]$$

where,  $TI_{eff}$  is the time from the inversion pulse to the mid-line of  $k$ -space usually called the effective TI, and is often  $TI + (TR \times (N_k / 2))$ .

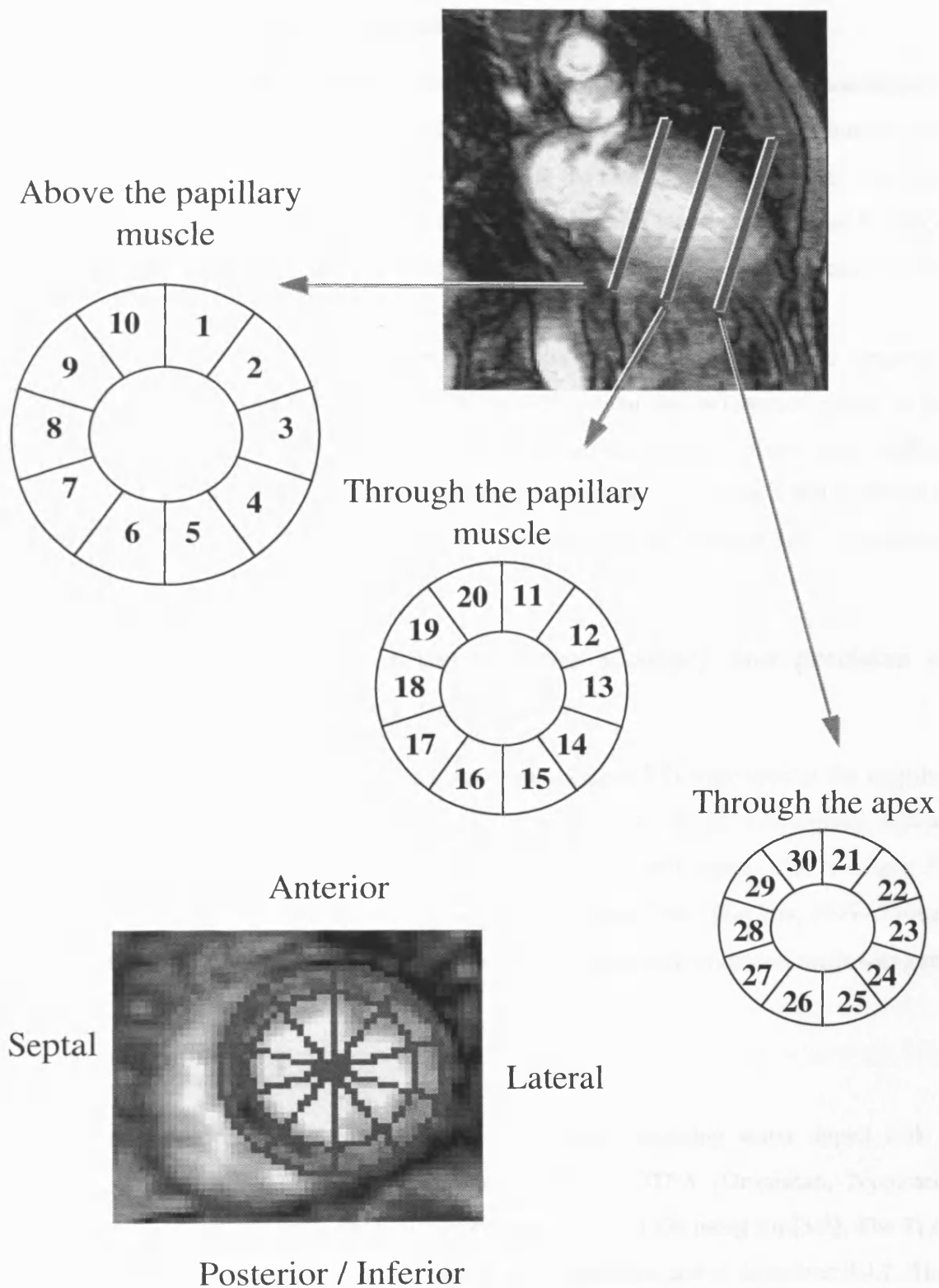


Figure 4.1. Three short axis images are obtained from the left ventricle. Each image is divided equally into ten regions of interest (ROI), producing thirty regions of interest per patient.

#### 4.3.1.2 $T_1$ measurement during contrast injection

An  $M_0$  image was acquired for each slice, then the heart was imaged continuously during the injection of  $0.05\text{mol kg}^{-1}$  gadobenate dimeglumine (Gd-BOPTA) contrast agent (Bracco SpA, Milan, Italy). Images were acquired at the rate of one image every two heart beats. The time interval between each of the snapshot FLASH measurements was recorded. The inversion time for the sequence was 300ms and all the other parameters were the same as above.

The  $R_1$  was calculated twice for each region of interest first with the simplified analysis of Eq.[A1.9], then the full Eq.[A1.6]. In each patient, the differences caused by the simplified verses the full analysis were then assessed in the slice above the papillary muscle. The differences between the two analyses were compared in ROI's that appeared to have normal  $^{201}\text{thallium}$  and abnormal (reduced) uptake, as assessed by a Consultant Radiologist.

#### 4.3.2 The effect of inversion time on the accuracy and precision of snapshot FLASH in measuring $T_1$ *in vivo*.

To measure the effect of inversion time, two different TI's were used in the snapshot FLASH sequence. TI=300ms was used to null the signal from normal myocardium, with an approx.  $T_1=0.75\text{s}$ . Then, a longer TI=850ms was used to null signal with a longer  $T_1$ , approx. 1.4s. Other sequence parameters were  $\alpha=8^\circ$ ; TR=4.7ms; TE=2ms; FOV=250ms;  $64\times 64$  data matrix; 10mm thick slices.  $R_1$  was calculated for both inversion times using the full analysis Eq.[A1.6].

##### 4.3.2.1 Phantom studies

A phantom consisting of 9 separate vials each containing water doped with a different concentration (0.1086 to 0.8 mmol/L) of Gd-DTPA (Omniscan, Nycomed, Norway), was used to give a range a  $T_1$  values from 1.2s to 0.25s using Eq.[3.2]. The  $T_1$  of these phantoms was measured using a gradient echo sequence, and is described 3.4.2. This allowed mean  $T_1$  values to range from 1.28s to 0.257s.

The snapshot FLASH sequence was used to image the phantoms using the two TI's. First an  $M_0$  image was obtained using the three slice snapshot FLASH sequence. Each of the slices were then obtained with a temporal resolution of 1.5s, corresponding to a heart

rate of 80 beats per minute (bpm). Six measurements were taken. The sequence delay was altered using Eq.[4.2] to ensure that imaging was completed within two RR intervals, and thus the temporal resolution was constant.

$$\text{Sequence Delay} = (1.3 \times \text{RR interval}) - \text{TI}_{\text{eff}} \quad [4.2]$$

where TI is the inversion time, TR is the repetition time, and  $\text{TI}_{\text{eff}}$  is the effective inversion time. This is schematically represented in Figure 4.2.

The process was carried out twice, one for each TI. The first measurement was discarded, to allow for the signal to reach steady state. The first slice from each of the three measurements was analysed, and the  $R_1$  was calculated using the full analysis Eq.[A1.6] for each TI.

#### 4.3.2.2 Volunteer studies

Ten volunteers were imaged to investigate the effect of inversion time on the measurement of  $T_1$  *in vivo*. A questionnaire (shown in Appendix 2) was completed by each volunteer to assess the likelihood of heart problems, together with a twelve lead ECG which was assessed by an experienced cardiac research nurse.

$M_0$  images of the myocardium were obtained above, through and below the papillary muscle. ECG gated images of the myocardium were then acquired using the snapshot FLASH sequence which was varied to obtain:

##### 4.3.2.2 I Multiple TI (MTI) images

The inversion time was altered from 1.93s to 0.15s in 13 steps. Imaging was cardiac gated, and full longitudinal relaxation was allowed between each image acquisition. This was used to calculate  $R_1$  for each ROI using Eq.[4.1].

##### 4.3.2.2 II Dynamic images

Using a short TI ( $\text{TI}=300\text{ms}$ ), and long TI ( $\text{TI}=720\text{ms}$ ) and with all other snapshot FLASH imaging parameters constant (4.3.2), the inversion time was altered. Eleven measurements were obtained at each of the TI's, the sequence delay was altered Eq.[4.2], to ensure that the temporal resolution remained at a constant of  $2 \times \text{RR interval}$  for each volunteer.  $R_1$  was calculated for each ROI using the full analysis of Eq.[A1.6].

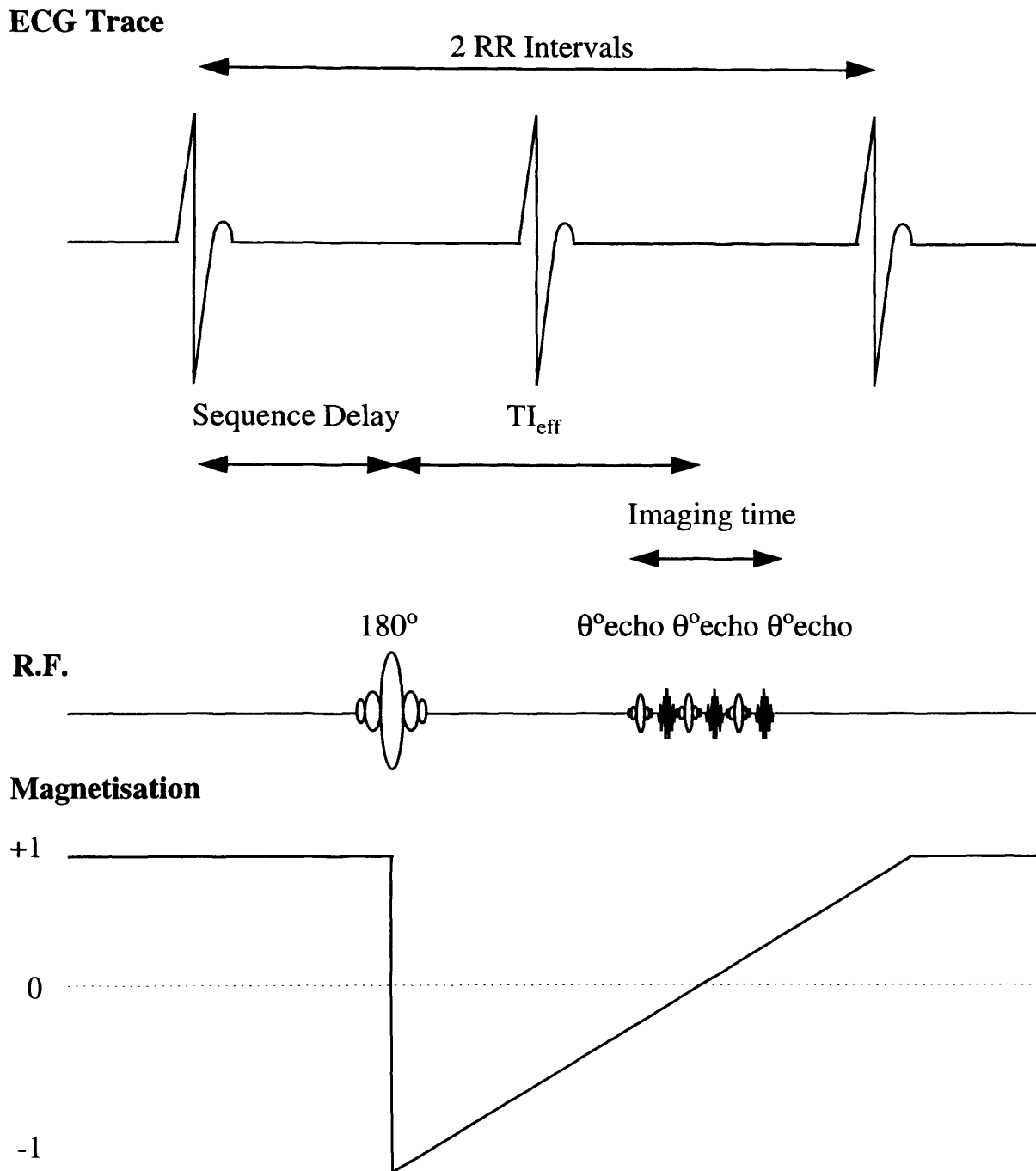


Figure 4.2. Schematic representation of an ECG gated snapshot FLASH imaging sequence. Imaging takes place over two R-R intervals. The first R wave triggers the sequence delay, at the end of which the  $180^\circ$  inversion pulse is applied. The  $M_z$  magnetisation is inverted and as it relaxes back it is imaged, with the centre lines of  $k$ -space acquired around the null point for myocardium.



### 4.3.3 The effect of ECG gating MRI scans on the myocardial $T_1$ values obtained

Five volunteers were re-imaged using the same parameters as 4.3.2.2.II, (long  $TI=820ms$ ) except that imaging was not ECG gated.  $R_1$  was calculated for each ROI using the full analysis of Eq.[A1.6].

## 4.4 Results

### 4.4.1 The effect of the heart rate ( $TR_0$ ) on $T_1$ values in both normal and abnormal myocardial regions of interest.

The patient data were arbitrarily divided into two groups: those with a slow heart rate ( $<80$  beats per minute [bpm]) (8 patients) and those with a fast heart rate ( $\geq 80$  bpm) (6 patients). Figure 4.3 and Figure 4.4 show the myocardial  $R_1$  vs. time in two of the fourteen patients with acute myocardial infarction. Figure 4.3 shows a patient with a fast heart rate (100 bpm) and Figure 4.4 shows one with a slow heart rate (60 bpm). Four ROI's are shown in each graph, two corresponding to normal and two for abnormal perfusion regions according to  $^{201}$ thallium SPECT assessment. The solid lines represent  $R_1$  values calculated using the fuller analysis (F.A.) of Eq.[A1.6] and can be compared to the dotted lines which represent the  $R_1$  values calculated using the simplified analysis (S.A.) of Eq.[A1.9]. The graphs show that the S.A. overestimates the  $R_1$ , but the degree to which this occurs varies dependant upon the  $R_1$  value and the heart rate.

Table 4.1 summarises the errors that occur when the simplified analysis is used to calculate  $R_1$ . The mean difference in  $R_1$  between the two methods of analysis was 10.5% which was statistically significant ( $p < 0.001$ ; Student's  $t$  test for paired data). The difference between the two methods is greater is when the heart rate is faster, because of the increased magnetisation saturation caused by the shorter sequence repetition time. Also, because of the shorter  $R_1$  in regions of infarction, there was greater error again due to magnetisation saturation.

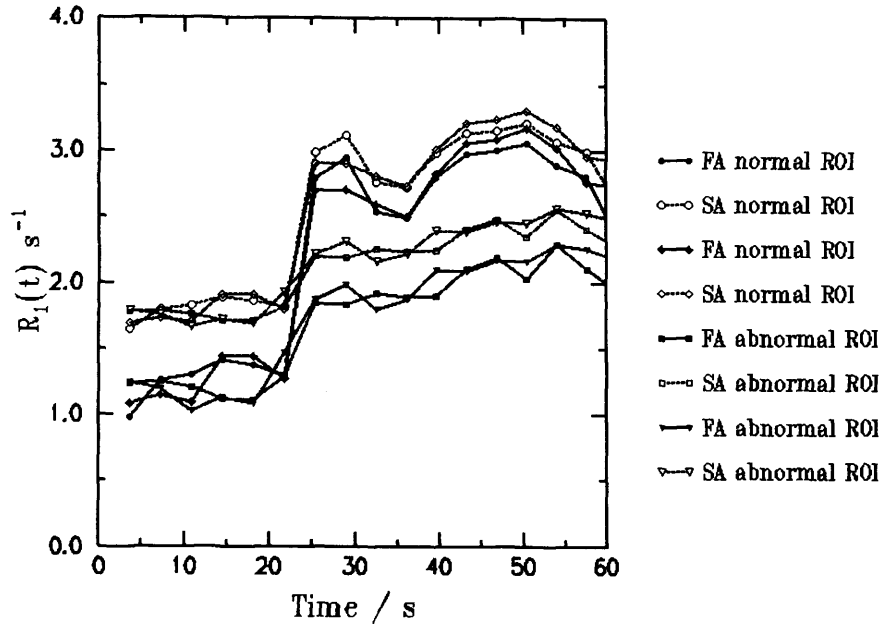


Figure 4.3. Graph showing the calculated  $R_1$  over time using the simplified analysis of Eq.[A1.9] and the full analysis of Eq.[A1.6] during the introduction of a contrast agent gadobenate dimeglumine (Gd-BOPTA). This is from a patient who had a fast heart rate (100 bpm) whilst dynamic imaging was being undertaken. Four ROI's are shown from the image slice above the papillary muscle. Two ROI's assessed as normal and two assessed as abnormal (reduced)  $^{201}\text{Tl}$  uptake are shown.

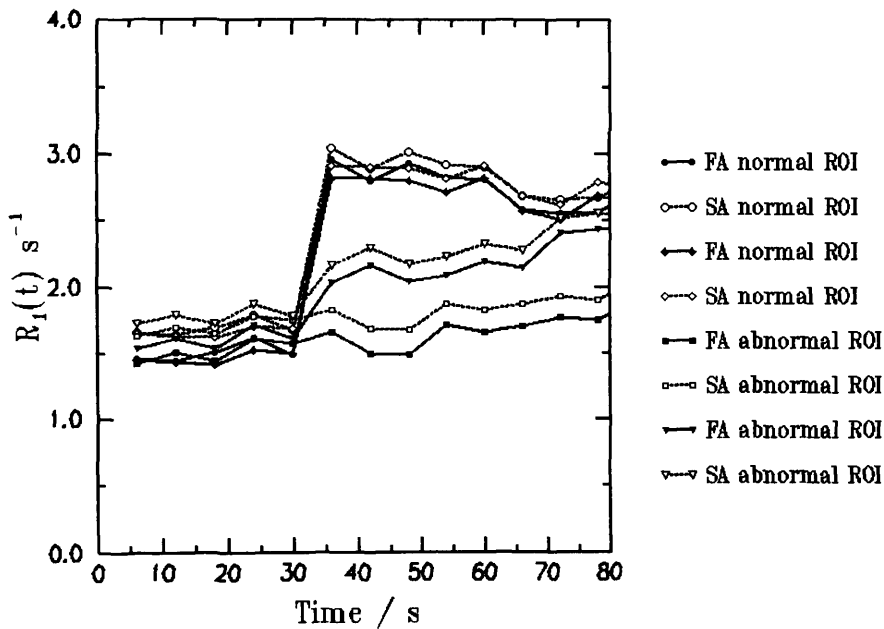


Figure. 4.4 Graph showing the calculated  $R_1$  over time using the simplified analysis of Eq.[A1.9] and the full analysis of Eq.[A1.6] during the introduction of a contrast agent gadobenate dimeglumine (Gd-BOPTA). This is from a patient who had a slow heart rate (60 bpm) whilst dynamic imaging was being undertaken. Four ROI's are shown from the image slice above the papillary muscle. Two ROI's assessed as normal and two assessed as abnormal (reduced)  $^{201}\text{Tl}$  uptake are shown.

Mean $R_1$	Slow heart rate ( $<80\text{bpm}$ )			Fast heart rate ( $\geq 80\text{bpm}$ )		
	Eq. [A1.6]	Eq. [A1.9]	% Diff.	Eq. [A1.6]	Eq. [A1.9]	% Diff.
Normal myocardium	$2.16\text{ s}^{-1}$	$2.32\text{ s}^{-1}$	7.7%	$2.39\text{ s}^{-1}$	$2.67\text{ s}^{-1}$	11.9%
Infarcted myocardium	$2.04\text{ s}^{-1}$	$2.24\text{ s}^{-1}$	9.6%	$1.63\text{ s}^{-1}$	$2.05\text{ s}^{-1}$	25.3%

Table 4.1. Calculated relaxation rates ( $R_1$ ) when using the simplified analysis of Eq.[A1.9], compared to the fuller analysis of Eq.[A1.6]. Results are shown for human myocardium during the arterial injection of Gd-BOPTA.

#### 4.4.1.1 Baseline (pre contrast)

At baseline (pre contrast) the  $R_1$  values obtained using the two methods of analysis were compared to the  $R_1$  values obtained using Eq.[4.1]. When full relaxation is allowed between imaging slices and multiple inversion pulses are used to image the myocardium Eq.[4.1] can be used (MTI method). This does not require a knowledge of the maximum  $T_1$  value in the subject in order to ensure that contrast reversal does not occur. Also, as full relaxation has occurred between imaging slices, the heart rate does not affect the calculation of  $R_1$ . This value of  $R_1$  is compared to that obtained using the two analyses of Eq.[A1.9] and Eq.[A1.6] and is summarised in Table 4.2. The differences in  $R_1$  are shown to be greatest when the simplified analysis of Eq.[A1.9] are used in patients with a fast heart rate. The  $R_1$  values are closest to the values obtained using the MTI imaging when the full analysis is used, as this allows for the signal saturation due to the gating of the images.

	Equation used.	
	Eq.[A1.6]	Eq.[A1.9]
Fast heart rate $\geq 80\text{ bpm}$	34.15%	72.36%
Slow heart rate $< 80\text{ bpm}$	41.26%	66.03%

Table 4.2. Percentage difference in baseline relaxation rates for the simplistic analysis Eq.[A1.9], and fuller analysis Eq.[A1.6] compared to the multiple inversion time relaxation rate calculation. This is shown for patients with fast and slow heart rates.

#### 4.4.1.2 During contrast injection

The  $R_1$  values using the simplified analysis Eq.[A1.9] and full analysis Eq.[A1.6] were compared at first pass peak of the bolus of contrast agent. These were compared for both fast and slow heart rates and in normal and abnormal ROI's and is summarised in Table 4.3.

	Myocardial ROI's.	
	Normal	Infarcted
Fast heart rate $\geq 80$ bpm	6.09%	6.93%
Slow heart rate $< 80$ bpm	4.41%	5.28%

Table 4.3. Percentage difference between relaxation rates at first pass peak for the simplistic analysis Eq.[A1.9], and fuller analysis Eq.[A1.6]. This is shown for patients with fast and slow heart rates.

This shows that when  $R_1$  values are high (e.g. myocardium at first pass peak), the differences between the two methods of analysis are at their minimum, because there is less signal saturation. A greater amount of signal saturation occurs at first pass peak when  $R_1$  values are low as is the case in infarcted myocardium. The differences between the two methods of analysis are at their greatest in abnormal ROI's with a fast heart rate, where signal saturation will have a larger effect on the calculated  $R_1$  value.

#### 4.4.2 The effect of inversion time on the accuracy and precision of snapshot FLASH in measuring $T_1$ *in vivo*.

##### 4.4.2.1 Phantom studies

Figure 4.5 shows the  $R_1$  values obtained in a phantom when the TI is altered in the snapshot FLASH sequence and is compared to the  $R_1$  obtained using a gradient echo sequence. The graph shows that at the low  $R_1$  values ( $R_1 < 1.0 \text{ s}^{-1}$ ) there is a large difference between the  $R_1$  values obtained using the short TI (TI=300ms) and those obtained using the long TI (TI=820ms). The short TI method underestimates the  $R_1$  values due to the effect of contrast reversal. The calculation of  $R_1$  using an inversion recovery sequence assumes that the signal polarity is positive and it is difficult to determine whether this is the case using one inversion pulse. With a longer TI the estimated  $R_1$  is closer to the value obtained using the gradient echo sequence as the assumption that the signal polarity is positive is correct

for all values of  $R_1$  used in the phantom. The mean and standard deviations (SD, [shown as  $2 \times \text{SD}$ ]) on the graph, show that at the low  $R_1$  values, long TI imaging has a high degree of accuracy and precision. However the short TI imaging has a much lower SD, indicating that the measured  $R_1$  has a greater precision even though it is inaccurate.

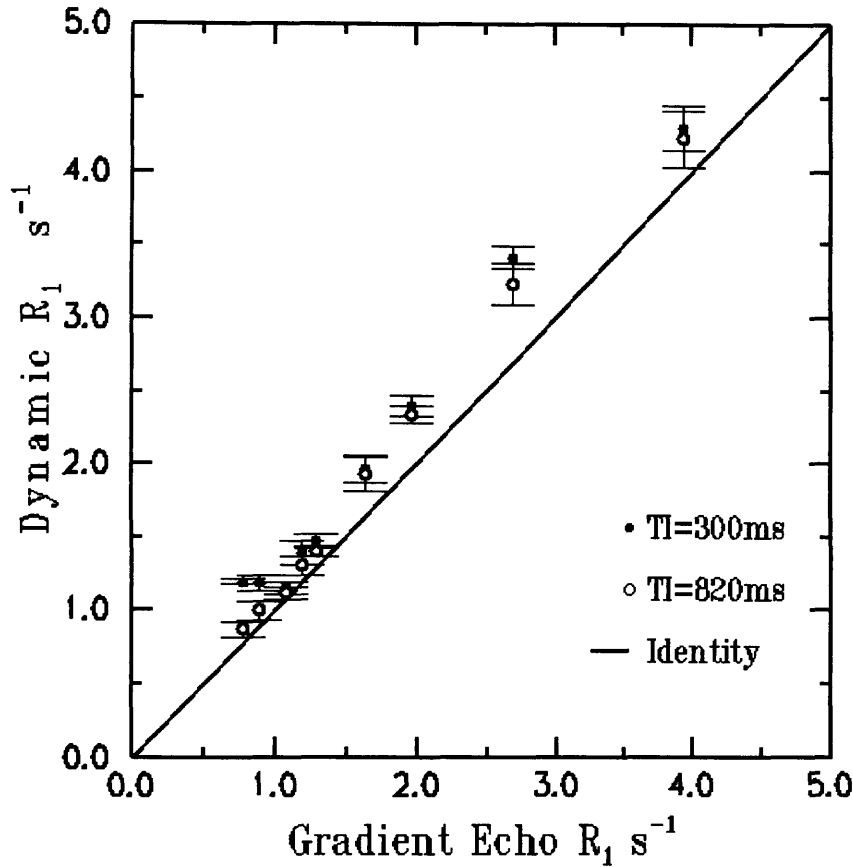


Figure. 4.5 Shows the calculated mean  $R_1$  values in a phantom using ECG gated dynamic snapshot FLASH imaging with two inversion times,  $T_I=300\text{ms}$  and  $T_I=820\text{ms}$ . This is compared to  $R_1$  values obtained using a gradient echo sequence. The standard deviations ( $2 \times \text{SD}$ ) are shown for the dynamic methods, and demonstrate the at the low  $R_1$  values (high  $T_1$  values) there is a large difference in the calculated mean  $R_1$  using  $T_I=300\text{ms}$  compared  $T_I=820\text{ms}$ .

At the higher  $R_1$  values ( $\sim R_1=4.0 \text{ s}^{-1}$ ) both the short and the long TI imaging overestimate the  $R_1$  compared to the gradient echo method. Also the standard deviation is increased, indicating that the precision of  $R_1$  measurement is reduced. This is because the imaging time for the snapshot FLASH sequence is 300ms with the mid line of  $k$ -space acquired at 150ms. Therefore the phantom vial will have fully relaxed before image acquisition is completed and the  $R_1$  value obtained cannot be considered accurate.

#### 4.4.2.2 Volunteer studies

Thirty  $R_1$  values corresponding to 30 ROI's from each of the ten volunteers were obtained for each of the types of imaging: I) Multiple TI images (MTI), and II) Dynamic Imaging TI=300 (short TI), TI=820 (long TI).

Figure 4.6 summarises the  $R_1$  values obtained in a myocardial ROI for the MTI method compared to the  $R_1$  value for the same ROI using dynamic imaging with a long TI and short TI. Unfortunately, data from one volunteer using dynamic imaging with a long TI could not be obtained, so only nine volunteers are shown for this.

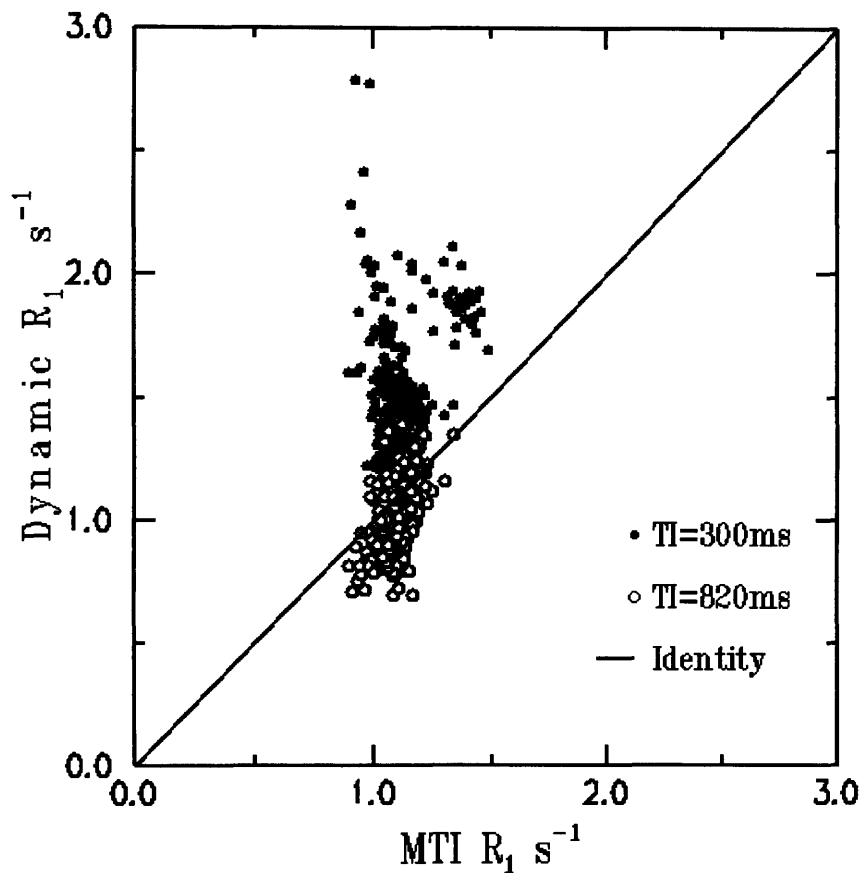


Figure. 4.6 Graph showing the calculated mean  $R_1$  values obtained in volunteers using ECG gated dynamic snapshot FLASH imaging with two inversion times, TI=300ms and TI=820ms. This is compared to  $R_1$  values obtained using ECG gated snapshot FLASH imaging with multiple inversion times and full longitudinal relaxation between inversion pulses (MTI imaging). Each point represents the mean  $R_1$  value for a ROI obtained from 10 dynamic measurements. Ten volunteers with thirty ROI's each are shown.

The MTI imaging is shown to give a narrow range of  $R_1$  values mean  $R_1=1.11\text{s}^{-1}$ , and with a 95% range between  $0.9\text{-}1.32 \text{ s}^{-1}$ . The  $R_1$  values obtained using dynamic imaging with a long TI method were closer to those obtained using the MTI imaging, with a mean

$R_1$  of  $1.01 \text{ s}^{-1}$ , and with a 95% confidence interval range between  $0.74\text{-}1.28 \text{ s}^{-1}$ . The dynamic imaging using a short TI tended to overestimate the  $R_1$ , with a mean of  $1.52 \text{ s}^{-1}$ , and it also gave a greater range of  $R_1$  values  $1.02\text{-}2.02 \text{ s}^{-1}$  with a 95% confidence interval. These results are summarised in table 4.4.

	Relaxation Rate		
	Multiple TI	TI=820ms	TI=300ms
Mean $R_1$	$1.11 \text{ s}^{-1}$	$1.01 \text{ s}^{-1}$	$1.52 \text{ s}^{-1}$
2× Standard Deviation	0.02	0.26	0.49
Upper $R_1$	$0.9 \text{ s}^{-1}$	$0.74 \text{ s}^{-1}$	$1.02 \text{ s}^{-1}$
Lower $R_1$	$1.32 \text{ s}^{-1}$	$1.28 \text{ s}^{-1}$	$2.02 \text{ s}^{-1}$

Table 4.4. Shows the mean and the variability in the calculated longitudinal relaxation rates for three types of imaging.

The *in vivo* myocardial  $R_1$  as determined using the MTI imaging was lower than for dynamic imaging using a short TI. The maximum  $R_1$  to ensure signal polarity is on the correct side of the null point using the short TI is  $R_1=1.33 \text{ s}^{-1}$  ( $T_1=0.75\text{s}$ ). However the mean  $R_1$  using the MTI method was  $R_1=1.11 \text{ s}^{-1}$  ( $T_1=0.9 \text{ s}$ ), which means for  $R_1$  values lower than  $1.33\text{s}^{-1}$ , the short TI would not be able to calculate them accurately as the assumption that the signal polarity is positive would not hold for these values. This is however not a problem for dynamic imaging using the long TI as the minimum  $R_1$  to ensure signal polarity is on the correct side of the null point is  $R_1=0.71 \text{ s}^{-1}$  ( $T_1=1.4 \text{ s}$ ). This value is lower than the upper  $R_1$  range for 95% of the  $R_1$  values obtained using MTI imaging  $R_1=0.9 \text{ s}^{-1}$  ( $T_1=1.11\text{s}$ ).

Figure 4.7 shows a plot of the mean  $R_1$  values for the myocardial ROI's using long, short and multiple TI imaging in one volunteer. The standard deviations (SD, [shown as  $2\times\text{SD}$ ]) for the long and short TI imaging indicate that the precision of the two methods varies. Short TI imaging has a greater imprecision in calculated  $R_1$  values, compared to imaging using a long TI. Both methods of imaging have an increased degree of imprecision in the apex of the heart compared to the ROI's from above and through the papillary muscle. This is summarised in table 4.5.

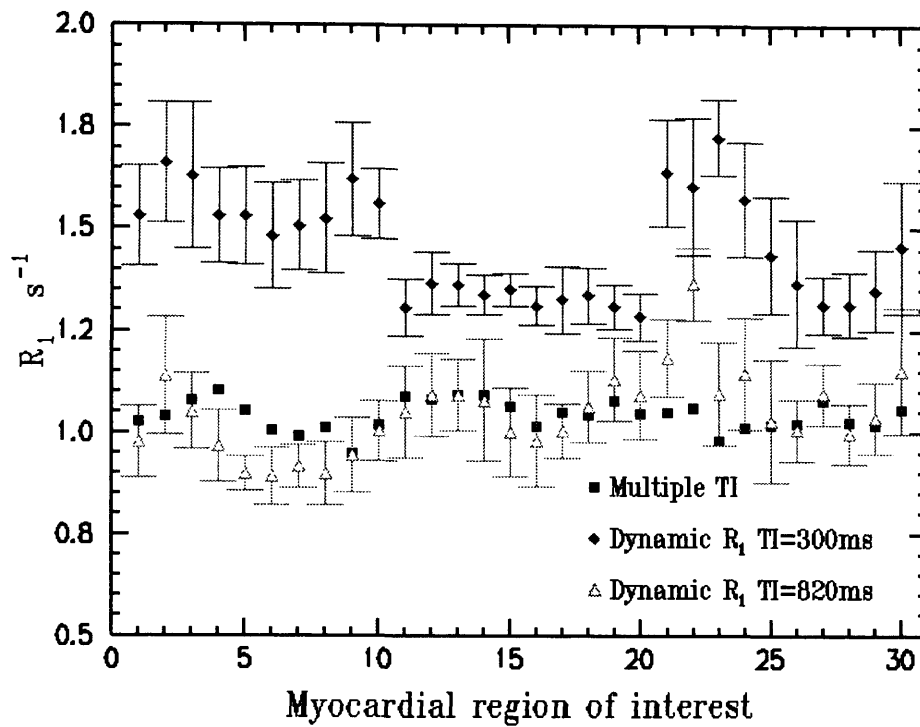


Figure. 4.7 The graph compares the calculated  $R_1$  values obtained in a volunteer using ECG gated dynamic snapshot FLASH imaging with two inversion times, TI=300ms and TI=820ms; and ECG gated snapshot FLASH imaging with multiple inversion times and full longitudinal relaxation between inversion pulses (MTI imaging). This is compared in 30 myocardial ROI's. For the dynamic snapshot FLASH sequence 10 dynamic measurements were obtained. Each point represents the mean and standard deviation ( $2 \times \text{SD}$ ) for the calculated  $R_1$  in a ROI using the full analysis of Eq.[A1.6].

	Relaxation Rate ( $R_1$ )		
	Multiple TI	TI=820ms	TI=300ms
Above papillary muscle	1.02 s <sup>-1</sup> (0.08)	0.97 s <sup>-1</sup> (0.15)	1.56 s <sup>-1</sup> (0.11)
Through papillary muscle	1.06 s <sup>-1</sup> (0.05)	1.05 s <sup>-1</sup> (0.09)	1.33 s <sup>-1</sup> (0.05)
Through the apex	1.03 s <sup>-1</sup> (0.05)	1.11 s <sup>-1</sup> (0.22)	1.47 s <sup>-1</sup> (0.29)
All imaging levels	1.04 s <sup>-1</sup> (0.07)	1.04 s <sup>-1</sup> (0.19)	1.45 s <sup>-1</sup> (0.26)

Table 4.5. Shows the mean calculated  $R_1$  values in one volunteer using three types of imaging for each of the three myocardial levels, and then all three imaging levels. The standard deviations are shown in brackets ( $2 \times \text{SD}$  shown).



#### 4.4.3 The effect of ECG gating MRI scans on the myocardial $T_1$ values

Figure 4.8 show a plot of  $R_1$  values from 30 ROI's per volunteer for the ECG gated snapshot FLASH sequence and 30 ROI  $R_1$  values from the ungated sequence. These values compared to their corresponding  $R_1$  values obtained using MTI imaging in five volunteers.

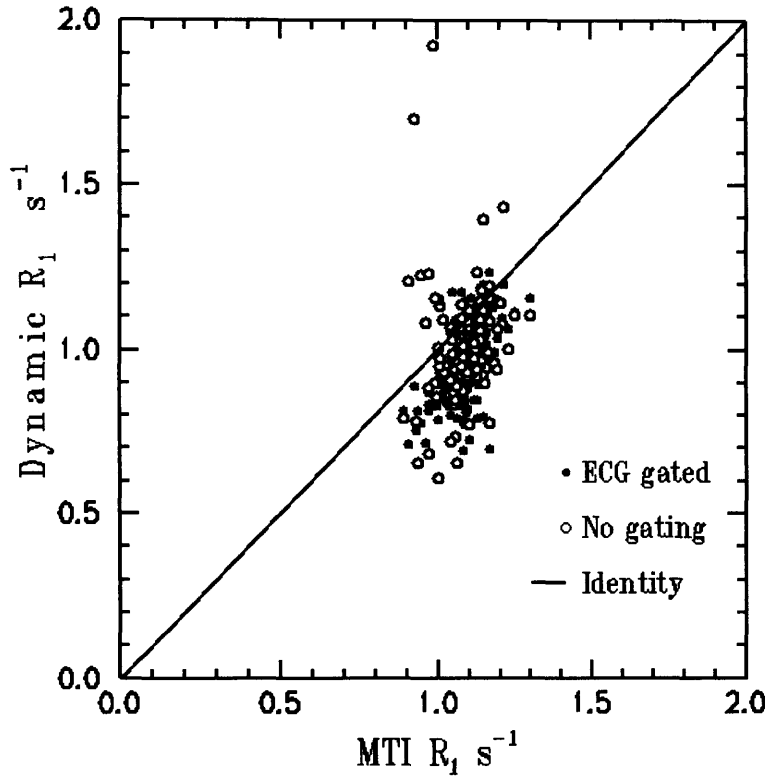


Figure. 4.8 The graph shows the calculated  $R_1$  value obtained during dynamic snapshot FLASH imaging with  $TI=820\text{ms}$ , with and without ECG gating. This is compared to the  $R_1$  values obtained using ECG gated snapshot FLASH imaging with multiple inversion times and full longitudinal relaxation between inversion pulses (MTI imaging). Each point represents the mean  $R_1$  value for a ROI obtained from 10 dynamic measurements. Five volunteers with thirty ROI's each are shown.

The mean  $R_1$  value obtained using both dynamic imaging methods are similar to that obtained using the MTI imaging, although it is slightly underestimated. This is summarised in table 4.6. The main effect of ECG gating on the calculated  $R_1$  values appears to be in the magnitude of the range obtained. At a 95% confidence limit, the effect of not gating the scans results in  $R_1$  values ranging from  $0.69\text{-}1.31 \text{ s}^{-1}$ . However when these ROI's are imaged with ECG gating so the myocardium is in the same cardiac phase, the range of  $R_1$  values is reduced to between  $0.71\text{-}1.22 \text{ s}^{-1}$ .

	Relaxation Rate		
	Multiple TI	ECG gated	No gating
Mean $R_1$	$1.09 \text{ s}^{-1}$	$0.97 \text{ s}^{-1}$	$1.0 \text{ s}^{-1}$
2× Standard Deviation	0.13	0.25	0.31
Upper $R_1$	$1.23 \text{ s}^{-1}$	$1.22 \text{ s}^{-1}$	$1.31 \text{ s}^{-1}$
Lower $R_1$	$0.95 \text{ s}^{-1}$	$0.71 \text{ s}^{-1}$	$0.69 \text{ s}^{-1}$

Table 4.6. Shows the mean and the variability in the calculated relaxation rates, with and without ECG gating. When dynamic imaging with a long TI (TI=820ms) is used. These values can be compared to the  $R_1$  values obtained during ECG gated multiple inversion pulse (Multiple TI) imaging which allows full longitudinal relaxation between inversion pulses.

#### 4.4.4 Myocardial $T_1$ values from normal volunteers

The myocardial  $R_1$  values obtained (using MTI imaging) from all ten volunteers are shown in Figure 4.9. The minimum  $R_1$  was  $0.89 \text{ s}^{-1}$  and the maximum was  $1.48 \text{ s}^{-1}$ . The mean  $R_1$  value was  $1.11 \text{ s}^{-1}$  and with a 95% confidence interval, ranged between 0.91-1.32  $\text{s}^{-1}$ . The  $T_1$  values for the myocardial levels are summarised in table 4.7.

The majority of the  $R_1$  values for nine of the volunteers are around  $R_1=1 \text{ s}^{-1}$  ( $T_1=0.9\text{s}$ ) however, one volunteer has a longer  $R_1\sim 1.3 \text{ s}^{-1}$  ( $T_1\sim 0.75 \text{ s}$ ) for most of the thirty ROI's, which cannot be explained.

The standard deviations (SD, [shown as 2×SD]) for the  $R_1$  values obtained vary depending upon which myocardial level is imaged.  $R_1$  values for images above and through the papillary muscle have SD=0.19 and SD=0.2 respectively. The standard deviation for the  $R_1$  values through the apex was higher SD=0.22. This can be observed in Figure 4.7, as the  $R_1$  values for ROI's 21-30 are more scattered than those for ROI's 1-20. This may be because the apex of the left ventricle may be moving through the imaging plane.

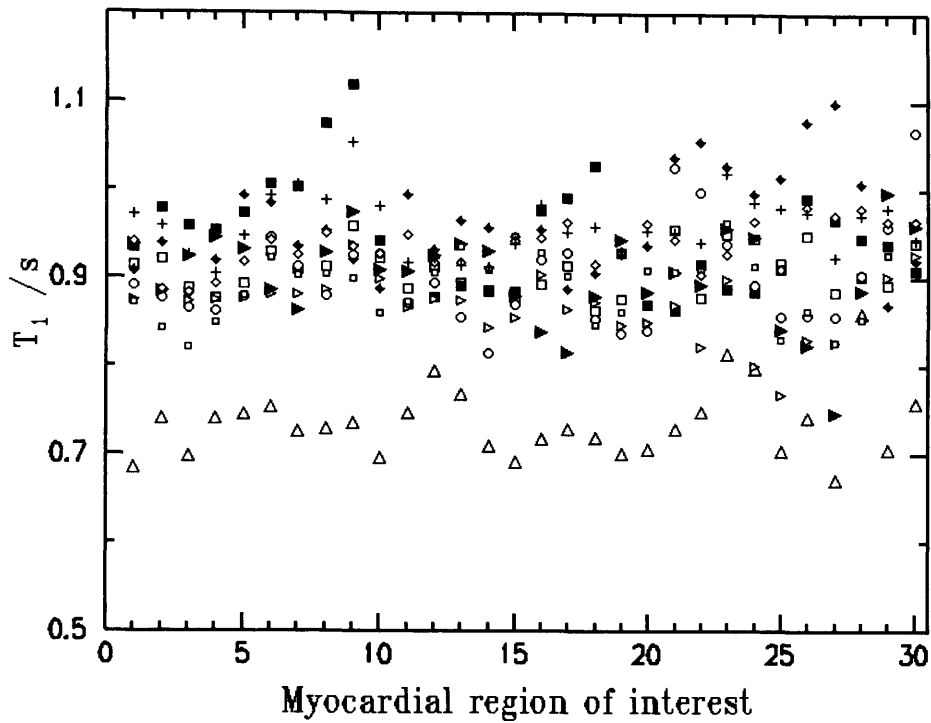


Figure. 4.9 The graph shows the  $R_1$  values obtained in ten volunteers using ECG gated snapshot FLASH imaging with multiple inversion times and full longitudinal relaxation between inversion pulses (MTI imaging). These are shown for thirty ROI's per volunteer. ROI's 1-10 are from the image slice above the papillary muscle, 11-20 are from the image slice through the papillary muscle and 21-30 are from the image slice through the apex. Each point represents the  $R_1$  value from an ROI from a volunteer. The symbols used are different for each volunteer.

	Relaxation rate			
	Above papillary muscle	Through papillary muscle	Through apex of ventricle	All slices
Mean $R_1$	$1.11 \text{ s}^{-1}$	$1.13 \text{ s}^{-1}$	$1.1 \text{ s}^{-1}$	$1.11 \text{ s}^{-1}$
$2 \times$ Standard Deviation	0.2	0.19	0.22	0.2
Upper $R_1$	$1.31 \text{ s}^{-1}$	$1.31 \text{ s}^{-1}$	$1.32 \text{ s}^{-1}$	$1.32 \text{ s}^{-1}$
Lower $R_1$	$0.9 \text{ s}^{-1}$	$0.93 \text{ s}^{-1}$	$0.88 \text{ s}^{-1}$	$0.91 \text{ s}^{-1}$
Minimum $R_1$	$0.89 \text{ s}^{-1}$	$0.97 \text{ s}^{-1}$	$0.9 \text{ s}^{-1}$	$0.89 \text{ s}^{-1}$
Maximum $R_1$	$1.45 \text{ s}^{-1}$	$1.44 \text{ s}^{-1}$	$1.48 \text{ s}^{-1}$	$1.48 \text{ s}^{-1}$

Table 4.7. Shows the  $R_1$  values obtained in ten volunteers using the multiple TI imaging (MTI).

## 4.5 Discussion

The accurate measurement of  $T_1$  *in vivo* has many problems not encountered in phantoms. The phantom  $T_1$  measurements were performed on a system with mono-exponential  $T_1$ . However, *in vivo* there may be multiple  $T_1$  values as tissue water is compartmentalised (Burstein *et al* 1991). The measurement of multi-exponential  $T_1$  relaxation requires that several images are acquired at different points in the  $T_1$  relaxation curve (Crawley *et al* 1988). If this is done with cardiac gating, then several cardiac cycles are needed. For dynamic imaging with good time resolution, this is not practical.

The sub-second image acquisition of the snapshot FLASH sequence enables dynamic imaging studies. Errors may be introduced in  $T_1$  measurement if gating does not allow full longitudinal relaxation ( $>5 \times \text{longest } T_1$ ). The degree of error introduced into the calculated myocardial  $T_1$  due to the reduction in  $TR_0$  is dependant upon the actual  $T_1$  and the heart rate. This is because for a given  $TR_0$  there will be more signal saturation if the  $T_1$  is long than if the  $T_1$  is short. During dynamic contrast injection, the myocardial  $T_1$  is reduced where there is normal blood supply to the effect of the contrast agent. Therefore pre contrast myocardium and myocardium with reduced perfusion where the myocardial  $T_1$ 's are longer will demonstrate a larger difference between the  $T_1$  values from the simplified analysis compared to the fuller analysis.

The greater accuracy and precision of  $T_1$  calculation using a longer inversion time was demonstrated in the results. The inaccuracy and reduced precision of dynamic imaging using a short TI may be due to the effect of contrast reversal when the TI used cannot guarantee that the signal is on the correct side of the null point. Figure 3.7 shows the response of the signal intensity as a function of  $T_1$  for various overall sequence repetition times. The signal response for the short TI imaging is likely to be flat around the null point ( $T_1 \sim 0.75$  s). However, for dynamic imaging using a longer TI there is likely to be a steady response in signal intensity at the myocardial  $T_1$  range which will add to its accuracy and precision. Also this type of imaging allows the input signal from the left ventricle to be acquired simultaneously with the myocardium, enabling perfusion to be assessed using kinetic modelling (Diesberg *et al* 1992, Larrson *et al* 1994). The disadvantage of using a longer TI is that the images have a reduced dynamic signal intensity range and therefore have less contrast. Ultimately, the TI used to image the myocardium is dependant upon whether the images are to be assessed quantitatively or qualitatively.

The use of cardiac gating attempts to image the heart with minimal cardiac motion and to maintain continuity in the myocardial blood volume being imaged. The snapshot FLASH sequence with its subsecond imaging has the effect of “freezing” cardiac motion. The mean myocardial  $T_1$  is unaffected by image gating. However not gating images has shown there is a larger range of  $T_1$  values obtained, indicating that for a single patient there is less accuracy. The advantage of not cardiac gating images is the improvement in temporal resolution. Gated images have a temporal resolution of  $2 \times \text{RR interval}$  ( $\sim 1.5\text{-}2.0\text{s}$ ), on our system ungated images with the longer TI, the temporal resolution is  $\sim 1.0\text{ s}$ . In some instances imaging may catch the heart in the same cardiac phase. As imaging is dynamic, several images are taken over time and this relies on a constant regular heart rate. It has been shown that the greatest effect of error in  $T_1$  calculation is that of overall sequence repetition time. Cardiac patients are not the best candidates for having a constant regular heart rate especially when this is added to the stress of a confined MRI scanner. The imaging of the heart ungated will have the added advantage of having a constant overall sequence repetition time and therefore will reduce the error introduced by this. This is at the cost of constancy in the myocardial blood volume during imaging.

## 4.6 Conclusion

This chapter has investigated the measurement of  $T_1$  *in vivo* using a standard snapshot FLASH sequence on a clinical MRI scanner. The practical *in vivo* technique, and its consequence on the measured  $T_1$  have been investigated.

The overall sequence repetition time, manifest as the heart rate, has the largest effect on the accuracy of myocardial  $T_1$  relaxation times. This impact is greatest at higher values of  $T_1$  as would be found in pre-contrast myocardium, and abnormally perfused myocardial regions.

The initial assumption of the myocardial pre contrast  $T_1$ , and therefore the inversion time used, affects both the accuracy and precision of the calculated  $T_1$ . If the maximum range of  $T_1$ 's to be imaged are underestimated, there will be an increase in the inaccuracy of the calculated  $T_1$  values.

The calculation of myocardial  $T_1$  from normal volunteers can be useful in optimising the imaging sequence parameters. These can be manipulated for either increasing the myocardial contrast for qualitative analysis, or to ensure that quantitative information can be extracted from the images.

In optimising the imaging parameters for quantitative analysis there is a reduction in the myocardial contrast range which needs to be maximised for qualitative analysis. This has implications for perfusion studies of the heart. It will be necessary to decide whether qualitative assessment of images is to be applied, in which case the myocardial image contrast is maximised. If images are to be analysed quantitatively, then there will be a reduction in the image contrast, but the accuracy of  $T_1$  measurements will increased.

## 4.7 References

Andersson T, Ericsson A, Eriksson B, Hemmingsson A, Lindh E, Nyman R, Oberg K. Relative proton density and relaxation times in liver metastases during interferon treatment. *Br J Radiol*, 62:433-437 1989

Bloch P, Lenkinski RE, Buhle EL, Hendrix R, Bryer M, McKenna WG. The use of  $T_2$  distribution to study tumor extent and heterogeneity in head and neck cancer. *Magn. Reson. Imaging*, 9:205-211 1991

Bluml S, Schad LR, Stepanow B, Lorenz WJ. Spin Lattice relaxation time measurement by means of a TurboFLASH technique. *Magn. Reson. Med.* 30, 289-295 1993

Bobman SA, Riederer SJ, Lee JN, Tasciyan T, Farzaneh F, Wang HZ. Pulse sequence extrapolation with MR image synthesis. *Radiology* 159:253-258 1986

Bottomley PA, Hardy CJ, Argersinger RE, Allen-Moore G. A review of  $^1\text{H}$  nuclear magnetic relaxation in pathology: Are  $T_1$  and  $T_2$  diagnostic? *Med phys* 14(1): 1-37 1987

Brix G, Schad LR, Deimling M, Lorenz WJ. Fast and precise  $T_1$  imaging using a TOMROP sequence. *Magn. Reson. Imaging* 8, 351-356 1990

Burstein D, Taratuta E, Manning WJ. Factors in myocardial 'perfusion' imaging with ultrafast MRI and Gd-DTPA administration. *Magn Reson Med*, 20:299-305 1991

Bydder GM, Young IR. MR imaging: Clinical use of the inversion recovery sequence. *J Comput Assist Tomogr* 9:659-675 1985

Carswell H. Functional MR techniques reveal the brain at work. *Diagnostic Imaging International* 28-32 1993.

Crawley AP, Henkelman RM. A comparison of one-shot and recovery methods in  $T_1$  imaging. *Magn. Reson. Med.* 7, 23-34 1988.

Damadian R. Tumor detection by nuclear magnetic resonance. *Science* 171: 1151-1153 1971

Deans HE, Smith FW, Lloyd DJ, Law AN, Sutherland HW. Fetal fat measurement by magnetic resonance imaging. *Br J Radiol*, 62: 603-607 1989

Deichmann R, Haase A. Quantification of  $T_1$  values by SNAPSHOT-FLASH NMR imaging. *J. Magn. Reson.* 96, 608-612 1992

Dickinson RJ, Hall AS, Hind AJ, Young IR. Measurement changes in tissue temperature using MR imaging. *J Comput Assist Tomogr*, 10:468-472 1986

Diesbourg LD, Prato FS, Wisenberg G, Drost DJ, Carrol SE, O'Neil B. Quantification of myocardial blood flow and extracellular volumes using a bolus injection of Gd-DTPA: Kinetic modelling in canine ischaemic disease. *Magn. Reson. Med.* 23, 229-253 1992

Gowland PA, Leach MO. Fast and accurate measurements of  $T_1$  using a multi-readout single inversion recovery. *Magn. Reson. Med.* 26, 79-88 1992

Graumann R, Barfuß H, Hentschel D, Oppelt A. TOMROP: a sequence for determining the longitudinal relaxation time  $T_1$  in magnetic resonance imaging. *Electromedica* 55, 67-72 1987

Graumann R, Deimling M, Heilmann T, Oppelt A. A new method for fast and precise  $T_1$  determination. Abstracts of the Society of Magnetic Resonance in Medicine, 4th Annual Meeting, p. 922, 1986.

Haase A. Snapshot FLASH MRI. Applications to  $T_1$ ,  $T_2$ , and chemical-shift imaging. *Magn. Reson. Med.* 13, 77-89 1990

Hall AS, Prior MV, Hand JW, Young IR. Observation by MR imaging of *in vivo* temperature changes induced by radio frequency hyperthermia. *J Comput Assist Tomogr*, 14:430-436 1990



Johnson G, Ormerod IE, Barnes D, Tofts PS, McManus D. Accuracy and precision in the measurement of relaxation times from nuclear magnetic resonance images. *Br. J. Radiol.* 60, 142-153 1987

Kay I, Henkelman RM. Practical implementation and optimisation of one-shot  $T_1$  imaging. *Magn. Reson. Imaging* 22, 414-424 1991

Kingsley PB, Ogg RJ, Steen RG. Phantom validation does not ensure accurate  $T_1$  measurements *in vivo*. *Book of Abstracts: Proceedings of the International Society for Magnetic Resonance in Medicine*, p 2066, 1997

Larsson HBW, Stubgaard M, Sondergaard L, Henriksen O. *In vivo* quantification of the unidirectional influx constant for Gd-DTPA diffusion across the myocardial capillaries with MR imaging. *Magn. Reson. Med.* 4, 433-440 1994

Look DC, Locker DR. Time saving in measurement of NMR and EPR relaxation times. *Rev. Sci. Instrum.* 41, 250-251 1970

Masterson ME, McGary R, Schmitt K, Koucher JA. Accuracy and reproducibility of image derived relaxation times on a clinical 1.5T magnetic resonance scanner. *Med. Phys.* 16, 225-233 1989

Parker DL, Smith V, Sheldon P, Crookes LE, Fussell L. Temperature distribution measurements in two-dimensional NMR imaging. *Med Phys*, 10:321-325 1983

Perman W.H., Hilal S.K., Simon H.E., Maudsley A.A. Contrast manipulation in NMR imaging. *Magn. Reson. Imaging* 2:23-32 1984.

Tofts PS, DuBoulay EP. Towards quantitative measurements of relaxation times and other parameters in the brain. *Neuroradiology* 32:407-415 1990

Warach S, Gaa J, Siewert B, Weipolski P, Edelman RR. Acute human stroke studied by whole brain echo planar diffusion-weighted magnetic resonance imaging. *Ann. Neurol.* 37:231-241 1995.

Warach S, Chein D, Li W, Ronthal M, Edelman RR. Fast magnetic resonance diffusion-weighted imaging of acute human stroke. *Neurology* 42:1717-1723 1992.

Welch KMA, Windham J, Knight RA, *et al.* A model to predict the histopathology of human stroke using diffusion and  $T_2$  weighted magnetic resonance imaging. *Stroke* 26(11):1983-1989 1995.

Young IR, Bailes DR, Bydder GM. Apparent changes of appearance of inversion recovery images. *Magn Reson Med*, 2:81-85 1985

Zhang YT, Yeung HN, Carson PL, Ellis JH. Experimental analysis of  $T_1$  imaging with a single scan, multi-point, inversion recovery technique. *Magn. Reson. Med.* 25, 337-343 1992

## **Chapter 5: Clinical application of the unidirectional influx constant ( $K_i$ ) as a method of quantitatively assessing myocardial perfusion *in vivo*.**

### **5.1 Introduction**

The development of fast imaging techniques within MR imaging has enabled the imaging of the myocardium. These have provided structural (Maddahi *et al* 1987, Higgins *et al* 1985), and functional (Caputo *et al* 1990, Cranney *et al* 1990) information, and the use of MR spectroscopy has enabled biochemical (Schaefer *et al* 1989) information to be extracted. Subsecond imaging has enabled tracking of a bolus of contrast agent through the myocardium. Studies have been conducted to attempt to extract regional perfusion data from an MR examination either qualitatively (Miller *et al* 1989, Atkinson *et al* 1990, Manning *et al* 1991, Eichenberger *et al* 1995) or semi-quantitatively (Hittmair *et al* 1994). MR imaging has the obvious advantages that it is relatively non invasive and there is no ionising radiation, so the examination is repeatable.

The development of cardiac drugs such as thrombolytic therapies (Pearlman *et al* 1995), or new treatment regimes such as transmyocardial laser revascularisation (Mirrhoseini *et al* 1988), calls for tools which will enable their clinical effect to be monitored. To extract quantitative perfusion information, a model that relates the MR signal intensity changes during the injection of a bolus of contrast agent to tissue perfusion is needed.

There are several methods which attempt to apply first pass contrast enhanced MR imaging to the evaluation of myocardial perfusion. Wilke *et al.* (1993) have attempted to measure myocardial perfusion by assessing the inverse of the mean transit time. The mean transit time is the ratio of a tissue's volume to its flow, and was calculated from the signal intensity time curve. A linear correlation was found between the inverse mean transit time

and radiolabelled microsphere measurements of absolute myocardial blood flow in dogs, using intra atrial injections of Gd-DTPA ( $0.05\text{mol kg}^{-1}$ ).

Diesbourg *et al.* (1992) used the modified Kety equation (Kety 1951) and applied it to model the variation of Gd-DTPA concentration with time, taking into account the extravascular movement of this contrast agent. They obtained the product of local blood flow (perfusion) and the extravascular movement of the contrast agent (extraction fraction). An estimate of the extracellular volume fraction was also obtained.

Gd-DTPA is an extracellular contrast agent in tissues where the cell membrane integrity is maintained i.e. normal tissue (Prato *et al* 1988, Diesbourg *et al* 1992, Tong *et al* 1993 [II]) and ischaemic but not infarcted tissue (Diesbourg *et al* 1992). However, in infarcted tissue where the cell membrane integrity is lost (Beanlands *et al* 1990), Gd-DTPA is able to enter the cells. Here Gd-DTPA is no longer limited to the extracellular space and so an estimate of the extracellular volume will be increased (Tong *et al* 1993 [I], Pereira *et al* 1996). For both normal and reperfused tissue, myocardial perfusion estimates would be expected to be within normal ranges [ $95 \pm 9\text{ml}/100\text{g}/\text{min}$  (Ilida *et al* 1988)] whereas in ischaemic or infarcted tissue, a reduction in perfusion would be expected (Diesbourg *et al* 1992). In this way it may be possible to distinguish tissue states by measuring both perfusion and extracellular volume.

In applying the modified Kety model to myocardial perfusion measurements, the parameters which describe the movement of the contrast agent out of the vascular space (extraction fraction) have to be determined. Also the equilibrium distribution of the contrast agent, i.e. the concentration in the myocardium divided by the concentration in the blood (partition coefficient) (Tong *et al* 1993 [I,II]) is required for specific contrast agents.

When measuring myocardial perfusion with extracellular contrast agents e.g. Gd-DTPA, the first pass kinetics are complicated, as they are determined by blood flow, intra and extravascular distribution as well as permeability across the capillary wall. Burstein *et al* (Burstein *et al* 1991) have shown that image intensity with Gd-DTPA in an isolated perfused heart, is affected by the delivery of the contrast agent to the extravascular extracellular space (interstitial space). This is dependant upon the coronary flow rate and the diffusion of the contrast agent to extravascular extracellular space. The image intensity is also affected by the relaxation properties of the tissue. This is dependant upon the concentration of the contrast agent, proton exchange rate and relative extracellular and intracellular volume fractions (Burstein *et al* 1991).

Several methods have been proposed which attempt to model the kinetics of Gd-DTPA during dynamic imaging to characterise abnormal capillary leakage (Tofts *et al* 1991, Larsson *et al* 1994, Brix *et al* 1990,1991). Larsson *et al* (1994) propose a method for the in vivo quantification of a unidirectional transfer constant ( $K_i$ ) in ml/100g/min. This describes the transfer of a tracer such as Gd-DTPA between the extracellular extravascular space and the plasma.  $K_i$  is the product of the extraction fraction (E), and perfusion (F), and requires the independent measurement of the extraction fraction in order to determine perfusion. This method also calculates  $\lambda$ , the partition coefficient (ml/g) which is equivalent to the myocardial distribution volume (Tong *et al* 1993 [II]). In normal myocardium when using extracellular contrast agent,  $\lambda$  is related to the anatomical extracellular volume. But for infarcted tissue, extracellular contrast agents can penetrate the myocytes so  $\lambda$  is physiologically described as the distribution volume (Tong *et al* 1993 [II]).

Larsson's model (Larsson *et al* 1994) requires that the concentration of the tracer can be monitored in both the arterial system (input function) and its uptake in the tissue (myocardium) over time (response function). There is a non linear relationship between increases in image intensity and myocardial gadolinium concentration beyond a dose of 0.05mmol/kg body weight (Wedeking *et al* 1992). In order to relate signal intensity to tracer concentration,  $R_1$  ( $=1/T_1$ ) is used as this has a linear relationship with Gd-DTPA concentration (Strich *et al* 1985, Koenig *et al* 1986, Burstein *et al* 1991).

The signal enhancement seen due to the presence of the contrast agent is dependant upon the effect the contrast agent has on the tissue water magnetisation (Donahue *et al* 1994). The contrast agent relaxes the tissue water and therefore reduces its  $T_1$ , and increases its signal intensity (Gadian *et al* 1985) in a  $T_1$  weighted imaging sequence. However, as the tissue is compartmentalised, only some compartments will contain the contrast agent. The exchange of the water molecules between these compartments will alter the magnetisation of water molecules in compartments not containing the contrast agent. If the proton exchange is fast (as between the intracellular and extracellular space), then the tissue will relax with one time constant. However if the exchange is slow to intermediate (as between the extravascular and intravascular space), then the tissue may relax with multiple time constants, and the measured time constant will depend upon the imaging parameters (Donahue *et al* 1995). Also, the differences between compartmental relaxation

rates are dependant upon contrast agent concentration. Therefore there may be differences in proton exchange as the concentration of the contrast agent varies, as happens during a bolus injection (Donahue *et al* 1997).

## 5.2 Aims

The aim of this study was to apply the simple model proposed by Larsson *et al* (1994) clinically, and to obtain myocardial  $K_i$  and distribution volume  $\lambda$ , values from patients after an acute myocardial infarction.

## 5.3 Method

Experiments were performed using a whole body MRI system (MAGNETOM IMPACT, Siemens, Erlangen, Germany) operating at 1.0 Tesla. A linearly polarised body coil was used for R.F. transmission and reception of the NMR signal. The system was equipped with actively shielded magnetic field gradient coils, giving gradient strengths of up to  $15\text{mT m}^{-1}$  with rise times of 1ms.

After obtaining ethics committee approval, thirty patients admitted to our hospital with acute myocardial infarction had an MRI scan within 2-4 days of this ischaemic event. These patients were also assessed using  $^{201}\text{thallium}$  single photon emission computed tomography (SPECT).

### 5.3.1 MR imaging

A snapshot FLASH sequence was used to measure *in vivo* myocardial  $T_1$ . Short axis images through the left ventricle were obtained, with three slices positioned above, through and below the papillary muscle. All image acquisition was cardiac gated so that the midline of  $k$ -space was acquired in systole, and the heart rate of each patient was recorded. On each image, the left ventricular myocardium was divided radially and evenly into ten regions of interest (ROI's) (Figure 4.1), and the  $R_1 (=1/T_1)$  was found for each ROI.

First, baseline (pre contrast)  $R_1$  measurements of the left ventricle were obtained using a snapshot FLASH sequence. The imaging parameters were  $\alpha=8^\circ$ ;  $\text{TR}=4.7\text{ms}$ ;  $\text{TE}=2\text{ms}$ ;  $\text{FOV}=250\text{ms}$ ;  $64\times 64$  data matrix; 10mm thick slices.  $R_1$  was calculated as described in section 4.3.1.1.

After acquiring an  $M_0$  image for each slice, the heart was then imaged continuously during the bolus injection of  $0.05 \text{ mol kg}^{-1}$  gadobenate dimeglumine (Gd-BOPTA) contrast agent (Bracco SpA, Milan, Italy). Twenty measurements, of the three image slices were acquired at the rate of one image every two heart beats. The time interval between each of the snapshot FLASH images was recorded. The inversion time for the sequence was 300ms and all the other parameters were the same as above.  $R_1$  was then calculated using the full analysis Eq.[A1.6] for each ROI during the dynamic injection of the contrast agent. In addition, an ROI was placed in the left ventricle of each slice, and the signal was used to calculate  $R_1$  for the input function.

For each patient  $K_i$  and  $\lambda$  was calculated for the ROIs, using a programme written by Dr M.A. Horsfield, Department of Medical Physics, University of Leicester. This programme follows the method of Larsson *et al.* (1994). From the plots of  $R_1$  vs. time, both the input function (arterial concentration of the contrast agent) and the tissue response (myocardial concentration of contrast agent) in each region of interest are calculated. The tissue response is the convolution of the input function with the  $\delta$ -function response. This is the term,

$$K_i e^{-\frac{K_i}{\lambda}}, \quad [5.1]$$

thus  $K_i$  and  $\lambda$  can be deduced.

In order to estimate the tissue concentration of contrast agent, the pre contrast tissue  $R_1$  must be accurately known. The major problem faced is ensuring that the inversion pulse applied is long enough to be certain the signal is on the correct side of the null point, when using the dynamic snapshot FLASH sequence. If the inversion pulse is very long relative to the pre contrast tissue  $T_1$ , then this increases imaging time. It also has the effect of reducing the image contrast. Pre contrast values of  $R_1$  were measured in the myocardium using the multiple TI method, as this was more accurate. The literature value of  $R_1 = 0.833 \text{ s}^{-1}$  for pre contrast blood was used (Bottomley *et al* 1984). A value of  $\rho = 5.1 \text{ L mmol}^{-1} \text{ s}^{-1}$  (Cavagna *et al* 1994) was used for the relaxivity of the contrast agent. The actual value of contrast agent relaxivity is not important for  $K_i$  measurement. However, it is important that the relaxivity is constant for blood and myocardium, both normal and infarcted (Tofts *et al.* 1997).

### 5.3.2 Single photon emission computed tomography (SPECT)

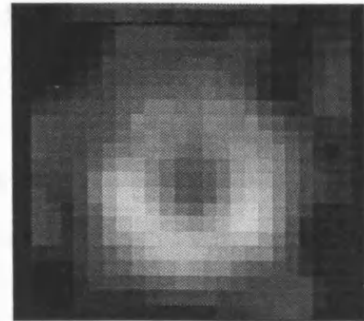
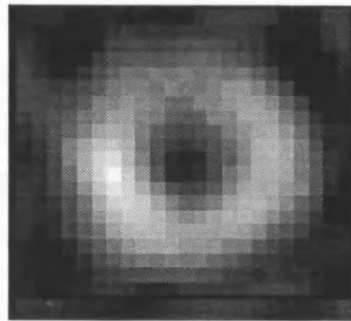
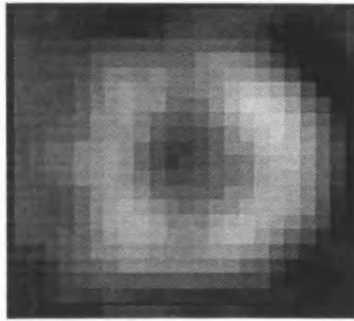
Within 24 hours of the MRI scan, patients received a resting  $^{201}\text{Tl}$  SPECT scan. Scintigrams were obtained using a Siemens Diacam camera. Scans were performed with the patients in a resting state after 80 MBq of  $^{201}\text{Tl}$  was administered intravenously. Data was acquired in a 180° rotation from 45° right anterior oblique to 45° left posterior oblique. Acquisition consisted of 32 projections each for 40 seconds. The projections were corrected for field nonuniformity and using the filtered back projection technique, transverse tomograms were reconstructed. The data acquired was then assessed on the same slice and ROI basis as the MRI scans. This is summarised in Figure 5.1. The assessment was undertaken in two ways: qualitatively and semi quantitatively.

The semi quantitative assessment used was the Sirner method (Stirner *et al* 1986) as supplied by the manufacturers (Siemens Medical Systems Inc. Erlangen, Germany 1994). This method enables the counts in an ROI to be normalised, and so enable comparisons between patients. In principle, the maximum counts in a region of interest are assumed to represent a normal region of myocardium. Each ROI has an expected minimum percentage of the maximum counts in order for it to be considered as having normal perfusion. This method allows for the reduced number of counts in areas such as the anterior wall due to attenuation from the chest wall. But, the limitation is that not all patients are the same build. Additionally, if a patient has triple vessel disease, then ROI's cannot be normalised as normal perfusion cannot be assumed. Using this method a  $^{201}\text{Tl}$  score was obtained for each ROI for each of the patients.

For the qualitative assessment, each ROI was scored from zero to three by a Consultant Radiologist. Zero corresponded to normal uptake, and three corresponded to reduced uptake of the  $^{201}\text{Tl}$ .



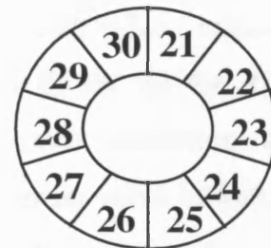
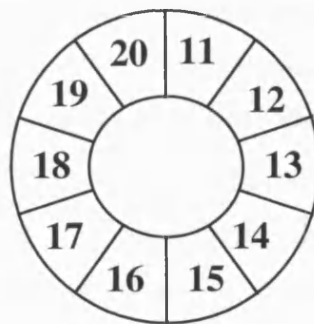
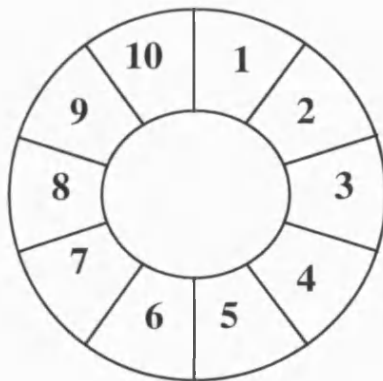
## Thallium images



Above the papillary muscle

Through the papillary muscle

Through the apex

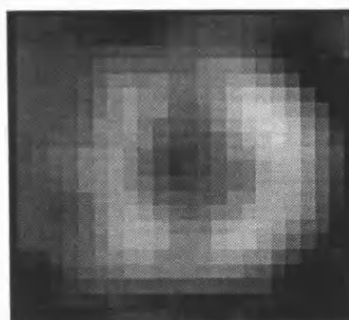


## Anatomical areas

Anterior

Septal

Lateral



Posterior/Inferior

Figure 5.1 shows three reconstructed transverse tomograms through the left ventricle. These images correspond to the three slices taken using MRI. Each image is equally divided into ten regions of interest ROIs, and these were used for the assessment of the myocardium and comparison with MRI.

## 5.4 Results

The quality of the data obtained from the patients varied to a large degree. This is shown in figure 5.2. Patient 1, has a clear signal from the ventricle after the injection of the contrast agent and there is a clear uptake of contrast agent in the myocardial regions of interest, reflected in the increased signal. This data together with the signal intensities from the  $M_0$  image (not shown) are used to calculate  $R_1$ , which can then be used to calculate the  $K_i$  and distribution volume ( $\lambda$ ), from Larsson's model. The values are very different between patients when the quality of the raw data is poor. Patient 2, has poor delivery of the bolus to the left ventricle as can be seen with the slow increase in the signal intensity, and so there is a resultant poor increase in the signal intensity in the myocardial ROI's. The resultant  $K_i$  values are much higher than those obtained by Larsson *et al* (1994).

The mean of the  $K_i$  values for the thirty patients are shown in Figure 5.3. The figure shows that there is a wide variation of values between patients. Standard deviations were not used as, there a wide distribution of data, and so showed negative  $K_i$  values, which is not possible. Instead, median values have been used. The mean  $K_i$  for all the ROIs  $K_i=116.32$  ml/min/100g, median=114.9 ml/min/100g, with a mean maximum and minimum of 199.95 and 41.47 ml/min/100g respectively. For  $\lambda$ , a mean value of  $\lambda=8.27$  ml/100g, was obtained. These  $K_i$  values are higher,  $K_i=54$ ml/min/100g, and  $\lambda$  values are lower  $\lambda=30$ ml/100g than those obtained in healthy volunteers (Larsson *et al* 1996).

The ROIs were divided into two groups, those with normal uptake of  $^{201}$ thallium and those with reduced uptake. This was done for both the semi quantitative method of assessment, and the qualitative method of assessment. The results for  $K_i$  and  $\lambda$  are shown in tables 5.1 and 5.2. below.

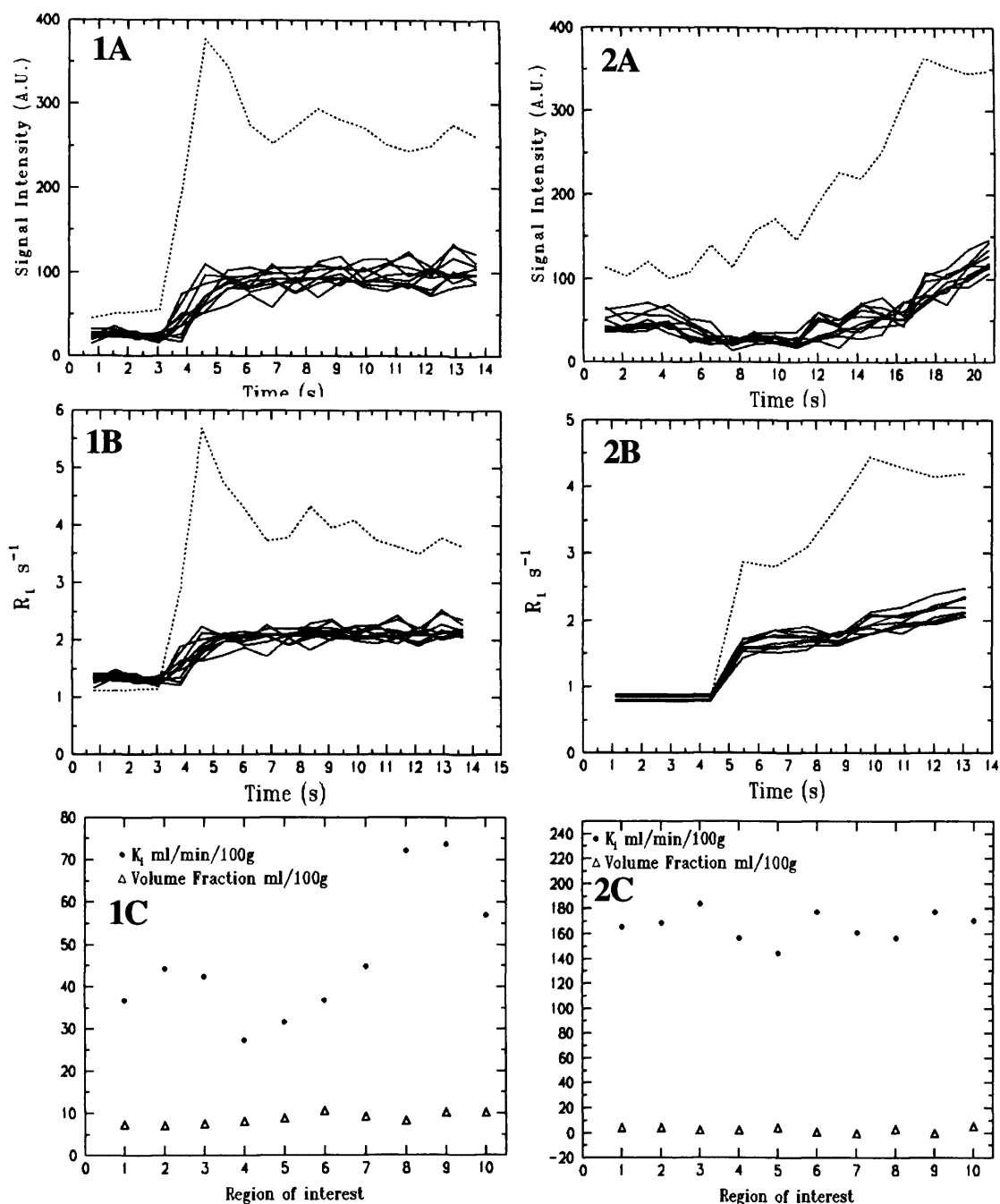


Figure 5.2 Shows the raw signal intensity data (A) and the calculated  $R_1$  values (B) which are then used to calculate the  $K_1$  (C). This is shown for two patients, Patient 1, with good quality raw data, and Patient 2, with poor quality raw data. They are shown for 10 ROI's (1-10) above the papillary muscle, shown as solid lines. The corresponding information from the input function (left ventricle) is shown with dashed lines. In graph 1A, there is a sharp rise in signal intensity when the contrast agent is introduced. In contrast, in graph 2A, there is a poor rise in signal intensity with contrast agent introduction. The pre contrast myocardial  $R_1$  values in graph 2B are replaced by those measured using the more accurate MTI method and so appear to be more stable. These were replaced for all patients. There is a wide difference in the calculated  $K_1$  values obtained from these two patients, because the quality of the raw data is so varied.

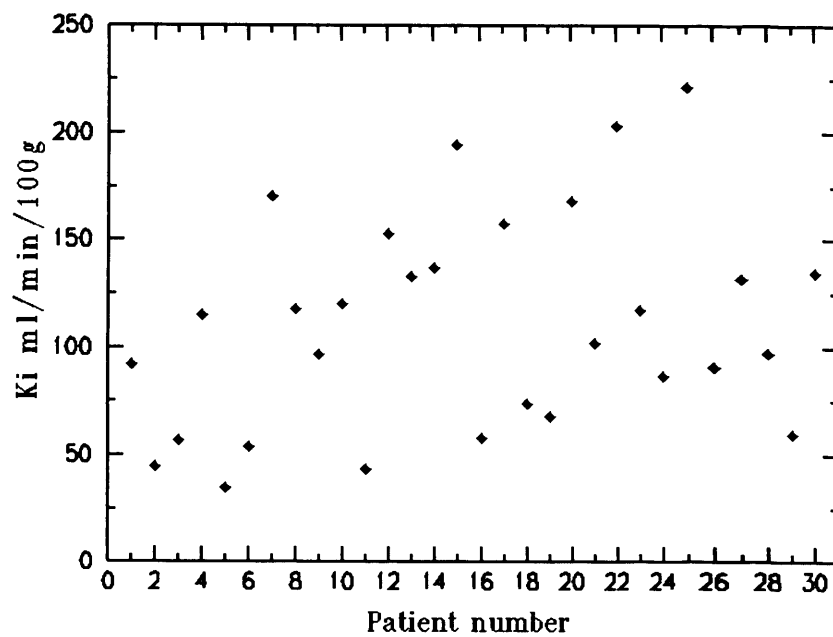


Figure 5.3 The mean  $K_i$  obtained from thirty regions of interest are shown for the thirty patients in the study. The figure shows that the mean value for  $K_i$  varies widely between patients.

	$K_i$ -Semi quantitative $^{201}\text{thallium}$ assessment		$K_i$ -Qualitative $^{201}\text{thallium}$ assessment	
	Normal Uptake	Reduced Uptake	Normal Uptake	Reduced Uptake
Mean ml/min/100g	110.7	124.62	124.73	109.95
SD	136.31	133.89	137.63	133.39

Table 5.1 The mean and SD values for  $K_i$  in all thirty patients. The ROIs are divided into those with normal and reduced  $^{201}\text{thallium}$  uptake as assessed semi quantitatively, and qualitatively.

	$\lambda$ -Semi quantitative $^{201}\text{thallium}$ assessment		$\lambda$ -Qualitative $^{201}\text{thallium}$ assessment	
	Normal Uptake	Reduced Uptake	Normal Uptake	Reduced Uptake
Mean ml/100g	7.87	8.88	7.98	8.5
SD	6.52	11.98	5.93	11.0

Table 5.2 The mean and SD values for  $\lambda$  in ROIs divided into normal and reduced  $^{201}\text{thallium}$  uptake. These ROIs were assessed semi quantitatively and qualitatively in all thirty patients.

As can be seen from the tables, similar mean values for  $K_i$  and  $\lambda$  are obtained for both methods of  $^{201}\text{thallium}$  assessment. For the semi quantitative assessment, a slightly lower  $K_i$  value is obtained for myocardium with normal  $^{201}\text{thallium}$  uptake, compared to the qualitative assessment. Also unexpectedly, the mean  $K_i$  increases from ROIs with normal compared to those with reduced  $^{201}\text{thallium}$  uptake.

Mean values for  $\lambda$  show a slight increase between normal and reduced  $^{201}\text{thallium}$  uptake in ROIs for both methods of assessment, and as the standard deviations reflect, there is a large variation in the  $\lambda$  values obtained.

To assess if there is a relationship between  $K_i$ ,  $\lambda$  and  $^{201}\text{thallium}$  uptake correlation coefficients were obtained. Spearmans correlation coefficient was applied where all the ROIs were ranked. The results are shown below in table 5.3.

	$K_i$		$\lambda$	
	Correlation coefficient	$p$ -value	Correlation coefficient	$p$ -value
Semi quantitative $^{201}\text{thallium}$ assessment	0.183	<0.0001	0.116	0.002
Qualitative $^{201}\text{thallium}$ assessment	-0.170	<0.0001	0.039	0.995

Table 5.3 shows the relationship between  $K_i$ ,  $\lambda$  and the  $^{201}\text{thallium}$  assessment of ROIs. The closeness of the relationship is reflected in the correlation coefficients and their significance in  $p$ -values. There is a very poor correlation between these variables. The qualitative assessment shows a negative correlation because the  $^{201}\text{thallium}$  score is increased in regions where  $^{201}\text{thallium}$  uptake is reduced.

The results in table 5.3 show that for all the ROIs there is a very poor correlation between  $K_i$ , and  $^{201}\text{thallium}$  assessment, although it is highly significant. For  $\lambda$  and  $^{201}\text{thallium}$ , there is no relationship, as the correlation coefficient is very low, and the  $p$ -value is high for the qualitative method of  $^{201}\text{thallium}$  assessment.

The relationship between  $K_i$  and  $^{201}\text{thallium}$  uptake was further assessed to ascertain if the relationship varies in different anatomical areas of the myocardium. The ROIs were anatomically grouped as according to the regions shown in table 5.4.

This grouping is also shown diagrammatically in Figure 5.4 below.

Imaging level	Anatomical area	Regions of interest
Above the papillary muscle	Anterior	1,2,10
	Lateral	3,4
	Posterior	5,6
	Septal	7,8,9
Through the papillary muscle	Anterior	11,12,20
	Lateral	13,14
	Posterior	15,16
	Septal	17,18,19
Through the apex	Anterior	21,30
	Lateral	22,23
	Inferior	24,25
	Posterior	26
	Septal	27,28,29

Table 5.4 shows the grouping of ROIs according to the anatomical areas of the myocardium they represent.

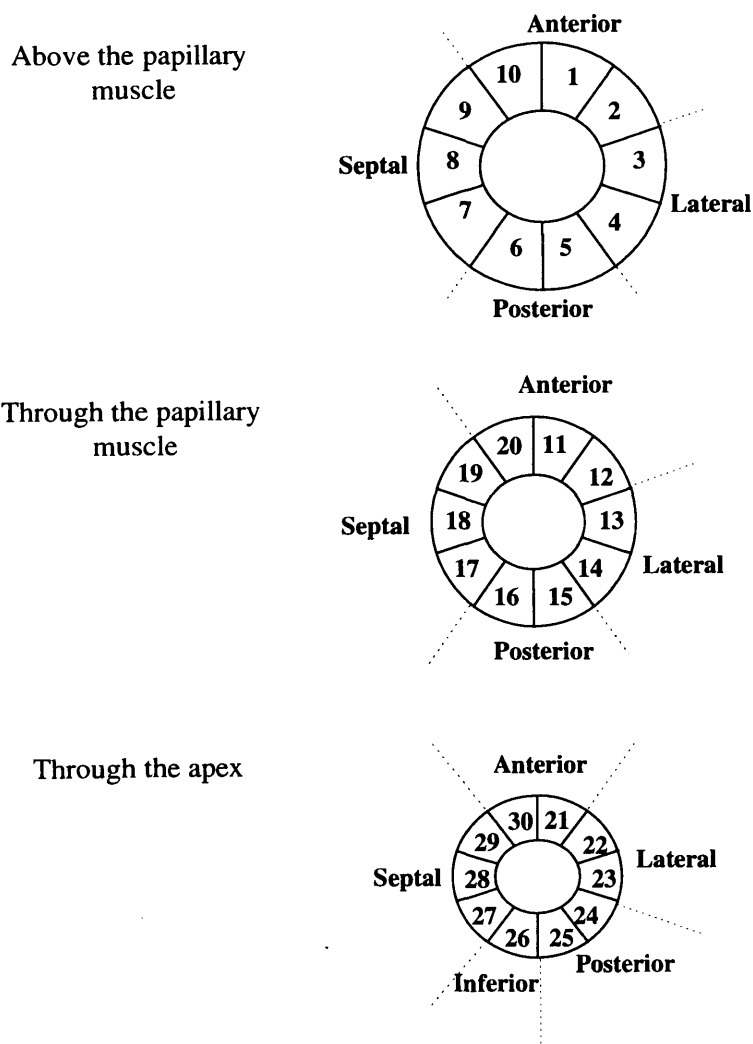


Figure 5.4. Shows the anatomical areas represented by the ROI's at each of the imaging levels.

The correlation coefficients were calculated between  $K_i$  and  $^{201}\text{thallium}$  for each anatomical area. The results are shown in Figure 5.5. There is shown a wide range of correlation coefficients obtained in the different anatomical areas for both methods of  $^{201}\text{thallium}$  assessment. There is a negative correlation between qualitative  $^{201}\text{thallium}$  assessment and  $K_i$  since areas of reduced  $^{201}\text{thallium}$  uptake have a higher score than those with an increased uptake. The mean correlation coefficient for the semi quantitative assessment was 0.165 (SD=0.247), and for the qualitative assessment was -0.159 (SD=0.197). Although overall there is a poor correlation between  $K_i$  and  $^{201}\text{thallium}$ , this appears to improve for some anatomical areas namely the anterior, septal and lateral.

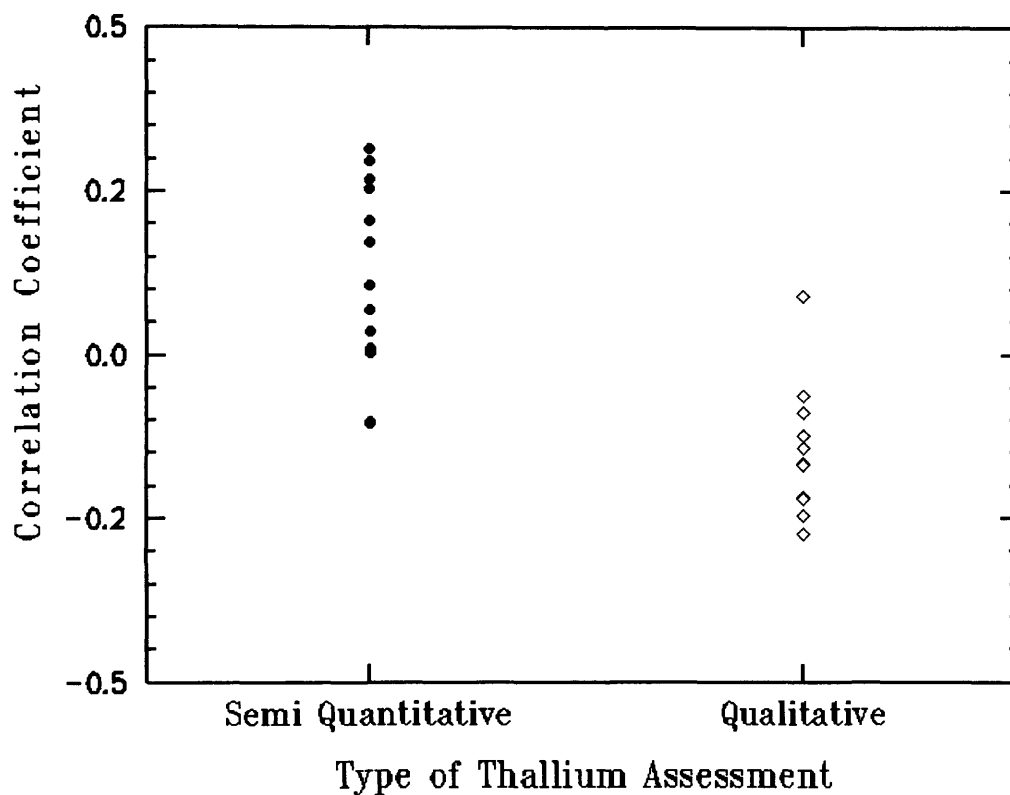


Figure 5.5 This figure shows the correlation coefficient obtained for  $K_i$  and  $^{201}\text{thallium}$  scintigraphy. These are shown for thirteen anatomical areas of the myocardium. Two methods of  $^{201}\text{thallium}$  assessment were used for the anatomical areas, qualitative and semi quantitative. There is an overall negative correlation between  $K_i$  and semi quantitative assessment as zero corresponded to normal  $^{201}\text{thallium}$  uptake, and scoring increased as there was a reduction in the  $^{201}\text{thallium}$  uptake.

Spearman's correlation coefficient was used to assess if there is a relationship between  $K_i$  and  $\lambda$ , in all thirty ROIs per patient. No relationship was seen as there was a very low correlation coefficient ( $r=-0.057$ ;  $p\text{-value}=0.387$ ).

## 5.5 Discussion

Dynamic images of the myocardium from patients admitted to hospital with an acute myocardial infarction were obtained in this study using MR imaging. The  $K_i$  was calculated for these patients and compared to  $^{201}\text{Tl}$  SPECT assessment. The  $K_i$  values obtained here are higher than those obtained by Larsson's group (1996). There may be several reasons for this. Larsson's group (1996) applied a more complex model of  $K_i$  calculation than the simple model used here (Larsson *et al* 1994) and obtained only one slice through the myocardium. For the study presented here, there is a reduction in the temporal resolution caused by increasing the number of slices in order to obtain adequate coverage of the myocardium. This may then not be able to image the peak of the contrast agent bolus in the left ventricle as there is approximately 6 seconds between images. Also it is important that the myocardial response can be measured accurately. If the temporal resolution was increased by reducing the number of slices obtained, this may reduce the clinical effectiveness of the procedure if the slice does not contain the diseased myocardium.

In this study, Gd-BOPTA has been used as the contrast agent, compared to Gd-DTPA which has been used by other groups (Larsson *et al* 1994, 1996 Diesboug *et al* 1992). Gd-BOPTA distributes in the extracellular fluid space, and its plasma kinetics were thought to be similar to Gd-DTPA (Rosati *et al* 1994). Gd-BOPTA has been shown to be selectively taken up by hepatocytes and excreted in bile, where it has shown high signal enhancement compared to other contrast agents (Dawson *et al* 1994, Vogl *et al* 1992, Runge *et al* 1997). In the liver evidence of Gd-BOPTA binding to plasma proteins and so accounting for an increase in the relaxivity has not been found (Vittadini *et al* 1988). Further studies postulate that the higher relaxivity in liver is due to either an increase in the microviscosity inside the hepatocyte, or due to a transient interaction of Gd-BOPTA with intracellular proteins (Schumann 1993, Caudana *et al* 1996, Schima *et al* 1997).

Within myocardium, an increase of 58% in the relaxivity of Gd-BOPTA in reperfused myocardial infarcts compared to its relaxivity in blood has been reported (Cavagna *et al* 1994), and is thought to be due to protein binding. For Gd-DTPA, there was a similar increase in relaxivity, 56%, when moving from blood to reperfused myocardial infarct (Cavagna *et al* 1994). This has implications for  $K_i$  measurement as a requirement of the model is that the contrast agent has a constant relaxivity (Tofts 1997). In the case of



Gd-BOPTA, where there is an increase in the myocardial albumin concentration, there is a change in the relaxivity between blood and myocardium. So, an estimation of Gd-BOPTA concentration ( $[Gd-BOPTA]$ ) based on  $[Gd-BOPTA] = \Delta R_1 / \rho$ , ( $\rho$ =relaxivity Gd-BOPTA) (Strich *et al* 1985, Koenig *et al* 1986, Burstein *et al* 1991) may not hold true. The problem is that the time scale of the change in the relaxivity is not known, as the relaxivity has not been investigated during bolus administration of Gd-BOPTA.

If Gd-BOPTA relaxivity changes rapidly, in this study there would be a change in  $R_1$  which would be very high for blood after the introduction of contrast, with less of a change for normal myocardium, and with a very high change in reperfused myocardium. Overall, the change in  $R_1$  for myocardium was around  $2 \text{ s}^{-1}$  which is similar to values obtained by Larssons group (1994) using Gd-DTPA. For the blood, peak Gd-DTPA concentration of  $3-4 \text{ mmol L}^{-1}$  have been reported (Larsson *et al* 1994, Fritz-Hansen *et al* 1996), which results in  $R_1$  values ranging between  $12-17 \text{ s}^{-1}$ . In this study the peak change in  $R_1$  ranges between  $2-16 \text{ s}^{-1}$ , again the upper end of the range is similar to the results from other studies (Larsson *et al* 1994, Fritz-Hansen *et al* 1996) that have used Gd-DTPA. We have calculated  $K_i$  assuming constant relaxivity. If relaxivity were not constant then our values of  $R_1$  for the blood would be much higher than those reported for Gd-DTPA (Larsson *et al* 1994, Fritz-Hansen *et al* 1996). A problem may be that at very high values of  $R_1$  ( $2-16 \text{ s}^{-1}$ ,  $T_1 = 0.083-0.058 \text{ s}$ ) as found in this study, the calculated  $R_1$  values obtained may not be accurate anyway. This is because the inversion pulse used is of 300ms, and so there would be full relaxation of the magnetisation before image acquisition begins.

Overall, there was shown to be a poor correlation between  $^{201}\text{thallium}$  assessment and  $K_i$ .  $^{201}\text{Thallium}$  SPECT is a technique used to assess myocardial viability (Kuijper *et al* 1992, Iskandrian *et al* 1993, Hendel *et al* 1994).  $K_i$  is a measure reflecting the leakiness of myocardial capillaries (Tofts *et al* 1997). It may be that blinded qualitative  $^{201}\text{thallium}$  assessment by several radiologists may affect the results, as here only one experienced radiologist was used. Alternatively, it may be that  $K_i$  and  $^{201}\text{thallium}$  are showing different information about the physiological state of the myocardium.

There was shown to be no correlation between  $\lambda$  and  $^{201}\text{thallium}$  uptake in this study. Other studies have shown that there is a strongly negative correlation between the partition coefficient of Gd-DTPA ( $\lambda$ ) and  $^{201}\text{thallium}$  uptake (Pereira *et al* 1996). This means that in infarcted myocardium, the cell dies and so  $^{201}\text{thallium}$  is not taken up. Cell

death would result in the loss of cell membrane integrity and an increase in the space to which the MR contrast agent can distribute, thereby increasing  $\lambda$ .

The values obtained for  $\lambda$  are lower than those obtained by Larssons group (1996). Here, an average of 8 ml/100g was obtained compared with 30 ml/100g (Larsson *et al* 1996) obtained in healthy volunteers. It may be that although there is an underestimation of  $\lambda$ , cell death may have been minimised due to the policy of this hospital to administer thrombolytic therapy to eligible patients within 12 hours of myocardial infarction (MI). Patients were imaged early after their MI, between 2-4 days. Even without the use of thrombolytics, acute inflammation has been shown to peak at 3 days post infarction, with necrosis reaching a plateau from 2.5-8 days post infarction before there is a slow decline in the death rate of cells (Fishbein *et al* 1978). It may be that in imaging patients early after their MI, and with many of them receiving thrombolytic therapy, potential increases in  $\lambda$  for some ROIs, reflecting myocardium which has lost cell membrane integrity, have been obscured.

## 5.6 Conclusion

In conclusion, it has been shown that it is feasible to image patients early post MI. The  $K_i$  and  $\lambda$  values obtained from this study were higher and lower respectively than those obtained in healthy volunteers by other workers (Larsson *et al* 1996). This may be due characteristics of the contrast agent used, or to the lower temporal resolution when imaging myocardium to obtain clinical effectiveness. Further research using relaxation contrast agents during dynamic imaging with a higher temporal resolution is needed.

## 5.7 References

- Atkinson DJ, Burstein D, Edelman RR. First pass cardiac perfusion: evaluation with ultrafast MR imaging. *Radiology* 174:757-762 1990.
- Beanlands R S, Dawood F, Wen W H. Are the kinetics of technetium-99m methoxyisobutyl-isonitrile affected by cell metabolism viability. *Circulation* 82:1802-1084 1990.
- Bottomley PA, Foster TA, Arsinger RE, Pfeifer LM. A review of normal tissue hydrogen relaxation times and relaxation mechanisms from 10199 MHz: dependence on tissue type, NMR frequency, temperature, species, excision and age. *Med Phys* 11:425-448, 1984
- Brix G, Semmler W, Port R, Schad L R, Layer G, Lorenze W J. Parametrization of the MRI signal enhancement during and after i.v. infusion of Gd-DTPA: a pharmacokinetic model. In: Proceedings of the 9th annual meeting of the Society of Magnetic Resonance in Medicine. New York. Society of Magnetic Resonance in Medicine, 2:758 1990.
- Brix G, Semmler W, Port R, Schad L R, Layer G, Lorenze W J. Pharmacokinetic parameters in CNS Gd-DTPA enhanced imaging. *J Comput Assist Tomogr.* 15:621-628 1992.
- Burstein D, Taratuta E, Manning W. Factors in Myocardial "Perfusion" Imaging with Ultrafast MRI and Gd-DTPA Administration. *Magn. Reson. Med.* 20:299-205 1991.
- Caputo GR, Suzuki JI, Kondo C, Cho H, Quaife RA, Higgins CB, Parker DL. Determination of left ventricular volume and mass with the use of biphasic spin echo imaging: Comparison with cine MR. *Radiology* 177:773-777 1990.
- Caudana R, Morana G, Pirovano G, *et al.* Focal Malignant Hepatic Lesions: MR Imaging Enhanced with Gadolinium Benzyloxypropionictetra-acetate(BOPTA) - Preliminary Results of Phase II Clinical Application. *Radiology.* 199:513-520 1996.

Cavagna F, Marzola P, Dapra M *et al.* Binding of Gadobenate Dimeglumine to Proteins Extravasated into Interstitial Space Enhances Conspicuity of Reperfused Infarcts. *Invest. Radiology*. 29(supp 2); S50-S53 1994.

Cranny CB, Lotan CS, Dean L, Baxley W, Bouchard A, Pohst GM. Left ventricular volume measurement using cine axis nuclear magnetic resonance imaging. *Circulation* 82:154-163 1990.

Dawson P, Blomley M. Gadolinium Chelate MR Contrast Agents. Editorial. *Clinical Radiology*. 49:439-442 1994

Diesbourg L, Prato F, Wisenberg G, *et al.* Quantification of Myocardial Blood Flow and Extracellular Volumes Using a Bolus Injection of Gd-DTPA: Kinetic Modelling in Canine Ischemic Disease. *Magn. Reson. Med.* 23:239-253 1992.

Donahue K, Burstein D, Manning W, Gray M. Studies of Gd-DTPA Relaxivity and Proton Exchange Rates in Tissue. *Magn. Reson. Med.* 32:66-76 1994.

Donahue K, Weisskoff R, Burstien D. Water Diffusion and Exchange as They Influence Contrast Enhancement. *Journal Magn. Reson. Imaging*. 7:102-110 1997.

Donahue K, Weisskoff R, Parmelee D J, *et al.* Dynamic Gd-DTPA enhanced measurement of tissue volume fraction. *Magn. Reson. Med.* 34:423-432 1995.

Eichenberger AC, Schuiki E, Kochli VD, Amann FW, McKinnon GC, von Schulthess GK. Ischemic heart disease: Assessment with gadolinium-enhanced ultrafast MR imaging and dipyridamole stress. *J. Magn. Reson. Imaging* 4:425-431 1995.

Fishbein M, Maclean D, Maroko P. The Histopathologic Evolution of Myocardial Infarction. *Chest* 73:843-849 1978

Fritz-Hansen T, Rostrup E, Larsson H, Sondergaard L, Ring P, Henriksen O. Measurement of the Arterial Concentration of Gd-DTPA Using MRI: A Step Toward Quantitative Perfusion Imaging. *Magn. Reson. Med.* 36:225-231 1996.

Gadian D, Payne J, Bryant D, Young I, Carr D, Bydder G. Gadolinium-DTPA as a Contrast Agent in MR Imaging - Theoretical Projections and Practical Observations. *Journal of Computer Assisted Tomography*. 9(2):242-251 1985.

Hendel R C. Single photon perfusion imaging for the assessment of myocardial viability. *J. Nucl. Med.* 35(Suppl):23S-31S 1994

Higgins CB, Lanzer P, Stark D, Crooks LE, Kaufman L. Assessment of cardiac anatomy using nuclear magnetic resonance imaging. *J. Am. Coll. Cardiol.* 5(Suppl. 1):775-815 1985.

Hittmair K, Gomiscek G, Langenberger K, Recht M, Imhof H, Kramer J. Method for the Quantitative Assessment of Contrast Agent Uptake in Dynamic Contrast-Enhanced MRI. *Magn. Reson. Med.* 31:567-571 1994.

Iida H, Kanno I, Takahashi. Measurement of absolute myocardial blood flow with  $H_2^{15}O$  and dynamic positron emission tomography. *Circulation* 78:104-115 1988.

Iskandrian A S. Thallium reinjection imaging: the search for an optimal protocol. *J. Nucl. Med.* 34(5):743-746 1993

Kety SS. The theory and applications of the exchange of inert gas at the lungs and tissue. *Pharmacol. Rev* 3:1-4 1951

Koenig S H, Spiller M, Brown R III, Wolf G L. Relaxation of water protons in the intra- and extracellular regions of blood containing Gd(DTPA). *Magn. Reson. Med.* 3:791-795 1986.

Kuijper A F, Vliegen H W, van der Wall E E, *et al.* The clinical impact of thallium-201 reinjection scintigraphy for the detection of myocardial viability. *Euro. J. Nucl. Med.* 19:78-789 1992.

Larsson HBW, Fritz-Hansen T, Rostrop E, S ndergaard L, Ring P, Henriksen O. Myocardial perfusion modelling using MRI. *Magn Reson Med.* 35:716-726 1996

Larsson HBW, Stubgaard M, S ndergaard L, Henriksen O. In vivo quantification of the unidirectional influx constant for Gd-DTPA diffusion across the myocardial capillaries with MR imaging. *J Magn Reson*, 4:433-440 1994.

Maddahi J, Crues J, Berman DS, Mericle J, Becerra A, Garcia EV, Henderson R, Bradley W. Non invasive quantification of left ventricular myocardial mass by gated proton nuclear magnetic resonance imaging. *J. Am. Coll. Cardiol.* 10:682-692 1987.

Manning WJ, Atkinson DJ, Grossman W, Paulin S, Edelman RR. First pass nuclear magnetic resonance imaging studies with gadolinium-DTPA in patients with coronary artery disease. *J. Am. Coll. Cardiol.* 18:959-965 1991.

Miller DD, Holmvang G, Gill JB, Dragotakes D, Kantor HL, Okada RD, Brady TJ. MRI detection of myocardial perfusion changes by gadolinium-DTPA infusion during dipyridamole hyperemia. *Magn. Reson. Med.* 10:246-255 1989.

Mirrghoseini M, Shelgikar S, Clayton MM. New concepts in revascularisation of the myocardium. *Ann. Thorac. Surg.* 45:415-420 1988.

Pearlman JD, Hibberd MG, Chuang ML, et al. Magnetic resonance mapping demonstrates benefits of VEGF-induced myocardial angiogenesis. *Nat Med* 1:1085-1089 1995.

Pereira R, Prato F, Wisenberg G, Sykes J. The Determination of Myocardial Viability Using Gd-DTPA in a Canine Model of Acute Myocardial Ischemia and Reperfusion. *Magn. Reson. Med.* 36: 684-693 1996.

Prato F, Wisenberg G, Marshall T P, Lee T Y, Carroll E, Sandler D, Wills J, Drost D. Comparison of the biodistribution of Gadolinium-153 DTPA and Technitium-99 M DTPA in rats. *J. Nuc. Med.* 29(10):1683-1687 1988

Rosati G, Pirovano G, Spinazzi A. Interim Results of Phase II Clinical Testing of Gadobenate Dimeglumine. *Invest. Radiology* 29(supp 2):S183-S185 1994.

Runge V, Lee C, Williams N. Detectability of Small Liver Metastases with Gadolinium BOPTA. *Investig. Radiology* 32(9): 557-565. 1997.

Schaefer S, Massie B, Weiner MW. Magnetic resonance spectroscopy of the heart. *Cardiol. Clin.* 7:697-712 1989.

Schima W, Petersein J, Hahn P, Harisinghani M, Halpern E, Saini S. Contrast-Enhanced MR Imaging of the Liver: Comparison Between Gd-BOPTA and Mangafodipir. *Journal Magn. Reson. Imaging.* 7:130-135 1997.

Schuhmann-Giampieri G. Liver Contrast Media for Magnetic Resonance Imaging. Interrelations between Pharmacokinetics and Imaging. *AJR* 28(8):753-761. 1993.

Siemens Operating Instructions. Macro programming environment (MPE) applications. Siemens Medical Imaging, Erlangen, Germany. Published 1994.

Strich G, Hagan P L, Slutsky R A. Tissue distribution and magnetic resonance spin lattice relaxation effects of gadolinium-DTPA. *Radiology* 154:723-726 1985.

Stirner H, Bull U, Kleinhans E. Three dimensional ROI-based quantification of stress/rest 201-Tl myocardial SPECT: Presentation of method. *Nucl. Med.* 25:128-133 1986.

Tofts P, Kermode A. Measurement of the Blood Barrier Permeability and Leakage Space Using Dynamic MR Imaging. 1. Fundamental Concepts. *Magn. Reson. Med.* 17:357-367 1991.

Tofts P. Modelling Tracer Kinetics in Dynamic Gd-DTPA MR Imaging. *J Magn. Reson. Imaging.* 7:91-101, 1997.

Tong C Y [I], Prato F, Wisenberg G, Lee T, Carroll E, Sandler D, Wills J. Techniques for the Measurement of the Local Myocardial Extraction Efficiency for Inert Diffusible Contrast Agents such as Gadopentate Dimeglumine. *Magn. Reson. Med.* 30:332-336 1993.

Tong C Y [II], Prato F, Wisenberg G, Lee T, Carroll E, Sandler D, Wills J, Drost D. Measurement of the Extraction Efficiency and Distribution Volume for Gd-DTPA in Normal and Diseased Canine Myocardium. *Magn. Reson. Med.* 30:337-446 1993.

Vittadini G, Felder E, Tirone P, Lorusso V. B-19036, A Potential New Hepatobiliary Contrast Agent for MR Proton Imaging. *Invest. Radiology* 1988; 23(Supp 1):S246-S248.

Vogl T, Pegios W, McMahon C, *et al.* Gadobenate Dimeglumine - a New Contrast Agent for MR Imaging: Preliminary Evaluation in Healthy Volunteers. *AJR* 158: 887-892, 1992.

Wedeking P, Sotak C, Tesler J, Kumar K, Chang C, Tweedle M. Quantitative Dependence of MR Signal Intensity on Tissue Concentration of Gd(HP-DO3A) in the Nephrectomized Rat. *Magn. Reson. Imaging.* 10:97-108 1992.

Wilke N, Jerosch-Herold M, Wang Y, *et al.* Myocardial Perfusion Reserve: Assessment with Multisection, Quantitative, First-Pass MR Imaging. *Radiology.* 204:373-384 1997.

Wilke N, Simm C, Zhang J, Ellerman J, *et al.* Contrast-Enhanced First Pass Myocardial Perfusion Imaging: Correlation Between Myocardial Blood Flow in Dogs at Rest and During Hyperemia. *Magn. Reson. Med.* 29:485-497 1993



## **Chapter 6: MR enhancement of human myocardium *in vivo*, post acute myocardial infarction using Gd-BOPTA.**

### **6.1 Introduction**

The use of a contrast agent to discriminate between normal and infarcted regions of myocardium was first applied by Lauterbur in 1973. A manganese salt was used as the contrast agent and Lauterbur found that the longitudinal relaxation rate ( $R_1=1/T_1$ ) correlated with tissue concentration, so enabling relaxation behaviour to distinguish normal myocardium from infarcted. Contrast agents have now become a very important part of diagnostic imaging, improving the contrast between normal and diseased tissue. They can also be used to provide information about the functional status of an organ (Manning *et al* 1991).

Contrast agents are able to affect nuclear relaxation rates because they have unpaired electrons. For gadolinium ions, the efficiency of relaxation enhancement is roughly proportional to the number of unpaired electrons, (Gd-III=7). Gadolinium is a highly magnetic but toxic metal ion. It can be used clinically because it is chelated to an organic ligand eg benzyloxypropionictetraacetate (BOPTA), diethylenetriaminepentaacetic acid (DTPA), which reduces its toxicity. The differences between the various gadolinium based contrast agents are in the organic ligands used, which may affect the relaxivity, toxicity, biodistribution and excretion of the contrast agent.

The relaxivity of an agent describes the efficiency with which it is able to enhance the proton relaxation rate of water. In the case of  $T_1$  agents, these have the effect of increasing tissue signal intensity, on  $T_1$ -weighted images (Gadian *et al* 1985). The relaxivity of an agent in tissues is dependant upon whether the agent binds to macromolecular structures, which increase relaxivity. Also the compartmentalisation of the agent also has an effect upon relaxivity. Tissue water is compartmentalised into intravascular (~5%), interstitial (extracellular, extravascular) (~15%) and intracellular (~80%). If there is a slow exchange of water between these compartments, extracellular

contrast agents are not exposed to all tissue water, and so there is a reduction in the effective tissue relaxivity, and there will be multicomponent relaxation.

The toxicity of a gadolinium complex is related to the dissociation *in vivo* of the free metal ion (Gd), and the ligand (i.e. BOPTA or DTPA) before excretion. The biodistribution and excretion of a contrast agent is determined by its structure. Hydrophilic chelates with low molecular weight are filtered out by the kidneys if they do not bind to proteins (Venkatachalam *et al* 1978). If the chelate maintains a balance between a hydrophobic and a hydrophilic nature, then it is excreted by the liver (Klassen *et al* 1984). In this case, it often displays protein binding, particularly to albumin, reducing its excretion by glomerular filtration. To minimise toxicity, excretion by both or either routes is desired. Chronic toxicity results when a lipophilic agent is used, which is then distributed to fat storage sites, membranes or taken up by the reticuloendothelial system.

Gd-BOPTA is a low molecular weight, extracellular contrast agent whose plasma kinetics are similar to other gadolinium chelate contrast agents (Rosati *et al* 1994). This agent has shown an affinity for biliary excretion, with between 2-4% of the contrast agent being excreted by the liver in humans (Vogl *et al* 1992). Due to this excretion route, enhancement of liver parenchyma has increased lesion detectability (Dawson *et al* 1994, Runge *et al* 1997). Low biliary excretion and yet high enhancement may be due to an increase in the relaxivity of this contrast agent in the liver. It has been hypothesised that this may occur because of a weak binding of the agent with serum proteins (Cavagna *et al* 1994), and has the effect of increasing the signal intensity on  $T_1$  weighted imaging, although this has not been proven in the liver (Vittadini *et al* 1988). It has been suggested that there may be other factors responsible for the increase in relaxivity of Gd-BOPTA inside the liver such as a change in microviscosity inside the hepatocyte or a transient interaction with intracellular proteins (Schumann *et al* 1993, Caudana *et al* 1996, Schima *et al* 1997).

In tissues there will be a steady concentration of serum proteins in the interstitium defined by the rates of extravasation and lymph drainage. In acute myocardial infarction (AMI) and following reperfusion the equilibrium concentration of serum proteins will be increased due to the leakiness of the capillaries. Also the distribution volume for the contrast agent will be increased due to a breakdown of myocytes. These factors combine to increase the tissue concentration of the contrast agent and with an increase in relaxivity, result in high differential signal enhancement of injured compared to normal tissue in rats

(Cavagna *et al* 1994). This contrast has been shown in human pilot studies to peak 30 minutes after administration for enhancement of brain lesions and AMI, and 30-40 minutes for liver lesions (Rosati *et al* 1994).

## 6.2 Aims

Gd-BOPTA is rapidly excreted from the body, following intravenous injection, with a half life elimination phase of ~15 minutes, and so is similar to Gd-DTPA (~17 minutes) (Vittadini *et al* 1988). If there is no *in vivo* binding of the contrast agent within human myocardium, then a reduction in the MR signal enhancement would be expected at 30 minutes post contrast.

This study aimed to assess the difference in myocardial signal enhancement between 15 and 30 minutes after administering Gd-BOPTA to AMI patients. Following the independent determination of normal and infarcted myocardium, using baseline <sup>201</sup>thallium SPECT imaging, the study also aimed to ascertain if there is an increase in the differential enhancement of injured myocardium in these patients.

## 6.3 Method

Twenty seven patients admitted to our hospital with acute myocardial infarction received an MR imaging scan within 2-4 days using a whole body MRI system (MAGNETOM IMPACT, Siemens, Erlangen, Germany) operating at 1.0 Tesla. An ECG gated  $T_1$  weighted short axis spin echo sequence was performed before the introduction of 0.05mmol/Kg Gd-BOPTA, and the sequence was repeated at 15, and 30 minutes post contrast. A nickel chloride paramagnetic standard (PS) was used during imaging to enable normalisation of the MR signal. The imaging parameters were TR/TE 589/25ms, 8mm thickness, 1.6mm gap, 11 slices, FOV 350mm, 3 acquisitions 128×256 matrix.

Three slices corresponding to above, through and below the papillary muscle were identified by a consultant radiologist. Each of these three slices was divided into ten regions of interest (ROI); and the signal intensities (SI) were quantitatively assessed and normalised to the paramagnetic standard (PS) using Eq.[6.1], and the signal enhancement was calculated Eq.[6.2].

$$SI_{normalised} = \frac{SI}{SI_{PS}} \quad [6.1]$$

$$Enhancement = \frac{SI_{PostContrast\_Normalised} - SI_{PreContrast\_Normalised}}{SI_{PreContrast\_Normalised}} \quad [6.2]$$

Within 24 hours of the MR scan, patients also received a resting <sup>201</sup>thallium SPECT scan. Three images corresponding to above, through and below the papillary muscle, and on the same ROI basis as for MR images were semi quantitatively assessed using the Stirner method (Stirner *et al* 1986) which has been described in 5.3.2. ROIs with normal <sup>201</sup>thallium uptake were semi quantitatively identified from those with reduced uptake.

## 6.4 Results

ROIs were divided into two groups according to <sup>201</sup>thallium uptake:- normal and reduced. The mean MR signal in each of the 30 ROIs for each patient was analysed, and signal enhancement was calculated. The percentage signal enhancement at both 15 and at 30 minutes post contrast was assessed, for ROI's with normal and reduced <sup>201</sup>thallium uptake. The results are summarised in table 6.1 below. It can be seen that at 15 minutes post contrast, there is still a high percentage enhancement of both normal and reduced <sup>201</sup>thallium uptake ROI's, even though half the injected dose should have been excreted. The ROI's with reduced <sup>201</sup>thallium show higher enhancement than those with normal uptake.

	<sup>201</sup> Thallium uptake	
	Normal	Reduced
Mean MR signal enhancement at 15 minutes post contrast (2×[Standard Deviation])	39.2% (77)	43.8% (92)
Mean MR signal enhancement at 30 minutes post contrast (2×[Standard Deviation])	39.5% (86)	46.0% (97)
Number of ROIs	315	495

Table 6.1. Shows the mean percentage signal enhancement for myocardial ROIs at 15 and at 30 minutes post contrast.

Student's *t*-tests were performed on the data to see if there was a significant change in the signal enhancement between the 15 and 30 minute images for both the normal and the reduced uptake ROI's. The tests performed are summarised in table 6.2 below.

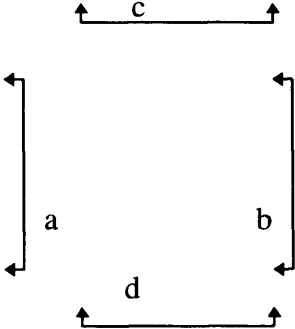
	<sup>201</sup> Thallium uptake	
	Normal	Reduced
Mean MR signal enhancement at 15 minutes post contrast		
Mean MR signal enhancement at 30 minutes post contrast		

Table 6.2 showing the sets of data upon which the Student's *t*-test was performed.

The signal enhancement between 15 minutes post contrast and 30 minutes post contrast for both normal (a) and reduced <sup>201</sup>thallium (b) ROI's did not show a significant difference. This means that there has been no real change in the signal enhancement, although the percentage enhancement has slightly increased during this time interval. One would expect that during this time interval the plasma concentration of Gd-BOPTA would have been reduced, it is a freely diffusable extravascular contrast agent, with a half life of ~15 minutes. Certainly by 30 minutes post contrast, a reduction in the myocardial concentration would be expected, accompanied by a reduction in the signal enhancement if there was no protein binding of the agent.

From the data in table 6.1, we can see that there is a higher percentage signal enhancement in ROI's with reduced <sup>201</sup>thallium uptake than in ROI's with normal uptake at both 15 minute (c), and 30 minute (d) post contrast. A Student's *t*-test was performed on the signal enhancement at 15 minutes post contrast (c), and this showed there was no significant difference between normal and reduced <sup>201</sup>thallium uptake ROI's. However, at 30 minutes post contrast, there was a significant difference (*p*=0.05) between the signal enhancement of ROI's with normal and those with reduced <sup>201</sup>thallium uptake. This is suggestive of contrast agent binding, as ROI's with reduced <sup>201</sup>thallium uptake following

AMI are more likely to have damaged cells, so reducing the membrane integrity and allowing the contrast agent to diffuse among intracellular contents.

A plot of the mean difference in signal enhancement between 15 and 30 minutes post contrast is shown below in Fig.6.1 for both normal and reduced  $^{201}\text{Tl}$  uptake ROI's. ROIs with normal  $^{201}\text{Tl}$  uptake showed a mean difference in signal enhancement between 15 and 30 minutes of 0.35% with 95% confidence between a range of 48% and -47%. ROIs with reduced  $^{201}\text{Tl}$  uptake had a mean signal enhancement of 2.42% and at 95% confidence between a range of 38% and -34%. A students *t*-test performed on mean difference in signal enhancement for the reduced and the normal  $^{201}\text{Tl}$  uptake ROI's, showed that there is no significant difference in these tissue states. This indicates that the difference in signal enhancement for both the tissue states is similar. Although there is a slightly higher degree of enhancement for ROI's with reduced  $^{201}\text{Tl}$  uptake, there is little change in the signal enhancement between 15 and 30 minutes post contrast. This is during the dual excretion of the contrast agent by both the kidneys and the liver, and one would expect that as the plasma concentration would be falling, so would the myocardial concentration. If there was no protein binding in the myocardium the signal enhancement would begin to fall.

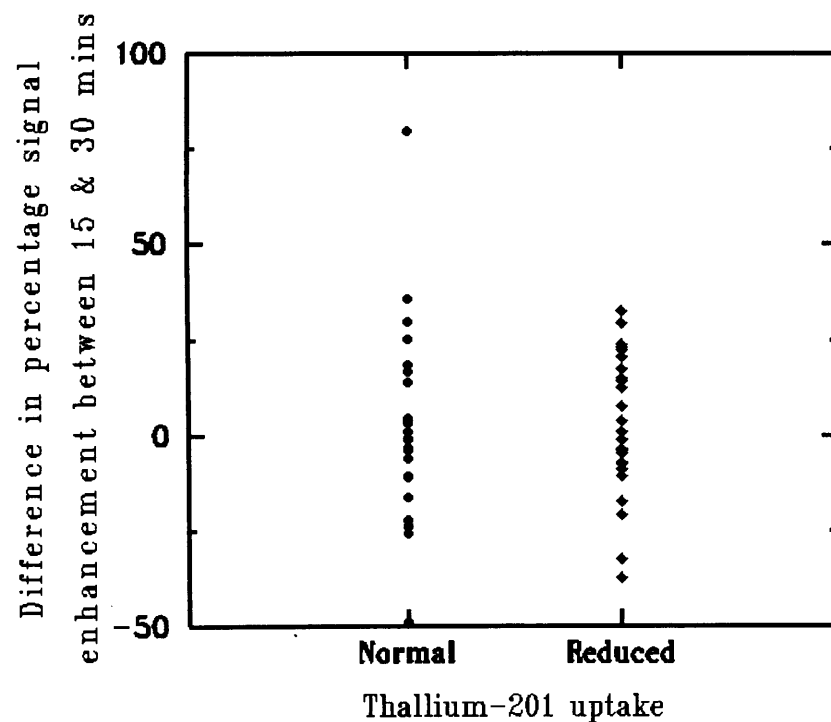


Figure 6.1 Shows the mean difference in percentage enhancement between 15 & 30 minute images for normal and reduced  $^{201}\text{Tl}$  uptake in each patient.

## 6.5 Discussion

Gd-BOPTA is rapidly excreted from the body with a half-life for elimination of ~15 minutes (Vittadini *et al* 1988). If the contrast agent does not bind to proteins *in vivo*, then we would expect that the plasma concentration would start to fall as the contrast agent is rapidly excreted. As a consequence the myocardial concentration of the contrast agent would also start to fall, as the contrast agent would diffuse back into the blood. We would then expect to see a reduction in MR signal enhancement between 15 and 30 minutes. The results have not shown this. The results have shown that the signal enhancement at 15 minutes post contrast and 30 minutes post contrast remain very similar. This is the case for both normal and reduced  $^{201}\text{Tl}$  uptake ROI's and suggest there is binding.

Following AMI, ROI's with reduced  $^{201}\text{Tl}$  uptake are likely to have a loss of cell membrane integrity. This will increase both the distribution volume of the contrast agent as well as allow the contrast agent to diffuse within intracellular contents including proteins. If the contrast agent binds to proteins, then we would expect that ROI's with reduced  $^{201}\text{Tl}$  uptake would have a significantly higher signal enhancement than normal uptake ROI's. This is because they are likely to have a higher relaxivity due to contact with intracellular proteins. This has been shown by the data at 30 minutes post contrast, and is further evidence that there is binding of the contrast agent *in vivo*.

If Gd-BOPTA does in fact bind *in vivo*, this has implications for perfusion imaging. Binding of a  $T_1$  contrast agent to macromolecules such as proteins, increases the relaxivity of the agent, and so causes a much larger increase in signal on  $T_1$  weighted image. This is desirable when qualitatively assessing images, as it increases the conspicuity of lesions. However, if the measurement of signal intensity is to be used to estimate contrast agent concentration for kinetic modelling purposes, then problems arise as a constant relaxivity is one simplifying assumption required in order to achieve this (Tofts 1997).

However, the time scale of the binding and therefore its eventual effect on relaxivity also has to be considered. If first pass dynamic contrast enhanced imaging is used but the protein binding is not instantaneous, resulting in a delay before the increased relaxivity of the contrast agent is able to affect the image signal intensity, then binding of the contrast agent is not important. However, if there is instantaneous binding so altering relaxivity, then it is not possible to non invasively estimate contrast agent concentration (Strich *et al* 1985, Koenig *et al* 1986, Burstein *et al* 1991). This is because contrast agent

concentration is calculated by measuring the change in  $R_1$ , and dividing this by the relaxivity of the agent. It is not possible to measure both of these simultaneously during dynamic contrast enhanced imaging, and so calculation of perfusion using kinetic modelling is not possible if the change in concentration of the contrast agent is not known.

## 6.6 Conclusion

The study has shown that at 30 minutes post contrast, there is a significant difference between the signal enhancement of myocardial ROI's with reduced  $^{201}\text{Tl}$  uptake compared to normal ROI's. Also, both for normal and reduced  $^{201}\text{Tl}$  uptake ROI's, there was no difference in the signal enhancement at 15 minutes post contrast and at 30 minutes post contrast, even though more than half the contrast agent dose should have been excreted. An explanation for these findings may be that there is an increase in the relaxivity of the remaining contrast agent, possibly due to protein binding. This would account for the greater increase in enhancement of ROI's with reduced  $^{201}\text{Tl}$  uptake as these may contain more plasma proteins due to the leakiness of capillaries and the breakdown of myocytes.



## 6.7 References

Burstein D, Taratuta E, Manning W. Factors in Myocardial "Perfusion" Imaging with Ultrafast MRI and Gd-DTPA Administration. *Magn. Reson. Med.* 20:299-205 1991.

Caudana R, Morana G, Pirovano G, Nicoli N, Portuese A, Spinazzi A, Rito R, Pistolesi G. Focal Malignant Hepatic Lesions: MR Imaging Enhanced with Gadolinium Benzyloxypropionictetra-acetate(BOPTA) - Preliminary Results of Phase II Clinical Application. *Radiology.* 199:513-520 1996.

Cavagna F, Marzola P, Dapra M *et al.* Binding of Gadobenate Dimeglumine to Proteins Extravasated into Interstitial Space Enhances Conspicuity of Reperfused Infarcts. *Invest. Radiology.* 29(supp 2); S50-S53 1994.

Dawson P, Blomley M. Gadolinium Chelate MR Contrast Agents. Editorial *Clinical Radiology.* 49:439-442. 1994

Gadian D, Payne J, Bryant D, Young I, Carr D, Bydder G. Gadolinium-DTPA as a Contrast Agent in MR Imaging - Theoretical Projections and Practical Observations. *Journal of Computer Assisted Tomography.* 9(2):242-251 1985.

Klaassen CD, Watkins JB III. Mechanisms of bile formation, hepatic uptake, and biliary formation. *Pharmacological Review* 36:1 1984.

Koenig SH, Spiller M, Brown R III, Wolf GL. Relaxation of water protons in the intra- and extracellular regions of blood containing Gd(DTPA). *Magn. Reson. Med.* 3:791-795 1986.

Lauterbur PC. Image formation by induced local interactions: examples employing nuclear magnetic resonance. *Nature* 242:190-191 1973

Manning WJ, Atkinson DJ, Grossman W, Paulin S, Edelman RR. First-pass nuclear magnetic resonance imaging studies using gadolinium-DTPA in patients with coronary artery disease. *J Am Coll Cardiol* 18:959-965 1991

Rosati G, Pirovano G, Spinazzi A. Interim Results of Phase II Clinical Testing of Gadobenate Dimeglumine. *Invest. Radiology* 29(supp 2):S183-S185 1994.

Runge V, Lee C, Williams N. Detectability of Small Liver Metastases with Gadolinium BOPTA. *Investig. Radiology* 32(9): 557-565. 1997.

Schima W, Petersein J, Hahn P, Harisinghani M, Halpern E, Saini S. Contrast-Enhanced MR Imaging of the Liver: Comparison Between Gd-BOPTA and Mangafodipir. *Journal Magn. Reson. Imaging*. 7:130-135 1997.

Schuhmann-Giampieri G. Liver Contrast Media for Magnetic Resonance Imaging. Interrelations between Pharmacokinetics and Imaging. *AJR* 28(8):753-761. 1993.

Strich G, Hagan P L, Slutsky R A. Tissue distribution and magnetic resonance spin lattice relaxation effects of gadolinium-DTPA. *Radiology* 154:723-726 1985.

Stirner H, Bull U, Kleinhans E. Three dimensional ROI-based quantification of stress/rest 201-Tl myocardial SPECT: Presentation of method. *Nucl. Med.* 25:128-133 1986.

Tofts P, Kermode A. Measurement of the Blood Barrier Permeability and Leakage Space Using Dynamic MR Imaging. 1. Fundamental Concepts. *Magn. Reson. Med.* 17:357-367 1991.

Venkatachalam MA, Rennike HG. The structural and molecular basis of glomerular filtration. *Circulation research* 43:337 1978

Vittadini G, Felder E, Tirone P, Lorusso V. B-19036, A Potential New Hepatobiliary Contrast Agent for MR Proton Imaging. *Invest. Radiology* 1988; 23(Supp 1):S246-S248.

Vogl T, Pegios W, McMahon C, *et al.* Gadobenate Dimeglumine - a New Contrast Agent for MR Imaging: Preliminary Evaluation in Healthy Volunteers. *AJR* 158: 887-892, 1992.

## Chapter 7: Thesis conclusions

The thesis has reviewed the currently available methods of quantitatively assessing myocardial perfusion. Ideally, a technique should allow accurate measurements of perfusion to be made at a range of blood flows, with high spatial and temporal resolution. Also, the measurement should not affect the measured perfusion, and should enable perfusion in the transmural layers of the myocardium to be assessed. The currently available techniques are of limited value when applied to humans. Some are unable to quantitatively assess perfusion; others may have poor temporal resolution; and most have poor spatial resolution, or are invasive.

MRI is a non invasive imaging technique with good spatial resolution enabling transmural myocardial layers to be assessed. Fast imaging techniques have increased its temporal resolution enabling dynamic imaging so that the movement of a bolus of contrast agent can be tracked through the myocardium. If the change in concentration of the bolus can be accurately measured, then tracer kinetic models can be applied, and the calculation of perfusion in ml/min/g is possible.

The first experimental section of the thesis (Chapter 3), investigated the errors that are introduced into the assessment of relaxation time when using a fast imaging sequence (snapshot FLASH), and showed how this sequence could be applied to dynamic cardiac imaging. The aim was to optimise the imaging methodology by correcting for the errors found, and this was then tested on phantoms.

The next section applied the corrections tested on phantoms to healthy human volunteers for baseline (pre contrast) measurements of the myocardium, and phantoms for post contrast measurements. The sequence behaved as predicted.

Then, patients with acute myocardial infarction were imaged dynamically. The concentration of the Gd-BOPTA contrast agent was estimated using the techniques and corrections described in previous chapters, and a tracer kinetic model was applied to the data representing the movement of the contrast agent through the myocardium. The values estimated for  $K_i$  were higher than those obtained by Larssons group (Larsson 1994). This brought into question the behaviour of the contrast agent, and whether this may be responsible for the unexpected results.

The final experimental section investigated the effect of the contrast agent on the MR signal intensity *in vivo*. It was shown that this behaves differently to a currently available agent (Gd-DTPA), and so could be responsible for the spurious  $K_i$  results. Further work is required by applying this technique of  $K_i$  measurement using Gd-DTPA instead of Gd-BOPTA.

The clinical section of this study was part of a larger study funded by Bracco SpA., Milan Italy. The patients were enrolled into a phase III clinical trial investigating the safety and efficacy of Gd-BOPTA in patients with acute myocardial infarction. This introduced several problems into the experimental section of the Ph.D. thesis.

The phantom studies should ideally have used Gd-BOPTA instead of Gd-DTPA. However, at the time of conducting the phantom experiments, Gd-BOPTA was an unlicensed drug. Bracco were unable to supply any Gd-BOPTA, and we were not allowed to use any remnants from the patient vials as it all had to be returned to Bracco.

The MR imaging parameters used in the study were set before the start of the clinical trial to optimise qualitative assessment of the MR images. This also introduced problems for the Ph.D. thesis. It became evident early on in the clinical study that the MR imaging parameters would need to be altered in order to obtain accurate quantitative perfusion data for the Ph.D. thesis. This was not possible as the parameters had been optimised for the qualitative assessment of images for the phase III clinical trial, and were fixed in the trial protocol.

Further complications have been introduced as it has become evident that Gd-BOPTA behaves differently *in vivo* from currently existing MR contrast media. As discussed in the final experimental chapter, the relaxivity of Gd-BOPTA does not appear to remain constant and evidence suggests that it may increase through protein binding. This is an advantage when assessing images qualitatively as there is a greater enhancement in abnormal tissue than in normal tissue, thus increasing lesion conspicuity. However, in order to quantitatively assess perfusion, the contrast medium has to have a constant relaxivity in its passage from the blood into both normal and abnormal tissue. Thus, Gd-BOPTA introduced an extra complication into the interpretation MR signal data *in vivo* as it does not appear to have a constant relaxivity.

There have been several lessons learned from this study which can be of use in cardiac MRI. First, for quantitative perfusion imaging, the use of a contrast agent in dynamic imaging whose kinetic behavior *in vivo* is well documented (e.g. Gd-DTPA)

would be an advantage. This would enable easier interpretation of the MR signal changes. Secondly, the corrections required when images are cardiac gated in dynamic studies are applicable in all quantitative  $T_1$  measurement studies where full longitudinal relaxation is not allowed between sequential image acquisitions. Thirdly, there is a greater understanding of the relationship between the reduction in the overall sequence repetition time and the MR signal intensity change, at different  $T_1$ 's. This is useful when maximising image contrast for a chosen tissue using the snapshot FLASH sequence.

This work is now being extended to investigate quantitative myocardial perfusion in patients with coronary artery stenosis as determined by coronary angiography. A new 1.5T MRI scanner at the Glenfield General Hospital, with gradient strengths of upto 25 mT m<sup>-1</sup>, enables better temporal and spatial resolution than the 1.0T scanner on which the experiments for this thesis were conducted.

The new scanner has the spatial resolution to enable the separate investigation of subendocardial perfusion. This is of particular importance when investigating the significance of a coronary arterial stenosis on the myocardial perfusion bed of that artery as it is in the subendocardium that a reduction in perfusion is first seen. Adenosine 'stress' together with a 'rest' dynamic perfusion images are acquired, and these enable the calculation of the myocardial perfusion reserve index. Most of the lessons learned in this thesis have been applied in this area.

## 7.1 References

Larsson HBW, Stubgaard M, Sondergaard L, Henriksen O. *In vivo* quantification of the unidirectional influx constant for Gd-DTPA diffusion across the myocardial capillaries with MR imaging. *Magn. Reson. Med.* 4, 433-440 1994

## Appendix 1

The  $T_1$ -weighted snapshot FLASH can be written:

$$\left[ \text{TD} - 180^\circ - \text{TI} - [\alpha - \text{TR}]_{Nk} \right]_{Ni}, \quad [\text{A.1}]$$

where TD is an optional delay before the start of the sequence; TI is the inversion time; and  $\alpha$  is the flip angle of the read pulse for acquisition of one line of  $k$ -space. The inner loop is repeated for  $Nk$  lines of  $k$ -space, and the outer loop is repeated  $Ni$  times, according to the number of images required.

Expressions for the  $z$ -magnetization at four stages in the snapshot FLASH sequence have been written by Dr M.A. Horsfield. After several sequence repetitions, so that a steady state is reached, the magnetization at the end of the TD delay is of equal magnitude, but of opposite sign, to that just after the previous  $180^\circ$  pulse. Thus,

$$M^+ = -M^-. \quad [\text{A.2}]$$

Longitudinal relaxation then occurs during the TI period such the magnetization just before the first  $\alpha$  pulse for image acquisition is:

$$M_I^- = M_0(1 - EI) + M^+ EI, \quad [\text{A.3}]$$

where  $EI = \exp(-\text{TI} / T_1)$ , and  $M_0$  is the equilibrium  $z$ -magnetization. After the final  $\alpha$  pulse, the effect of the sequence of  $\alpha$  pulses is such that:

$$M_I^+ = M_I^- (ER \cos(\alpha))^{Nk} + M_0(1 - ER) \left( \frac{(ER \cos(\alpha))^{Nk} - 1}{ER \cos(\alpha) - 1} \right), \quad [\text{A.4}]$$

where  $ER = \exp(-\text{TR} / T_1)$ . At the end of image acquisition, relaxation occurs during the period TD before the next inversion pulse. So, just before the inversion pulse:

$$M^- = M_0(1 - ED) + M_I^+ ED, \quad [\text{A.5}]$$

where  $ED = \exp(-\text{TD} / T_1)$ . Solution of this system of equations leads to a  $z$ -magnetization value just before the  $m$ th line of  $k$ -space of:

$$\frac{M_m}{M_0} = C^{(m-1)} \left( 1 - EI \left( 1 + \frac{\left( 1 - ED(1 - C^{Nk}(1 - EI)) + \frac{ED(ER - 1)(C^{Nk} - 1)}{C - 1} \right)}{1 + ED \cdot C^{Nk} \cdot EI} \right) \right) + (1 - ER) \left( \frac{C^{(m-1)} - 1}{C - 1} \right) \quad [\text{A.6}]$$

where  $C = ER \cos(\alpha)$ . The signal intensity measured is thus  $M_m \sin(\alpha)$ .

Eq. [A.6] can be considerably simplified if a low flip angle is used for the  $\alpha$  pulses. The time from the inversion pulse to the mid-line of  $k$ -space is usually called the *effective* TI ( $TI_{eff}$ ) and is often  $TI + (TR \times (N_k/2 - 1))$ . Also, the overall image repetition time is  $TR_o = TI + (N_k \times TR) + TD$ . For very low flip angle  $\alpha$  pulses, Eq. [A.6] then reduces to:

$$M = M_0 \left( 1 - \frac{2e^{-TI_{eff}/T_1}}{(1 + e^{-TR_o/T_1})} \right). \quad [A.7]$$

where  $M_0$  is now the signal intensity which would be observed with a very long inversion time. When the  $TR_o$  is large compared to  $T_1$ , this expression further reduces to:

$$M = M_0 \left( 1 - 2e^{-TI_{eff}/T_1} \right), \quad [A.8]$$

which has been used in previous studies of dynamic contrast uptake (Larsson *et al* 1996).

Using this expression, it is then a simple matter to calculate the  $T_1$ :

$$T_1(t) = - \frac{TI_{eff}}{\ln \left( \frac{1}{2} \left( 1 - \frac{M(t)}{M_0} \right) \right)}. \quad [A.9]$$

However, when the  $TR_o$  cannot be considered large with respect to  $T_1$ , Eq. [A.7] must apply, from which we have been unable to extract an analytic solution for  $T_1$ . Iterative methods must be applied in order to find the  $T_1$  from a signal intensity ratio ( $M(t)/M_0$ ), even for the low flip angle approximation.

We can see from Eq. [7] that the null-point is given by:

$$TI_{eff} = -\ln \left( \frac{1}{2} \left( 1 + e^{-\frac{TR_o}{T_1}} \right) \right) T_1. \quad [A.10]$$

It is often the case that, in order to maximise the signal dynamic range in contrast-enhanced studies, the tissue to be evaluated is nulled before contrast is introduced. In the short  $TR_o$  regime, this then leads to a signal intensity relationship of:

$$\frac{M(t)}{M_0} = 1 - \frac{2e^{\ln \left( \frac{1}{2} \left( 1 + e^{-\frac{TR_o}{T_{1pre}}} \right) \right) \frac{T_{1pre}}{T_1(t)}}}{1 + e^{-TR_o/T_1(t)}} \quad [A.11]$$

where  $T_{1pre}$  is the pre-contrast  $T_1$  of the tissue.



It may appear from Eq. [A.7] that it is possible to simultaneously null two different  $T_1$  values by adjustment of both TI and  $TR_o$ . However, no analytic expression for this double null condition has been found and numerical methods applied to specific values of  $T_1$  have been unable to yield a solution. This suggests that double nulling is not possible, except for the trivial case where  $TI_{eff}$  and  $TR_o$  are both zero.

## **Appendix 2**

### **Demographic Data**

NAME

ADDRESS

DOB

SEX

ETHNIC ORIGIN

HEIGHT

WEIGHT

### **Factors**

- |   |                              |                             |
|---|------------------------------|-----------------------------|
| 1 | Current smoker               | How many?                   |
| 2 | Ex-Smoker                    | How many?                   |
|   |                              | How long did you smoke for? |
|   |                              | How long since given up?    |
| 3 | Angina                       |                             |
| 4 | Past MI                      |                             |
| 5 | Known Hypertension           |                             |
| 6 | Known Hyperlipidaemia        |                             |
| 7 | Past CVA                     |                             |
| 8 | Peripheral vascular disease? |                             |
| 9 | Heart valve disease?         |                             |

## 10 Diabetes?

## How long?

Control	Diet / Insulin / Oral
---------	-----------------------

## Family History

## 11 Family history of

Heart disease?

## Angina

MI (at what age)

## Hypertension

## Hyperlipidaemia

## Current Medication

12 N/Y If Y Please list names of all medication:

## 13 Beta Blocker

14 Diuretics

15 Calcium antagonist

16 Aspirin

## 17 Nitrates

18     ACE inhibitor

19 Digoxin

## Appendix 3

### Publications.

#### Peer Reviewed Publications

A. Jivan, M. A. Horsfield, G. R. Cherryman, "MR enhancement of human myocardium *in vivo*, post Acute Myocardial Infarction using Multihance". Submitted: *Annual conference of The International Society for Magnetic Resonance in Medicine*, Sidney, Australia, (1998).

A. Jivan, M. A. Horsfield, G. R. Cherryman, "Practical considerations for dynamic myocardial *in vivo*  $R_1$  measurement using inversion recovery snapshotFLASH". Submitted: *Annual conference of The International Society for Magnetic Resonance in Medicine*, Sidney, Australia, (1998).

A. Jivan, M. A. Horsfield, A. R. Moody, G. R. Cherryman, "Dynamic  $T_1$  measurement using snapshot FLASH MRI". *Journal of Magnetic Resonance Series B*, 127:65-72 (1997).

A. Jivan, M. A. Horsfield, A. R. Moody, G. R. Cherryman, "Measurement of *in vivo*  $T_1$  using snapshot FLASH imaging". *Book of Abstracts: Proceedings of the International Society for Magnetic Resonance in Medicine*, Vancouver, Canada, p2060 (1997).

A. Jivan, M. A. Horsfield, A. R. Moody, G. R. Cherryman, "Dynamic  $T_1$  measurement using snapshot FLASH MRI". *Book of Abstracts: Proceedings of the International Society for Magnetic Resonance in Medicine*, New York, U.S.A. p1552 (1996).

A. Jivan, M. A. Horsfield, A. R. Moody, G. R. Cherryman, "Dynamic measurement of  $T_1$  *in vivo* using MRI". *Book of Abstracts, Radiology*, Birmingham U.K., *Supplement to volume 69 of the British Journal of Radiology*, 1535 (1996).

A. Jivan, M. A. Horsfield, A. R. Moody, J. Tranter, G. R. Cherryman, "Quantifying myocardial contrast uptake, post myocardial infarction, using a perfusion index." *Book of Abstracts: Rontgen Centenary Congress*, Birmingham U.K. p84 (1995).

A. Jivan, A. R. Moody, J. Tranter, G. R. Cherryman, "The feasibility of cardiac magnetic resonance imaging of acute myocardial infarction of the left ventricle; A technical report." *Book of Abstracts: The Society of Magnetic Resonance Technologists and The British Association of MR Radiographers*, London, U.K. (1994).

### **Contributions to Peer Reviewed Publications**

G. R. Cherryman, A. Jivan, A. R. Moody, N. Hudson, R Keal, A. McCullough, D.B. Barnett, K. L. Woods, J. Tranter, M. Early, G. P. Pirovano, A. Spinazzi. "Efficacy and safety of Multihance (Gd-BOPTA/dimeg) for MR imaging of acute myocardial infarction. *Book of Abstracts: Radiology 98*, Birmingham U.K. (1998).

J. H. Cullen, G. R. Cherryman, N. Hudson, J. Tranter, A. Jivan, M. A. Horsfield, K. L. Woods, D. B. Barnett. "The mechanism of precordial ST depression in inferior myocardial infarction. Evaluation by contrast enhanced dynamic myocardial perfusion magnetic resonance imaging and <sup>201</sup>thallium single photon emission computed tomography." *European Heart Journal*, submitted for publication (1997).

G. R. Cherryman, N. Hudson, A. Jivan, M. Early, J. Tranter, M. A. Horsfield, A. R. Moody, K. L. Woods, D.B. Barnett. "Myocardial perfusion imaging: A comparison of MRI and <sup>201</sup>Thallium in patients with acute myocardial infarction." *Book of Abstracts: Radiology 97*, Birmingham U.K. (1997).

G. R. Cherryman, A. R. Moody, A. Jivan, J. Tranter, N. Hudson, M. Early, K. L. Woods, D. B. Barnett, G. P. Pirovano, A. Spinazzi. "The safety and utility of myocardial perfusion imaging with gadobenate dimeglumine in patients with acute myocardial infarction." *Book of Abstracts: The Proceedings of the Third Asian Pacific Congress of Cardiovascular and Interventional Radiology*, Melbourne, Australia. (1997).

G. R. Cherryman, A. Jivan, A. R. Moody, N. Hudson, R. Keel, D. B. Barnett, K. L. Woods, J. Tranter, G. P. Pirovano, A. Spinazzi. "Dynamic perfusion MRI in patients with acute myocardial infarction (AMI): A comparison with <sup>201</sup>Thallium." *Book of Abstracts: Radiological Society of North America Radiology*, Chicago U.S.A. *Supplement to Radiology*, Supp 201 (P):165 (1996).

G. R. Cherryman, A. Jivan, A. R. Moody, N. Hudson, R. Keel, A. McCullough, D.B. Barnett, K. L. Woods, J. Tranter, M. Early, G. P. Pirovano, A. Spinazzi. "Utility of myocardial perfusion imaging with gadobenate dimeglumine post acute myocardial infarction." *Book of Abstracts: 19th International Congress of Radiology*, Peking, China (1996).

J. H. Cullen, J. Tranter, A. R. Moody, K. L. Woods, N. Hudson, A. Jivan, R. Keel, D. B. Barnett, G. R. Cherryman. "Detection of posterior extension in inferior myocardial infarction using magnetic resonance imaging: comparison with <sup>201</sup>thallium perfusion imaging." *European Heart Journal*, p 24 vol 17 (1996).

J. H. Cullen, J. Tranter, A. R. Moody, N. Hudson, R. Keel, A. Jivan, K. L. Woods, D. B. Barnett, G. R. Cherryman. "Localisation of posterior myocardial infarction using MRI: A comparison of electrocardiogram with <sup>201</sup>thallium perfusion imaging." *Book of Abstracts, Radiology UK, Supplement to volume 69 of the British Journal of Radiology*, (1996).

G. R. Cherryman, A. R. Moody, N. Hudson, J. Tranter, M. A. Horsfield, S. Bolton, A. Jivan, K. L. Woods, D.B. Barnett. "Acute myocardial infarction demonstrated by dynamic MRI: A comparison with <sup>201</sup>Thallium and ECG." *Book of Abstracts: Rontgen Centenary Congress*, Birmingham U.K., p83 (1995).

G. R. Cherryman, A. R. Moody, A. Jivan, N J. Tranter, S. Bolton, M. A. Horsfield, Hudson, M. Early, N. Hudson. "Dynamic myocardial MRI following acute myocardial infarction." *Book of Abstracts: Proceedings of the annual scientific meeting, Royal College of Radiologists*, Norwich U.K. (1994).